New Low Temperature Techniques for Electron Thermometry and Thermal Isolation

Joshua Michael Allen Chawner, MPhys (Hons)

Supervisor: Dr. Jonathan Prance
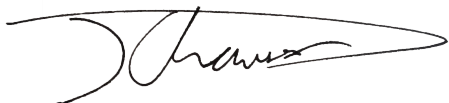Prof. Yuri Pashkin

A thesis submitted for the degree of
Doctor of Philosophy

Lancaster University
Department of Physics
September 2020

Declaration

I declare that this thesis titled, 'New Low Temperature Techniques for Electron Thermometry and Thermal Isolation' and the work presented in it are entirely my own. I confirm that:

- This thesis has not been submitted in substantially the same form for the award of a higher degree elsewhere.

- Where I have consulted the published work of others, this is always clearly attributed and the source is always given. With the exception of such quotations, this thesis is entirely my own work.

- The word count of this thesis is 31,489 and does not exceed the permitted maximum of 80,000.

Joshua M. A. Chawner

September 2020

'An acquaintance with natural laws means no less than an acquaintance with the mind of God' [1]

James Prescott Joule

Joshua Michael Allen Chawner, MPhys (Hons)

New Low Temperature Techniques for Electron Thermometry and Thermal Isolation

Doctor of Philosophy
September 2020

Abstract

Measuring electron temperature is an important method to understand the stability and coherence of a quantum circuit, since this variable describes how 'quiet' the electronic environment is. In this thesis, the construction, calibration and operation of a quantum dot electron thermometer is demonstrated in two different cryostats. Compared to previous implementations of a quantum dot thermometer, the work presented here is unique in that it only requires a single gate connection to calibrate and operate, which simplifies the application of the device substantially. For the thermometer calibration, a physical model of the quantum-dot reservoir system was developed, which reveals information usually obtained from a stability diagram. Electron thermometry was successfully performed with the calibrated thermometer in a $1.0\,\mathrm{K}$ to $3.0\,\mathrm{K}$ range. With the fastest mode of operation the quantum dot thermometer was shown to have a sensitivity of $3.7 \pm 0.3\,\mathrm{mK}/\sqrt{\mathrm{Hz}}$ at $1.3\,\mathrm{K}$. This device provides a new versatile, sensitive and effective tool for monitoring electron temperature in nanoelectronic devices at cryogenic temperatures. Also in this thesis, several plastic solid-void structures were demonstrated to offer excellent thermal and structural properties at sub-Kelvin temperatures. Good low temperature insulators are extremely useful for support cryogenic components and sample environments without leaking unwanted heat. A structure fabricated from commercially available ABS LEGO elements was shown to be effective at thermally insulating two bodies at sub-Kelvin temperatures, with a thermal conductivity of $\kappa = (8.7 \pm 0.3) \times 10^{-5} T^{1.75 \pm 0.02}\,\mathrm{Wm^{-1}K^{-1}}$. Similar scale 3D printed ABS and PLA gyroid structures were shown to also be effective as low-temperature insulators, having a thermal conductivity of $\kappa = (3.07 \pm 0.05) \times 10^{-5} T^{1.72 \pm 0.02}\,\mathrm{Wm^{-1}K^{-1}}$ and $\kappa = (4.45 \pm 0.05) \times 10^{-5} T^{1.64 \pm 0.02}\,\mathrm{Wm^{-1}K^{-1}}$, respectively. These samples demonstrate how low temperature insulation can be improved with readily available, fully customisable and affordable components.

Acknowledgements

Throughout my work, I have been blessed with the acquaintance and support of so many extraordinary people within and around Lancaster. First of all I must thank my supervisor Jon Prance. His contributions to my theoretical and experimental endeavours have been fully involved and continuous. His ability to apply calm perspective to any situation has been essential to my progress, and it is simply a fact that this thesis would not exist without Jon's guidance. I must also thank my deputy supervisor, Yuri Pashkin, whose unparalleled understanding of the theory has helped me steer clear from logical pitfalls, and experience in the lab has aided my experiments greatly.

Working in the lab brings out every conceivable emotion, both good and bad, but the people I worked alongside have made this experience much more pleasant. I thank Dmitry 'Dima' Zmeev, whose contagious enthusiasm for low temperature physics perfectly captures all that is great about being a scientist. Special thanks goes to Alex Jones, who seemingly knows more about the cryostats than the people who built them, and has been a great friend since he first showed me to my desk. Many thanks must go to Andy Guthrie, my laboratory accomplice; together we have consoled each other over many dead samples and witnessed each others many successes. I also thank Michael Thompson for continual assistance with experimental techniques from my first day to my last.

Living and working in Lancaster has been great fun, thanks to the ever-changing company of my fellow office dwellers, coffee-club attendees, cinema enthusiasts, fell climbers and pub regulars, too many to list. I would however particularly like to thank Ash Jennings for his mini-lectures in philosophy, Xiao Collins for his table tennis master class, Leo Forcieri for teaching me the ways of living *la dolce vita*, Sophie Au-Yong for daily games of backgammon, James & Charlotte Fong for many enjoyable outings, and Hsin Hui Chang for numerous much-needed escapes around the world. I also wish to show my gratitude to all the folks at the Lancaster University Sailing Club for many happy memories, and in particular for allowing me to forget I am a 'old buoy' for two glorious nights a year at the extraordinary Southport 24 hour race.

Finally, I would like to thank my parents and my brothers for their unconditional love and support.

Contributions

This thesis details the work that is the result of joint research, and is the basis for three articles drafted by myself, that I have authored alongside my collaborators at Lancaster and externally. The experiments carried out in this thesis can be divided into two major sections; electron thermometry and thermal isolation.

For the electron thermometry experiments, the transistor devices used as an electron thermometer were fabricated by Dr. S. Barraud at CEA-Leti. The experiments were designed, performed and analysed by myself, with the help and guidance of Dr. J. Prance, Professor Yu. A. Pashkin, Dr. E. A. Laird and Dr. M. Fernando Gonzalez-Zalba. Data collection for these experiments was carried out using collection software developed by myself. My PCB designs were manufactured by S. Holt and his team at the Lancaster Physics Electronic Workshop, who also provided assistance with measurement electronics. I also acknowledge the suggestions from X. Collins, Dr. K. L. Ramrakhiyani, Dr. M. Thompson and Dr A. Jones towards this work.

For the thermal isolation experiments, the samples were fabricated by myself, Dr. D. Zmeev and Prof. R. Young. I played a central role in designing and performing the experiments. The data collection was undertaken by Dr. D. Zmeev, with the assistance of Dr. V. Tsepelin, Dr. A. Jones and Dr. T. Noble. The analysis was performed by myself, with the help and guidance of the ULT group, including Dr. D. Zmeev, Professor. G. Pickett, Dr. V. Tsepelin and Dr. S. Autti. I also acknowledge the suggestions from Professor T. Guénault, Professor R. Haley and Dr J. Prance towards this work.

Contents

List of Figures

List of Tables

Nomenclature

QD	**Q**uantum **D**ot
AC	**A**lternating **C**urrent
RF	**R**adio **F**requency
PCB	**P**rinted **C**ircuit **B**oard
SMA	**S**ub**M**iniature version **A**
FET	**F**ield **E**ffect **T**ransistor
BNC	**B**ayonet **N**eill-**C**oncelman
LO	**L**ocal **O**scillator
IO	Oxford Instruments '**IO**' cryostat (Details in section 2.3)
LD250	BlueFors '**LD250**' cryostat (Details in section 2.3)
FWHM	**F**ull **W**idth **H**alf **M**aximum
SEM	**S**canning **E**lectron **M**icroscope
PID	**P**roportional–**I**ntegral–**D**erivative
ABS	**A**crylonitrile **B**utadiene **St**yrene
PLA	**P**oly**LA**ctide
AL	**A**BS **L**EGO sample (Details in section 5.1)
AWG	**A**BS **W**alled **G**yroid sample (Details in section 5.1)
AOG	**A**BS **O**pen **G**yroid sample (Details in section 5.1)
PWG	**P**LA **W**alled **G**yroid sample (Details in section 5.1)
RMS	**R**oot **M**ean **S**quare

To my Grandma Win Evans
and in memory of my Grandad,
and my pal,
Bill Evans.

Chapter 1

Introduction

1.1 Motivation

Today, physicists have the exciting task of experimentally realising quantum phenomena in ways that were impossible to achieve during the development of the theory 100 years ago. The technology now exists to construct $\sim$ nm scale devices and control them, therefore providing the freedom to design and construct scalable quantum circuitry. A notable example is the quantum computer, which uses the superposition of quantum states in an array of 'qubits' to produce advanced logic beyond the reach of classical computation [2, 3, 4]. Most quantum electronic systems in their current form are highly sensitive to many forms of energy. Mechanical, electromagnetic and thermal noise all can limit the performance and capabilities of both classical and quantum circuits. All of these forms of noise are minimised inside the shielded low temperature environment of a cryostat.

For charge-based quantum circuits, unwanted heat is important to minimise so as to reduce the electron temperature, which creates more coherent charge qubits and increased stability in the application of logic gates, allowing a more complex and scalable circuit [5, 6, 7]. With increased circuit complexity, the multiple signal lines required to connect to room temperature electronics can quickly reach the maximum available quantity within the cryostat. Measuring electron temperature is a good method to understand the stability and coherence of a quantum circuit, since this variable is fundamental to how the circuit will behave. Several approaches exist to perform low temperature electron thermometry, which use the Fermi-Dirac statistical energy

distribution of an electron gas [8, 9] to read out the temperature [10, 11, 12, 13], for example via tunnel junction transport [14, 15, 16]. Conduction around the Coulomb blockade within electronic islands [17, 18, 19, 20] or quantum dots [21, 22, 23] are both good thermometry techniques which require direct galvanic connections to the electron reservoir. Charge sensing quantum dots allow non-invasive electron temperature readout, with galvanic connections external to the electron reservoir [24, 25, 26]. Radio-frequency probing is another technique for non-invasive readout from thermometer devices via capacitive connections coupled to a resonator [27, 28]. These techniques still require multiple connections to the thermometer device.

This thesis describes a new take on a non-invasive quantum dot electron thermometer that only requires a single connection to the device for calibration and operation. The characteristics of the quantum dot are measured during the calibration procedure without any source or drain connections, which simplifies the installation and operation of the thermometer substantially. The thermometer can be used to measure the electron temperature of any conducting system without any galvanic interference. This makes it an exceptionally versatile electron thermometer that can be easily added into low temperature circuits, or retro-fitted to existing systems.

Achieving the lowest possible temperature environment is the first step in reducing electron temperature. Therefore a cryogenic system requires good thermal isolation between components to reduce any unwanted heat entering the experiment. For example some commercial cryogen-free fridges use stainless steel heat switches to thermally isolate the separate stages. Wet fridges often use Macor or Vespel pillars to support the mixing plate due to the excellent insulation provided by plastics and ceramics [29, 30]. Using insulators with lower heat conductance within these systems can reduce the thermal energy and noise within an experiment. Good insulation is useful for all cryogenics, but in particular the current progression of quantum computing, which relies on isolated low temperatures for operation and coherence.

This thesis describes the testing of several designs for solid-void insulators that are effective in low temperature environments. This includes the affordable and scalable LEGO element system, a commercial option that gives very effective insulation and strong support. Several plastic structures were

created using the cheap and infinitely customisable process of 3D printing. These structures also demonstrate excellent insulation properties.

1.2 Chapter Outline

In detail, this thesis is organised as follows:

- Chapter 2 describes the necessary theoretical background for this thesis. This includes quantum dot theory focusing on the Coulomb blockaded regime, details of using radio-frequency electronics and cryogenic apparatus to probe a quantum dot, and details of fit modelling. The Debye model of a solid is also discussed in the context of measuring thermal conductivity.

- Chapter 3 describes the experimental techniques used to build and optimise a quantum dot electron thermometer. This includes the design and optimisation of the low temperature and room temperature radio-frequency electronics, plus details on the choice of Si field-effect transistor used to create the quantum dot tunnel coupled to an electron reservoir.

- Chapter 4 describes the successful single-line calibration and operation of a quantum dot thermometer, in two different cryostats. This includes analysing the validity of the thermometer calibration and analysing the error in the electron thermometry.

- Chapter 5 describes the fabrication and thermal conductivity measurements of new solid-void plastic insulators for use at low temperatures.

- Chapter 6 gives a summary of the outcomes and conclusions from this thesis, and potential for future work.

1.3 Current and Future Publications

This thesis details the work that went into the following articles, all of which have been drafted by the author:

I LEGO® Block Structures as a Sub-Kelvin Thermal Insulator (Published in Scientific Reports 2019 [31])

II Non-galvanic calibration and operation of a quantum dot thermometer (Accepted for publication in Physical Review Applied 2021.)

III 3D-Printed Plastic Structures as a Sub-Kelvin Thermal Insulators (To be submitted.)

Chapter 2

Background

In October 1745, German cleric Ewald Georg von Kleist went to his lab and began working on his latest experiment. He connected a wire between a high-voltage electrostatic generator and a large volume of water in a glass jar, in an attempt to 'store electricity' in the conducting water. Von Kleist found that touching the wire resulted in a powerful spark, much more painful than that obtained from the electrostatic generator alone. His hand and the water acted as conductors, and the jar as a dielectric; the capacitor had been discovered. By touching the wire, the capacitor was shorted, and all the stored charge in the large volume of water was discharged instantly through Von Kleist. The capacitance between two conductors is a conceptual pillar of all that came after this discovery; the storage of electrical power, the transistor, electrical information, and now quantum electronics.

—●•●—

This chapter details the relevant background, theory and techniques that are applied in the electron thermometer experiments detailed in Chapters 3 and 4, and the thermal isolation experiments detailed in Chapter 5. This includes a description of a quantum dot coupled to a electronic reservoir in Section 2.1 and a technique for modelling data to estimate parameters in Section 2.2. The various cryostat equipment used is described in Section 2.3 and the radio-frequency electronics used to interact with the quantum electronics is described in Section 2.4. The thermal conductivity of an insulator using the Debye model is derived in Section 2.5.

2.1   Quantum Dots

An electronic potential island that can confine charge carriers in all three spatial dimensions will have a quantised density of states, for example an atom and its discrete set of electron energy levels. This occurs when the spatial confinement is similar to the de Broglie wavelength of the charge carrier, which in semiconductors is $\sim 100\,\text{nm}$. A quantum dot (QD) is the artificial creation of such a system in a metal or semiconductor device [32, 33].

QDs have enjoyed a thorough and varied experimental development in the last 30 years. The QD's simplicity and scalability makes it a fundamental entity in the world of nano-electronics, and one of the most popular gateways into the quantum world.

This work focuses on semiconductor QDs investigated in the Coulomb blockade regime, where the QD is weakly coupled to the electrodes. The properties of this system are detailed in this section for later reference in the experimental Chapters 3 and 4, where a QD is integrated into a low temperature circuit and used as an electron thermometer.

In Section 2.1.1, the basis for the electrostatic behaviour of a QD is explained with the capacitance model. Section 2.1.2 details the relevant energy scales in a QD system and the requirements for achieving Coulomb blockade. This is explained further in Section 2.1.3, where the QD stability diagram is detailed. Section 2.1.4 describes how a QD can be used as an electron thermometer. Some more specific details about a tunnel coupled QD with no source-drain bias voltage are included in Section 2.1.5. Finally a brief mention of the electron-phonon coupling is included in Section 2.1.6.

2.1.1   Capacitance Model

The behaviour of a QD is built upon the capacitance network that surrounds it, which is described with a capacitance matrix. Each conducting object i has a self-capacitance described by the matrix element C_{ii}, which represents the amount of electric charge that must be added when completely isolated to raise the object's potential by one volt. Each object also has a set of mutual capacitance matrix elements C_{ij}, which represents the capacitance with

any other conducting object j. If we imagine a series of individual metallic objects, we can define the charge on object i as

$$Q_i = \sum_{j=0}^{n} C_{ij} V_j + Q_i^{(0)},\tag{2.1}$$

where V_j is the potential of object j and $Q_i^{(0)}$ is the charge that resides on object i when all voltages are zero [34]. n represents the number of conducting objects in the system. For a closed system, the sum of non-residual charge the capacitance matrix along each row or column is zero, i.e $\sum_{j=0}^{n} C_{ij} = \sum_{i=0}^{n} C_{ij} = 0$. Consider the object $i = 0$ as our QD, the sum across j represents the addition of the QD self-capacitance C_{00} and the total capacitance between the QD and all other objects $C_\Sigma = -\sum_{j=1}^{n} C_{0j}$ (the values for the mutual capacitance matrix elements are negative, so C_Σ is positive). $|C_{0j}|$ is the capacitance of object j, such as a gate electrode, with respect to the QD. Therefore we can say for our closed system $C_{00} - C_\Sigma = 0$, which combined with Equation 2.1 makes the potential V_0 on the QD equal to:

$$V_0 = \frac{Q_0 - Q_0^{(0)}}{C_\Sigma} - \sum_{j=1}^{n} \frac{C_{0j} V_j}{C_\Sigma},\tag{2.2}$$

For any object, the stored charge Q_i must be an integer of the elementary charge, which has been recently defined to be exactly $e = 1.602176634 \times 10^{-19}$ C. Note that e is a positive value, which will be the notation throughout this thesis. Therefore, for the QD, we can define the electrostatic energy E_e required to add N additional electrons to the object as

$$E_e(N) = \int_{Q_0^{(0)}-eN}^{Q_0^{(0)}} V_0(Q_0)\mathrm{d}Q_0 = \frac{e^2 N^2}{2C_\Sigma} + eN\left(\frac{Q_0^{(0)}}{C_\Sigma} + \sum_{j=1}^{n} \frac{C_{0j}}{C_\Sigma} V_j\right).\tag{2.3}$$

2.1.2 Quantum Dot Energies and the Coulomb Blockade

A QD has several energy scales associated with it, and the magnitude of these energies define its electronic characteristics.

First we consider the quantum confinement energy. Any quantum-mechanical

system is described with a Hamiltonian operator $\hat{H}$, which possesses a quantum state described by the wave function Ψ. The total energy of the system E is defined by the allowed eigenvalues from Schrödinger's wave Equation $\hat{H}\Psi = E\Psi$ [35, 36]. Consider a classical N-electron system within a bulk semiconductor. The electron distribution can be described as [34]:

$$\rho_e(\mathbf{r}) = -e \sum_n \delta(\mathbf{r} - \mathbf{r}_n), \tag{2.4}$$

where e is the elementary charge, δ is the delta function, $\mathbf{r}$ is a position vector and $\mathbf{r}_n$ is the coordinate vector of the nth electron. The Hamiltonian for this N-electron system is:

$$\hat{H}_N = \sum_{n=1}^{N} \left\{ \frac{[\mathbf{p}_n + e\mathbf{A}(\mathbf{r}_n)]^2}{2m^*} - eV(\mathbf{r}_n) + \frac{1}{2}g^*\mu_B\boldsymbol{\sigma}\mathbf{B}(\mathbf{r}_n) + e^2 \sum_{n-1}^{m=1} G(\mathbf{r}_m, \mathbf{r}_n) \right\}. \tag{2.5}$$

The first term describes the Hamiltonian of a free electron in an external magnetic field $\mathbf{B} = \nabla \times \mathbf{A}$, with p_n representing the momentum of electron n with effective mass m^*. The second term is the electric potential field V. The third term is the Zeeman term which describes the influence of the magnetic field on the electron's energy, with the Landé g-Factor g^* and the Bohr magneton μ_B. The components of $\boldsymbol{\sigma}$ are the Pauli matrices. The final term is the electron-electron interaction term, which describes the influence of all other electrons onto each individual electron, where G is the Coulomb interaction between two electrons at positions $\mathbf{r}_m$ and $\mathbf{r}_n$. For the systems discussed within this thesis, the magnetic field is at zero. With a sufficiently strong confinement potential, the energy eigenvalues of the Schrödinger wave equation will be a set of quantised energy levels that trapped electrons will occupy. For example, a QD realised within a 2D electron gas with radius r and N electrons, in a material with a parabolic dispersion relation, will have a total confinement energy equal to:

$$E_{\text{tot}} = \frac{\hbar^2}{m^*r^2}N^2, \tag{2.6}$$

where m^* is the electron effective mass and $\hbar$ is the reduced Planck's constant [34]. Therefore the confinement energy required to add another electron is

given by:

$$E_{\text{add}} = E_{\text{tot}}(N+1) - E_{\text{tot}}(N) = \frac{\hbar^2}{m^* r^2} N, \tag{2.7}$$

for a large N. We then find that the spacing between corresponding confinement energy levels is:

$$E_{\text{con}} = E_{\text{add}}(N+1) - E_{\text{add}}(N) = \frac{\hbar^2}{m^* r^2}. \tag{2.8}$$

This defines what is known as the single-particle level spacing.

Next we consider the influence of the Coulomb energy, which when dominating can produce interesting electronic characteristics. A conducting island must charge and de-charge in quantised steps of elementary charge e. If we consider the island (denoted object $i = 0$) to contain N electrons, the electrostatic energy is described with Equation 2.3. Therefore the electrochemical potential of the QD (or the energy required to add one more electron) is:

$$\mu_N = E_{\text{e}}(N+1) - E_{\text{e}}(N) = \frac{e^2 N}{C_\Sigma} + \frac{e^2}{2C_\Sigma} + e\left(\frac{Q_0^{(0)}}{C_\Sigma} + \sum_{j=1}^{n} \frac{C_{0j}}{C_\Sigma} V_j\right). \tag{2.9}$$

A common term used to characterise a quantum dot is the charging energy E_c, which is given as the difference in μ_N for subsequent electron adding:

$$E_c = \mu_{N+1} - \mu_N = \frac{e^2}{C_\Sigma}. \tag{2.10}$$

Therefore in the constant interaction model, the charging energy is assumed to be a constant. This is safe to assume for a small range of N, where C_Σ will remain constant. Let us assume a dot radius of 100 nm in a GaAs 2DEG. The self capacitance of such a QD would be $C_{00} = 8\epsilon\epsilon_0 r$ (ϵ_0 is the vacuum permittivity and $\epsilon = 12.53$ is the relative permittivity for GaAs). Assuming the self capacitance dominates over the mutual capacitance from any surrounding objects, this system would be characterised by a charging energy $E_c = 1.8$ meV and a single-particle level spacing of $E_{\text{con}} = 0.11$ meV. In this case, the Coloumb energy dominates over the confinement energy. This creates a QD energy spectra with many confined states which all jump significantly on the energy scale with the addition or subtraction of an electron,
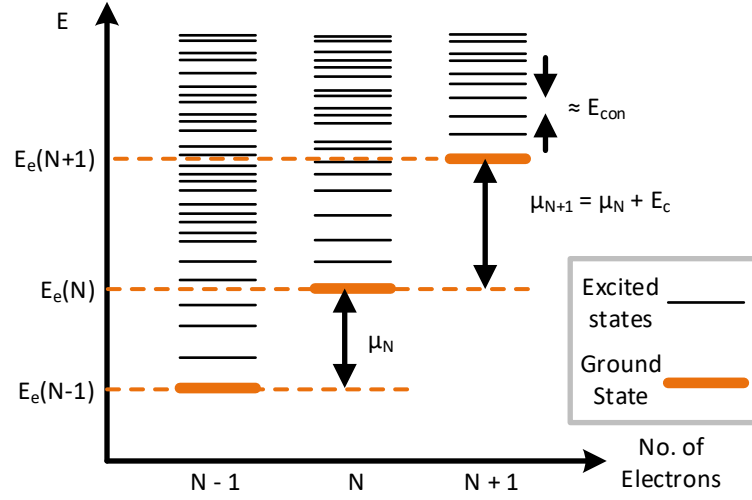
Figure 2.1: Typical energy spectra of a QD for adjacent electron numbers. $E_e(N)$ represents the electrostatic energy required to add all N electrons to the QD. μ_N shows the energy required to add just the Nth electron to the QD. The difference between μ_N and μ_{N+1} is the charging constant E_c, which is true for any value of N, assuming the QD has constant geometry. E_{con} represents the single-particle level spacing defined by 0D quantum confinement.

visualised in Figure 2.1. An effective 'ladder' of energy levels exists within the QD, where each 'rung' of the ladder is separated by E_c and can be individually filled with a single electron.

Another energy to consider is the brodening of the QD energy levels originating from the tunnel coupling to nearby conductors. The magnitude of this energy can be derived from an adaptation of Heisenberg's uncertainty principle [37, 38], which states:

$$\alpha_E \alpha_t \geq \frac{\hbar}{2}, \tag{2.11}$$

where $\hbar$ is the reduced Planck constant, α_E is the uncertainty in the energy of an electron occupying a QD energy level and α_t is the uncertainty in time to charge or discharge the QD from the conductor. Each of the QD tunnel barriers has a tunnel resistance given by:

$$R_T = V_R / I_R, \tag{2.12}$$

where V_R is the potential over the barrier and I_R is the current tunnelling through the barrier. If R_T is low, electrons can tunnel in and out of the QD quickly, decreasing α_t which in turn allows α_E to increase. For Coulomb blockade to be preserved, the uncertainty in electron energy must be much less than the charging energy $\alpha_E \ll E_c$. Therefore, combined with the uncertainty condition in Equation 2.11, the time uncertainty must follow:

$$\alpha_t \gg \frac{\hbar C_T}{2e^2},\tag{2.13}$$

where C_T is the mutual capacitance across the tunnel coupled QD and nearby conductor. The charging time for the QD is $\sim R_T C_T$, therefore the uncertainty in energy can broaden the QD density of states, unless the tunnelling resistance R_T exceeds the resistance quantum:

$$R_T \gg \frac{\hbar}{2e^2}.\tag{2.14}$$

If the condition in Equation 2.14 is met, the uncertainty in the QD energy levels is diminished and a well defined number of electrons can exist within the QD. The tunnel rate through the barrier Γ_T is given by $\Gamma_T = V_R/eR_T$. If all tunnel barriers are considered with a total tunnel rate Γ, then the minimum value α_E can take is limited by the tunnel coupling energy $\hbar\Gamma$.

The electrons in the conductors outside the QD also have thermal fluctuations in energy of the order $\sim k_B T_e$, where T_e is the electron temperature and k_B is the Boltzmann constant. For the Coulomb blockade to occur, the charging energy must dominate over the other energy scales [32]:

$$E_c \gg k_B T_e, \ \hbar\Gamma, \ E_{con}.\tag{2.15}$$

It is possible to observe the single-particle level spacing (referred to as the QD excited states) if the temperature and tunnel rate are both low enough to meet the following condition:

$$E_{con} > k_B T_e, \ \hbar\Gamma.\tag{2.16}$$
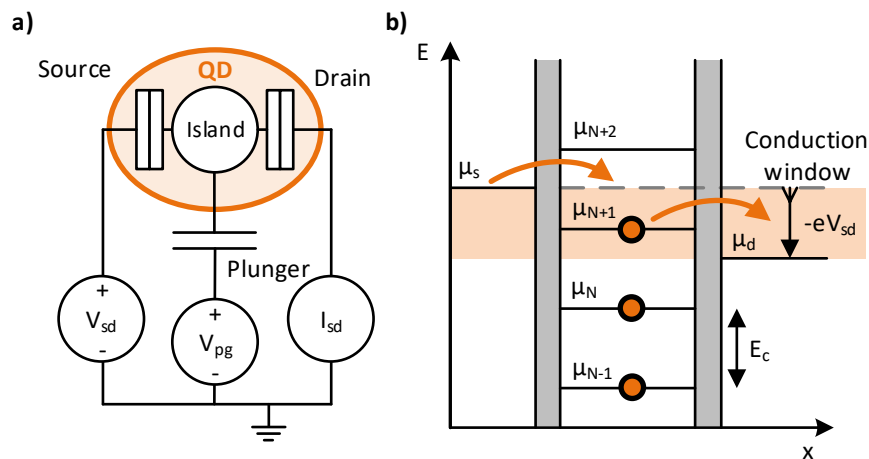
Figure 2.2: a): Simplified circuit schematic of a QD with source and drain connections via tunnel barriers and a capacitative plunger gate connection. V_{sd} controls the source-drain voltage over the QD and V_{pg} controls the pluger gate voltage, which shifts the energy levels in the QD via capacitive coupling. **b)**: An energy diagram of a QD whilst tuned to a Coulomb peak with a small negative V_{sd} applied. μ_s and μ_d are the source and drain electrochemical potentials respectively, and μ_N is the chemical potential of the QD when it is occupied by N electrons. The Nth electron can tunnel in from the source as it has the required energy to do so, and it can tunnel out into the drain. If V_{pg} is adjusted so that there is no energy state within the bias voltage window, then the Nth electron does not have enough energy to tunnel into the QD, and the $N-1^{th}$ electron does not have enough energy to tunnel out. This would mean the QD is Coulomb blockaded.

2.1.3 Stability Diagram

To better understand the transport characteristics through a QD, consider
the schematic of a generic QD circuit (Figure 2.2). A plunger gate electrode
is capacitively coupled to the QD, and source-drain connections are coupled
via tunnel barriers. In this system, there are three entities coupled to the QD,
the source connection (s), the drain connection (d) and the plunger gate (pg).
A useful term is the lever arm α_i, which is defined as

$$\alpha_i = \frac{C_i}{C_\Sigma}, \tag{2.17}$$

which normalises the capacitive influence of object i on the QD. Therefore,
combining Equations 2.9 and 2.17, the electro-chemical potential of the QD
can be described by

$$\mu_N(V_{pg}) = \frac{e^2 N}{C_\Sigma} + e(\alpha_s V_s + \alpha_d V_d + \alpha_{pg} V_{pg}). \tag{2.18}$$

The electro-chemical potential of the metallic source (drain) connection is de-
fined as $\mu_s = -eV_s$ ($\mu_d = -eV_d$), and the source-drain voltage is $V_{sd} = V_s - V_d$. If we assume a small positive source-drain bias V_{sd}, the QD con-
ductance is non-zero when $\mu_s \geq \mu_N \geq \mu_d$, as this allows electron tun-
nelling through both tunnel barriers. The QD is Coulomb blockaded if μ_N
is outside this region and the electron tunnelling is blocked at either tun-
nel barrier (shown in Figure 2.2). If $V_{sd} = 0$ and V_{pg} is varied to make
$\mu_N(V_{pg}^{(0)} + \Delta V_{pg}) = \mu_{N+1}(V_{pg}^{(0)})$, it can be shown with Equation 2.18 that the
change in V_{pg} must be

$$\Delta V_{pg} = \frac{e}{C_\Sigma \alpha_{pg}}. \tag{2.19}$$

This tells us the separation in plunger gate voltage of neighbouring QD Coulomb
peaks if there is a small bias applied (also known as conductance resonances,
however in this thesis they will be referred to as 'Coulomb peaks' to avoid
confusion with the electrical response of a resonant circuit).

Now consider varying V_{sd} whilst keeping V_{pg} constant. Each QD energy
level within the voltage window allows a electrons to tunnel through the
QD one-by-one. This creates a step-like conductance where each step occurs

when an additional energy level can contribute to the source-drain current. These steps can only be observed if both the thermal broadening is small and the total tunnel rate through the QD is small enough to avoid tunnel broadening (described by Equations 2.15 and 2.14). The minimum source-drain bias voltage to guarantee conduction through the QD at all V_{pg}, labelled ΔV_{sd}, is equivalent to the charging energy i.e $\Delta V_{sd} = E_c/e$.

The QD stability diagram is created by measuring I_{sd} whilst sweeping V_{pg} against V_{sd}, and it gives one of the most recognisable signatures of a QD: the Coulomb diamond (Figure 2.3). This diamond pattern allows us to extract many characteristics of the QD, for example the plunger gate lever arm $\alpha_{pg} = \Delta V_{sd}/\Delta V_{pg}$. Both ΔV_{pg} and ΔV_{sd} are trivial to interpret from the stability diagram. The plunger gate lever arm can be more accurately determined for a single Coulomb peak using the relationship

$$\alpha_{pg} = \frac{1}{m_d - m_s}, \tag{2.20}$$

where $m_d = \mathrm{d}V_{pg}^{(d)}/\mathrm{d}V_{sd}^{(d)}$ is the gradient along the 'drain resonance' side of a Coulomb diamond and $m_s = \mathrm{d}V_{pg}^{(s)}/\mathrm{d}V_{sd}^{(s)}$ is the gradient along the 'source resonance' side.

2.1.4   Quantum Dot Thermometry

The technique of probing the statistical energy distribution of an electron gas to read out the electron temperature exists in several popular forms [10, 11, 12, 13]. One example is measuring tunnel junction conduction, or shot noise, to perform electron thermometry [14, 16, 15]. Coulomb blockade thermometry is a popular choice for measuring electron temperature, and readout can be achieved with source-drain conduction measurements of metallic islands, which can be coupled to magnetic cooling mechanisms [17, 12, 18, 19, 20]. A similar technique can be achieved using solitary QDs, which can be easily coupled to other quantum electronic systems [11, 21, 22, 23]. Localised charge sensing of QDs is a less invasive approach that does not require conduction measurements through the electron reservoir(s) [24, 25, 26, 22].
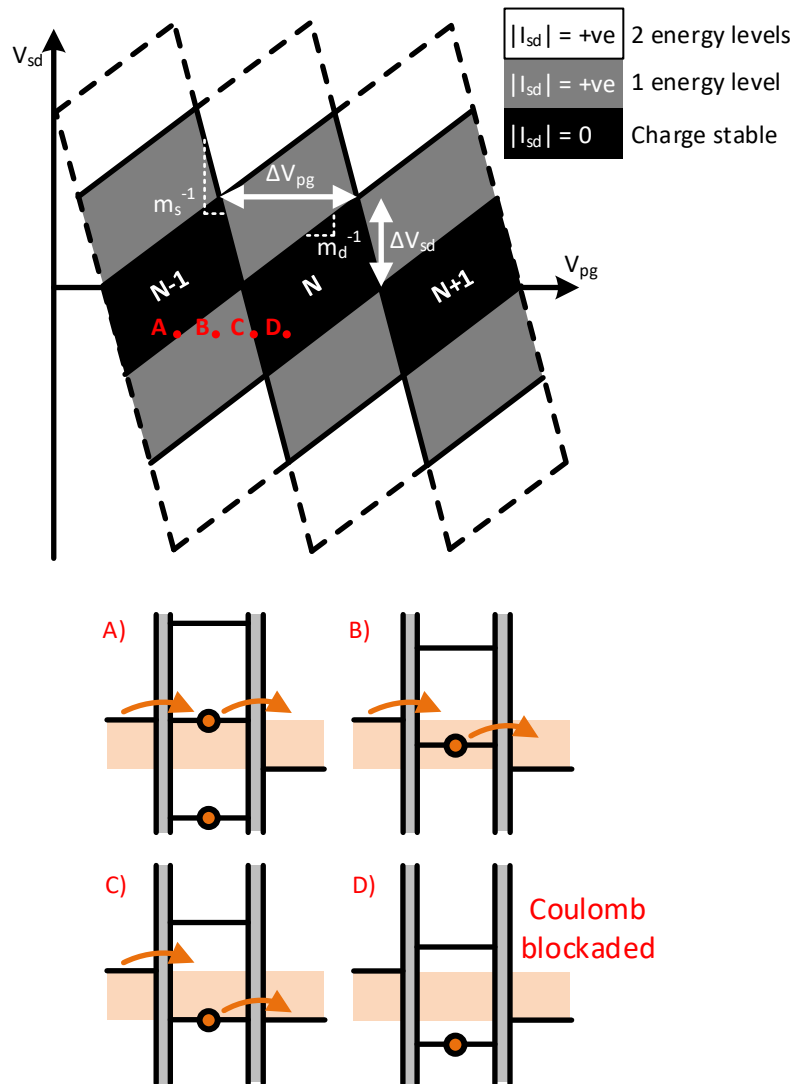
Figure 2.3: Top: QD charge stability diagram showing Coulomb diamonds formed (in black) from Coulomb peaks at various source-drain bias V_{sd}, assuming QD temperature $T = 0$. The black diamonds are Coulomb blockaded, so the QD is charge stable and has no conduction. Each subsequent Coulomb diamond with increasing plunger gate voltage V_{pg} contains an extra electron within the charge stable QD (labelled with N, $N + 1$, etc.). The grey and white diamonds demonstrate areas where there are single and double QD energy levels in the bias voltage window, respectively. Each energy level within the bias window adds a source-drain transport channel for electrons, which steps up the QD source-drain conductance. The stepped conductance pattern will continue with larger $|V_{sd}|$ adding more transport channels. ΔV_{pg} shows the spacing between Coulomb peaks, with each additional peak adding an electron to the QD. This is equivalent to the width of the diamonds. ΔV_{sd} is the height of the diamonds from the $V_{sd} = 0$ axis. **Bottom**: Electron energy diagrams of points A to D from the stability diagram, all shown when $V_{sd} = -\Delta V_{sd}/2$. A to C show the various stages of a Coulomb peak through the QD. D shows the Coulomb blockaded QD. Conduction is only allowed when at least one electron energy level is inside the voltage window.

For QD thermometry, the technique is ultimately modelled around the tunnelling behaviour of electrons in and out of the QD. This is because the electron occupation of a well defined energy in the QD reveals information about the statistical distribution in the coupled reservoir, as will be explained here. Consider an electron transmission from state i to state j. The electron tunnel rate $\gamma_{i \to j}$ (transmission probability per unit time) is defined by Fermi's golden rule [39, 40, 41, 34, 42]:

$$\gamma_{i \to j} = \frac{2\pi}{\hbar} |M_{ij}|^2 \rho(E_{\mathrm{j}}) \tag{2.21}$$

where M_{ij} is a matrix element that defines the coupling between states i and j, ρ is the density of states (that is receiving the electron) and E_{j} is the energy of state j. The QD is tunnel coupled to two reservoirs, the source and the drain. The total tunnelling rate from the source lead (s) into the QD (q) is given from the integral of Equation 2.21:

$$\Gamma_s = \frac{2\pi}{\hbar} \int_{-\infty}^{\infty} |M_{sq}|^2 n(E) F(E - \mu_s) \mathrm{d}E, \tag{2.22}$$

where $n(E)$ is the QD density of states and $F_{\mathrm{s}}(E)$ is the probability of finding in electron in the reservoir at energy E, which is given by the thermally broadened Fermi-Dirac distribution [8, 9]:

$$F(E) = \frac{1}{\exp\left(\frac{E}{k_{\mathrm{B}} T}\right) + 1}. \tag{2.23}$$

For a simple QD system we consider the tunnel rates Γ_{s} and Γ_{d} for the source and drain barriers respectively. Lets say the QD has $N - 1$ electrons and the resultant available ground state energy is μ_N. If the tunnelling resistance of the QD (Equation 2.12) is low, then the each energy in the QD density of states ladder μ_N is tunnel broadened. The shape of the broadening can be approximated as a Lorentzian distribution (or non-relativistic Breit–Wigner distribution) [32, 34]:

$$n(E) = \frac{1}{\pi} \frac{\hbar \Gamma}{(E - \mu_{\mathrm{N}})^2 + (\hbar \Gamma)^2}, \tag{2.24}$$

where Γ is the total tunnel rate in and out of the QD.

Let us now assume that there is zero source-drain bias, i.e $\mu_s = \mu_d = \mu_r$, where μ_r is the combined source-drain 'reservoir' electro-chemical potential. The temperature of the source and drain electron reservoirs will broaden the occupation probability of the electron gas around chemical potential μ_r (for arbitrary conducting reservoir, 'r'). If $\hbar\Gamma \gg k_B T$ then the QD Coulomb peaks can be observed to broaden into a Lorentzian distribution originating from the broadening of μ_N within the QD. Instead, if the condition $\hbar\Gamma \ll k_B T \ll E_c$ is met, then the QD becomes sensitive to the electron temperature of its source and drain reservoirs, opening the door to thermometry experiments. In the latter case, the source-drain conductance of the QD is given as [11]:

$$G(\mu_N) = \frac{e^2}{4k_B T} \frac{\Gamma_s \Gamma_d}{\Gamma_s + \Gamma_d} \cosh^{-2}\left(\frac{\mu_N - \mu_r}{2k_B T}\right). \tag{2.25}$$

In this case, measuring the shape of the QD conductance curve against μ_N gives a readout of electron temperature. It is also possible to measure the electron temperature by probing the QD capacitively instead of resistively. The differential capacitance C_{pg} between the plunger gate and the QD is given by:

$$C_{pg} = \frac{dQ}{dV_{pg}} = C_{geom} + C_t, \tag{2.26}$$

where C_{geom} is the geometric capacitance and C_t is a subtle extra term: the tunnelling capacitance (also known as quantum or parametric capacitance, it will be referred to as the tunnelling capacitance in this thesis) [43, 44, 45, 46, 28, 47]. The tunnelling capacitance appears around the charge degeneracy point when there is cyclic tunnelling between the reservoir and QD. If $P_N^{(0)}$ is the probability that the current QD ground state μ_N is occupied, then, due to the relationships $e\alpha dV_{pg} = d\mu_N$ and $dQ = e\alpha dP_N^{(0)}$, the tunnelling capacitance can be given as:

$$C_t = (e\alpha)^2 \frac{\partial P_N^{(0)}}{\partial \mu_N}. \tag{2.27}$$

If there is the condition $\hbar\Gamma \ll k_B T$, the density of states within the QD can be approximated by a delta function $\delta(E - \mu_N)$. $P_N^{(0)}$ is given by the integral of

the electron distribution in the reservoir and the QD density of states:

$$P_N^{(0)}(\mu_N) = \int_{-\infty}^{\infty} \frac{1}{\exp\left(\frac{E-\mu_r}{k_B T}\right)+1} \delta(E-\mu_N)\mathrm{d}E = \frac{1}{\exp\left(\frac{\mu_N-\mu_r}{k_B T}\right)+1}, \quad (2.28)$$

which can be rearranged to:

$$P_N^{(0)}(\mu_N) = \frac{1}{2}\tanh\left(\frac{\mu_N-\mu_r}{2k_B T}\right) + \frac{1}{2}. \quad (2.29)$$

Combining this with Equation 2.27 gives the tunnelling capacitance as a function of μ_N:

$$C_t = \frac{(e\alpha)^2}{4k_B T}\cosh^{-2}\left(\frac{\mu_N-\mu_r}{2k_B T}\right), \quad (2.30)$$

which is the same temperature-sensitive shape as the conductance from Equation 2.25. This can be detected with non-galvanic alternating current (AC) reflectometry, which is discussed in Section 2.4.2. By measuring the the tunnelling capacitance with reflected AC signals, non-galvanic QD electron thermometry can be performed [27, 28].

2.1.5   Quantum Dot Coupled to a Single Reservoir

We now consider specifically a QD that is tunnel coupled (perhaps strongly) to a single reservoir, shown in Figure 2.4. This is the same situation as connecting the source-drain reservoirs together, or simply having no source-drain bias, i.e $V_{sd} = 0$. The reservoir electrons have a distribution in energy obeying Fermi-Dirac statistics described by Equation 2.23. This tells us the probability of finding an electron at energy E within the reservoir, which can be rearranged to:

$$F(E) = \frac{1}{2} - \frac{1}{2}\tanh\left(\frac{E-\mu}{2k_B T_e}\right), \quad (2.31)$$

where μ is the electrochemical potential of the reservoir, T_e is the electron temperature and k_B is the Boltzmann constant. The QD contains a ladder density of states separated by the charging energy E_c, as discussed in Sections 2.1.2. Each of these states is broadened in the form of a normalised Lorentzian, given by Equation 2.32. When the QD is Coulomb blockaded,
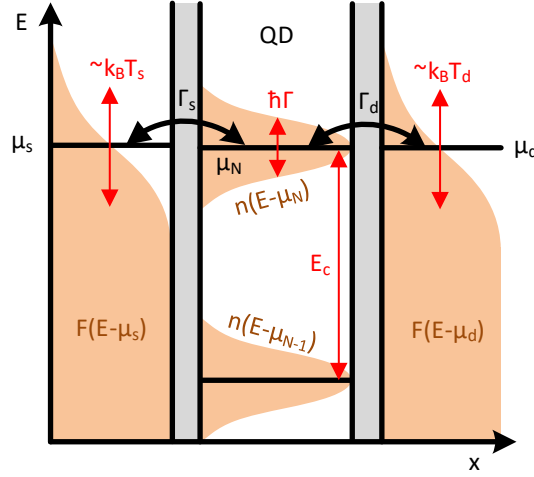
Figure 2.4: A diagram visualising the various energy scales in a QD-reservoir cou-
pled system. The reservoir's electron occupation is broadened following
a Fermi-Dirac distribution F (Equation 2.23) centred on the correspond-
ing chemical potential, visualised in orange. The width of this broaden-
ing is proportional to the temperature of the corresponding reservoir. In
the QD, each additional electron energy μ_N is separated by charging en-
ergy E_c and is lifetime broadened following a Lorentzian distribution n
(Equation 2.24), visualised in orange. This broadening has a full-width-
half-maximum equal to $2\hbar\Gamma$, where Γ is the total tunnelling rate via both
the QD barriers. For QD thermometry the condition $k_B T, \hbar\Gamma \ll E_c$ must
be met to create a full Coulomb blockade and allow a single additional
electron state μ_N to contribute to the conductance. If $\hbar\Gamma \gg k_B T$ then
the QD is not sensitive to the temperature of the reservoir electrons. If
$\hbar\Gamma \ll k_B T$ then the lifetime broadening can be ignored and the QD is
very sensitive to the temperature of the reservoir electrons. Note the en-
ergy scales on the diagram are for visual aid and are not to particular
scale.

we can consider just the next available energy level for adding an extra electron μ_N, which we will from now on label E_{QD}. Then the density of states within the QD can be described as:

$$n(E - E_{QD}) = \frac{1}{\pi} \frac{\hbar\Gamma}{(E - E_{QD})^2 + (\hbar\Gamma)^2}. \tag{2.32}$$

In the case where the tunnel broadening in the QD is significant when compared with the thermal broadening in the reservoir, then we need to modify Equation 2.28 to include both mechanisms in the QD occupation model. Therefore the probability P_{QD} of an excess electron occupying the QD energy level E_{QD} is given by the integral of the product of $n(E - E_{QD})$ and $F(E)$:

$$P_{QD}(E_{QD}) = \int_{-\infty}^{\infty} F(E)n(E - E_{QD})\mathrm{d}E. \tag{2.33}$$

This is mathematically equivalent to the convolution of the two functions F and n. The convolution operation expresses how the shape of one function is modified by the other, and has the general form of [48]:

$$(f * g)(t) = \int_{-\infty}^{\infty} f(\tau)g(t - \tau)\mathrm{d}\tau, \tag{2.34}$$

and the derivative of the convolution has the following identity:

$$(f * g)' = f * g' = f' * g. \tag{2.35}$$

Using the convolution operation, and because $n(E - E_{QD}) = n(E_{QD} - E)$, we can use Equation 2.32 to rewrite P_{QD} simply as:

$$P_{QD}(E_{QD}) = (F * n), \tag{2.36}$$

where the convolution is a function of E_{QD}. The QD tunneling capacitance C_t can then be defined by substituting Equation 2.36 into Equation 2.27:

$$C_t(E_{QD}) = (e\alpha)^2 (F * n)', \tag{2.37}$$

where the derivative is in respect to E_{QD}. Therefore, using the identity in Equation 2.35, we can say the tunnelling capacitance is:

$$C_t(E_{QD}) = (e\alpha)^2(F' * n). \tag{2.38}$$

The derivative of F with respect to E_{QD}, denoted F', is

$$F'(E_{QD}) = \frac{-1}{4k_B T_e} \cosh^{-2}\left(\frac{E_{QD} - \mu}{2k_B T_e}\right). \tag{2.39}$$

The spin degeneracy of the QD state can affect where the centre of the Coulomb peak is located. Consider the pair of dot states d and d', with N_d and $N_d + 1$ electrons, respectively. In the case where the QD is in state d, there are two possible situations. If N_d is an odd number, the N_d^{th} electron is in an incomplete spin 'shell', which gives state d a spin degeneracy of 2, up or down. An additional electron tunnelling into the QD must have opposite spin to complete the shell. In this case d' has a spin degeneracy of 1. In the other case that N_d is an even number, the N_d^{th} electron completes the spin 'shell', which gives state d a spin degeneracy of 1. An additional electron tunnelling into the QD can have either spin up or down to complete the shell. In this case d' has a spin degeneracy of 2.

In either case, the imbalance of spin degeneracy between states d and d' mean that the charge equality point, where $P_{QD} = 1/2$, is shifted away from the charge degeneracy. The charge equality occurs with the following condition [28, 49]:

$$E_{QD} = \mu \pm k_B T \ln 2, \tag{2.40}$$

whereas the charge degeneracy occurs when $E_{QD} = \mu$. The sign of the second term is positive or negative depending on whether the N_d is even or odd. From Equation 2.27 it follows that the tunnelling capacitance is maximum at the charge equality point.

2.1.6 Electron-Phonon Coupling

When discussing the temperature T of a conducting material, there are actually several thermal bodies at play which all affect each other. The important

elements for this thesis are phonon temperature T_p and electron temperature T_e. Above the Debye temperature, the phonons and electrons are scattering off each other and are well thermalised, meaning $T_\mathrm{p} \approx T_\mathrm{e}$. This means the electrons can be assumed to have the same temperature as the cryostat base temperature. However, as discussed in Section 2.5, below the Debye temperature the lattice phonons will begin to freeze out. The heat flow from the phonon bath to the electrons due to electron-phonon coupling is given by [50, 30, 20]

$$\dot{Q}_{\mathrm{p}-\mathrm{e}} = \Sigma V (T_\mathrm{p}^n - T_\mathrm{e}^n), \qquad (2.41)$$

where V is the material volume and n is typically 5 for materials like copper. Therefore, as we go to sub-Kelvin temperatures, the bath of electrons within a reservoir is increasingly thermally isolated from the lattice phonons. This severely limits electron cooling, and so electrical noise and parasitic heating can elevate the electron temperature significantly. It is common therefore to measure elevated electron temperatures in low temperature circuits. In Chapters 3 and 4, the measured fridge temperature T_f is interpreted as equal to the phonon temperature T_p.

2.2   Modelling

Model fitting to data has become a standard technique to extract useful information and explain experimental observations, and usually such techniques are only mentioned briefly in a text. In this work, the process of fitting a model to data is used extensively in Chapter 4, for both the calibration of an electron thermometer and the subsequent electron temperature readout. The fitting procedure requires well defined confidence to be used reasonably, for example the electron temperature readout is meaningless without a well determined uncertainty. Therefore the methods used of fitting to experimental data and generating uncertainty in the parameter estimates are detailed here.

The background theory for the model fitting approach used is described in Section 2.2.1, and the method for determining the accuracy of the fit parameter estimates is described in Section 2.2.2.

2.2.1 Chi-square Fitting

Consider a set of N data points (x_i, y_i), where $i = 0, ..., N - 1$. We want to fit a model $y(x)$, with M adjustable parameters a_j, where $j = 0, ..., M - 1$, denoted by:

$$y(x) = y(x|a_0, ..., a_{M-1}) \tag{2.42}$$

where y is dependent on the parameters on the right hand side of the vertical bar. If we assume that each data point has a measurement error that is independently random within a normal Gaussian distribution with standard deviation σ, then the probability of obtaining the data set measured, with a fixed uncertainty of Δy, is proportional to:

$$P(\text{data}|\text{model}) \propto \prod_{i=0}^{N-1} \left\{ \exp\left[-\frac{1}{2} \left(\frac{y_i - y(x_i|a_0, ..., a_{M-1})}{\sigma} \right) \right] \Delta y \right\}, \tag{2.43}$$

for a given estimate of the a_j parameters [51]. A successful fit of the model to data will estimate values of the a_j parameters such that $P(\text{data}|\text{model})$ is maximised. This is mathematically equivalent to minimising the negative logarithm of Equation 2.43:

$$\left[\sum_{i=0}^{N-1} \frac{[y_i - y(x_i|a_0, ..., a_{M-1})]^2}{2\sigma^2} \right] - N\log\Delta y. \tag{2.44}$$

Since N, σ and Δy are constants, we can equally say the fit process is minimising the sum of the squared residuals between the model and the data:

$$R^2 = \sum_{i=0}^{N-1} [y_i - y(x_i|a_0, ..., a_{M-1})]^2. \tag{2.45}$$

Minimising R^2 should reveal the fitted values for the a_j parameters. If for each data point i we know the standard deviation of its measurement σ_i, then we can normalise R^2 to a more useful parameter, χ^2_{N-M}, which normalises the statistical independence of each data point:

$$\chi^2_{N-M} = \sum_{i=0}^{N-1} \left[\frac{y_i - y(x_i|a_0, ..., a_{M-1})}{\sigma_i} \right]^2, \tag{2.46}$$

where χ^2_{N-M} represents the chi-square distribution for N-M degrees of freedom. This can be minimised to obtain the set of a_j parameter estimates. If we have two separate instances of chi-square fitting and we wish to compare them, then χ^2 needs to be divided by the number of degrees of freedom, $N - M$, like so:

$$\chi^2 = \sum_{i=0}^{N-1} \left[\frac{y_i - y(x_i|a_0, ..., a_{M-1})}{\sigma_i(N-M)} \right]^2. \tag{2.47}$$

2.2.2 Model Fit Error

After a model fit is complete from minimising Equation 2.47, it is important to know the confidence limits for the set of a_j parameter estimates. One approach is to use a constant chi-square boundary to define the confidence limits, which is particularly useful if the limits may be asymmetrical around the estimate [51].

Assume a constant standard deviation for data point, i.e. $\sigma_i = \sigma$ for all i. The minimum value of χ^2, which we will label χ^2_{min}, corresponds to the final fit estimate for the a_j parameters, typically $\chi^2_{min} \sim 1$. To work out the certainty of the a_j estimates, a constant M-dimensional confidence boundary of $\chi^2_{min} + 1$ surrounds χ^2_{min}, creating a region which represents one standard deviation of confidence, i.e 68.3% certainty for the combined estimation of all a_j parameters.

2.3 Cryostats

All the experiments discussed in Chapters 3, 4 and 5 were performed in cryogenic environments. Around the turn of the 20th Century many low temperature experimental milestones had been accomplished, including the first liquefaction of oxygen, hydrogen, nitrogen and (finally) helium gases, greatly aided by the conception of the dewar. The latent heat from the evaporation of these liquid gases creates powerful cooling effects, with helium evaporation creating temperatures down to $\sim 1\,\text{K}$. This was advanced upon even further by the mixing of the two helium isotopes to obtain even lower temperatures [52, 10], and the mid-20th century brought the experimental realisation of the dilution refrigerator for the first time, in the Kamerlingh

Onnes Laboratorium at Leiden University [53]. The dilution refrigerator has enjoyed a rapid and interesting developmental history over the last 50 years, in which Lancaster University has played a significant part. Thanks to the recent rise of commercial cryogen-free dilution refrigeration, many options are now available for simple-operation milliKelvin environments.

Consider a pumped-on liquid bath where n particles per time are moved to the vapour phase. The cooling power $\dot{Q}_c$ is given by

$$\dot{Q}_c = \dot{n}\Delta H = \dot{n}L, \tag{2.48}$$

where L is the latent heat of evaporation and ΔH is the enthalpy [30]. For an evaporating cryogenic liquid $\Delta H = H_{\text{liq}} - H_{\text{vap}}$ where H_{liq} (H_{vap}) is the enthalpy for the liquid (vapour) phase. Assuming the liquid is pumped with a constant-volume pumping speed, the ideal gas law determines that the particle flow $\dot{n}$ across the liquid–vapour boundary is proportional to the vapour pressure $P_{\text{vap}} \propto e^{-L/RT}$, where R is the ideal gas constant. This gives a cooling power which has the same temperature dependence:

$$Q_c \propto e^{-1/T}. \tag{2.49}$$

This shows that the cooling power decreases rapidly with decreasing temperature because of an equivalent drop in vapour pressure, which reduces the impact of the pumping. When there is almost no vapour left, the system is at the minimum temperature obtainable by pumping on a bath of an evaporating cryogenic liquid. This limit is reached when the refrigeration due to evaporation of atoms is balanced by heat leaks flowing into the bath. The practical low-temperature limits determined by experimental parameters are typically about 1.3 K for ^{4}He and 0.3 K for ^{3}He (^{3}He and ^{4}He represent the two isotopes of He, where ^{3}He has two protons and one neutron, and ^{3}He has two protons and two neutrons). For ^{3}He–^{4}He dilution refrigeration the enthalpy ΔH of mixing is given by the integral of the difference in specific heat capacity for the ^{3}He concentrated and dilute phases:

$$\Delta H \propto \int \Delta C dT \tag{2.50}$$

The specific heat capacity for both the concentrated and dilute phases has a

temperature dependence proportional to *T* at low temperatures, so the cooling has a temperature dependence given by:

$$Q_{\text{c}} \propto T^2 \qquad\qquad (2.51)$$

Here the temperature dependence of the cooling power is weaker than that of the evaporation process, which gives it an advantage at lower temperatures and, with the right environment, the ability to cool to lower temperatures.

In this thesis, a total of three cryostat systems were used, all of which are visualised in Figure 2.5. First a 1 K pot fridge custom-built by Oxford Instruments, called the '**IO**'. This system is a 'dry' fridge, and so all the cryogen plumbing is within a vacuum. The IO cryostat uses an in-series double pulse tube cryocooler to cool down to 4 K, at which point ^{4}He gas is pumped through the pot via a closed loop and scroll pump. Initially the outgoing gas expands and cools the pot. When the incoming pressure is high enough ($\sim$ 0.1bar), the ^{4}He gas will begin to condense and pool up in the pot. The liquid ^{4}He evaporates, providing cooling power described with Equation 2.49, which cools the pot further. The evaporated ^{4}He is pumped back into the cryostat via the scroll pump and so the cooling continues. The base temperature typically reaches 1.3 K. This can be elevated with a proportional–integral–derivative (PID) controlled heater element mounted on the 1 K plate, which inputs heat to counter the cooling power of the cryostat, thereby causing the cryostat to settle at a new temperature.

Another fridge that is used is a commercial dilution refrigerator built by BlueFors, called the '**LD250**'. This system is also a dry fridge, and so all the cryogen plumbing is within a vacuum. The LD250 cryostat uses an in-series double pulse tube cryocooler to cool down to around 4 K. A mixture of ^{3}He and ^{4}He is circulated through the fridge via a scroll and turbo pump. A compressor is used to create a high incoming pressure, which causes the mixture to condense and liquefy into the mixing chamber. When the mixture is in full circulation it separates within the mixing chamber into the ^{3}He condensed and dilute phases, which produces cooling down to milliKelvin temperatures via Equation 2.51. The ^{3}He dilute phase pools up to the still, where ^{3}He evaporates and is pumped out, providing cooling to the still plate via Equation 2.49. The outgoing dilute phase is thermally connected to the
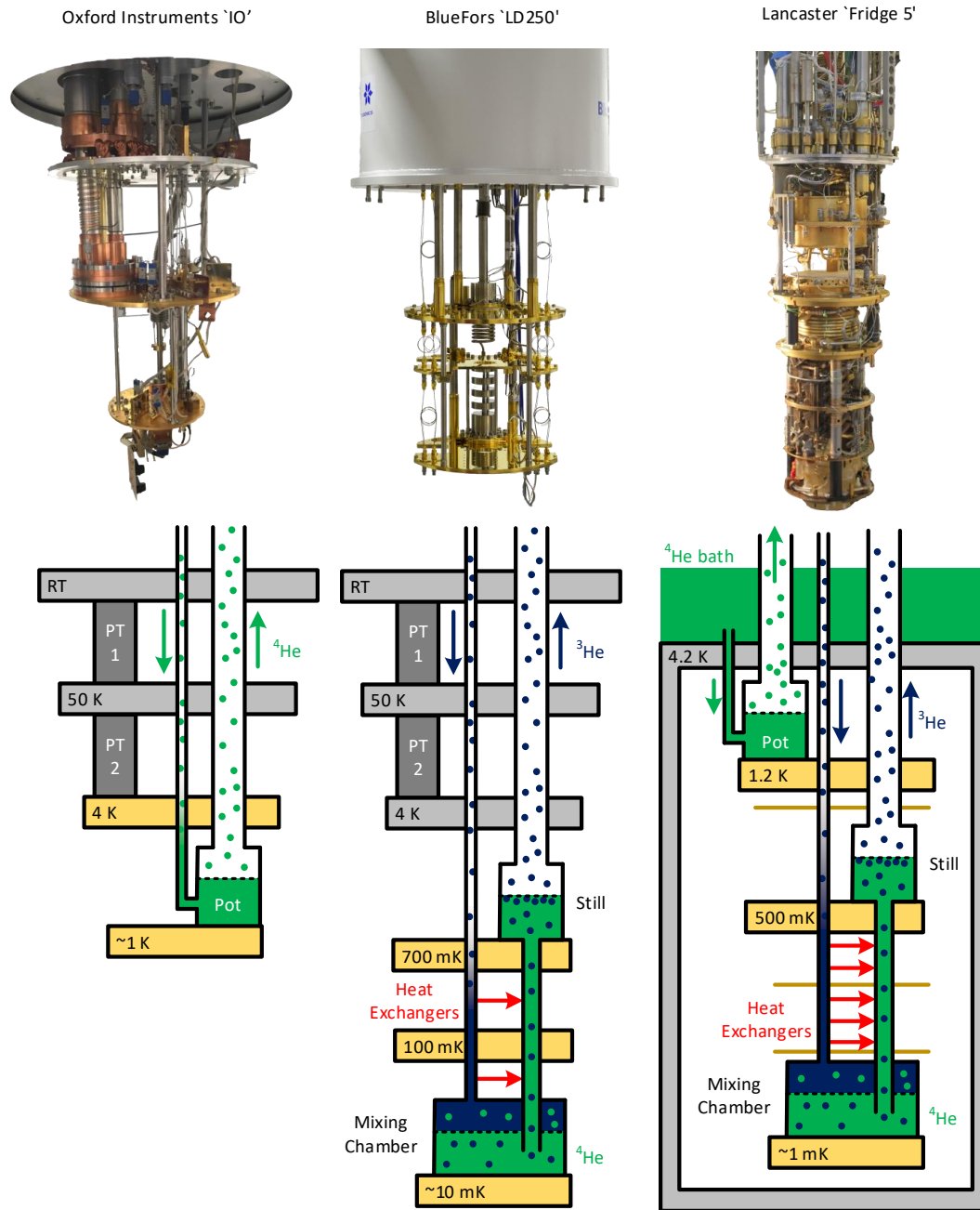
Figure 2.5: Photographs and schematic of the three cryostat systems used in the experiments detailed within this thesis. The left-most fridge is the 'IO', a custom built dry 1 K pot fridge by Oxford Instruments. It uses an in-series double pulse tube cryocooler, labelled 'PT 1' and 'PT 2' to cool down to ~ 4 K. ^{4}He is pumped through a pot to provide evaporative cooling power, creating a base temperature of 1.3 K. The centre fridge is the 'LD250', a commercial dry dilution refrigerator built by BlueFors. It also achieves ~ 4 K using a pulse tube. This fridge features a dilution unit, where ^{3}He dilutes in ^{4}He within the mixing chamber and separates into the rich and dilute ^{3}He phases. This provides cooling power, creating a base temperature of 8 mK. The right fridge is 'Fridge 5', a home-made wet fridge built at Lancaster University. This uses two concentric baths of nitrogen and helium to cool to 4.2 K. A ^{4}He pot is used to provide evaporative cooling power to 1.2 K, then a dilution unit creates a base temperature of 2.3 mK. The red arrows show heat exchangers which allow heat to transfer from the incoming mixture to the colder outgoing liquid.

incoming mixture via heat exchangers. This cools down the incoming mixture and allows the phase separation to create even lower temperatures. The base temperature typically reaches 8 mK. This can be elevated by removing a small amount of mixture from the closed loop, which reduces $\dot{n}$, and therefore the cooling power via Equation 2.48. A reduction in cooling power means the mixing plate will settle at a new, higher temperature.

The final cryostat discussed here is a Lancaster-built 'wet' dilution refrigerator, affectionately named '**Fridge 5**'. This works in a similar way to the LD250, however because it is a wet fridge it does not require a pulse tube for pre-cooling. Instead it relies upon a huge 3 m high dewar which contains a variety of cans in a matryoshka-doll packing style [29]. The outer can contains a vaccum which protects a bucket of evaporating nitrogen, which cools the inner can to 77 K, and works as a cryoshield to protect the inner layers from radiation. The inner can contains a volume connected to the vacuum, which houses a bucket of evaporating ^{4}He, shown in Figure 2.5, which cools the cryostat insert to 4.2 K. From there a ^{4}He pot fridge cools the insert down to 1 K via Equation 2.49, and the mixing chamber phase separation produces cooling down to milliKelvin temperatures via Equation 2.51. The nested baths of nitrogen and helium produce a huge amount of cooling power, and less noise than a pulse tube. Combined with excellent heat exchangers, this fridge can typically reach a base temperature of 2.3 mK.

2.4   Radio-Frequency Electronics

Radio-frequency (RF) electronics is a well established discipline that has an excellent range of uses for interacting with low temperature experiments. High frequency tones or quick pulses can be used to control, and readout from, quantum circuits [54, 55]. This Section will discuss the electronic theory for the apparatus and techniques used in Chapters 3 and 4, where RF techniques are used to measure the characteristics of a QD and perform electron thermometry.

First, the fundamental concepts of wave transmission through coaxial lines and reflection off an impedance load is described in Section 2.4.1. Applying this to the readout of a variable capacitance is described in Section 2.4.2.
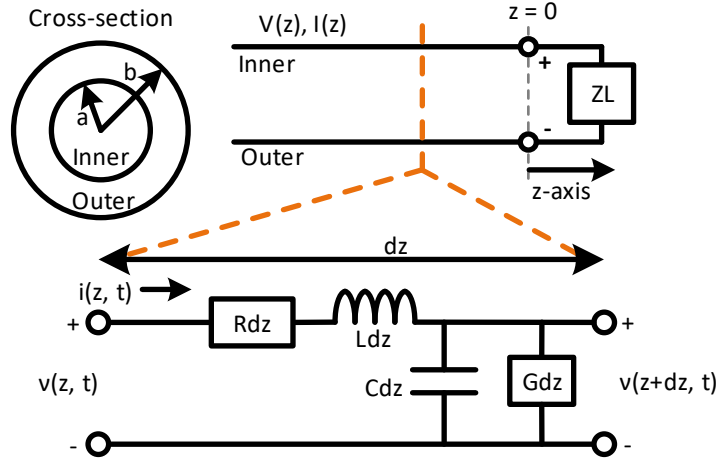
Figure 2.6: Top-left: x-y axis cross section of a coaxial transmission line with inner conductor radius *a* and outer conductor radius *b*. **Top-right:** A schematic representing the coaxial transmission line with voltage *V* and current *I* dependent on location along the *z* axis. **Bottom:** A schematic representing an infinitesimally small section of the coaxial line d*z*. The transmission line per unit length has a series resistance *R*, series inductance *L*, shunt conductance *G* and shunt capacitance *C*.

Finally, details are included for designing a coplanar waveguide in Section 2.4.3.

2.4.1 Transmission Lines and Termination

RF electronic signals are transmitted around the lab and into cryogenic environments using coaxial cable. The coaxial geometry acts as an excellent waveguide, allowing high-frequency signals to propagate over long distances.

Consider an infinitesimally small section of a two-wire transmission line which per unit length has a series resistance *R*, series inductance *L*, shunt conductance *G* and shunt capacitance *C* (Figure 2.6). From Kirchoff's voltage and current laws, we can say [56]:

$$\frac{\partial v(z,t)}{\partial z} = -Ri(z,t) - L\frac{\partial i(z,t)}{\partial t}, \tag{2.52}$$

$$\frac{\partial i(z,t)}{\partial z} = -Gv(z,t) - C\frac{\partial v(z,t)}{\partial t}, \tag{2.53}$$

where $v(z, t)$ and $i(z, t)$ is the voltage and current at point z along the transmission cable at time t. Switching from a time domain to a sinusoidal steady state condition with frequency ω, the transmission line voltage $V(z)$ and current $I(z)$ wave Equations are then

$$\frac{dV(z)}{dz} - \gamma^2 V(z) = 0, \tag{2.54}$$

$$\frac{dI(z)}{dz} - \gamma^2 I(z) = 0, \tag{2.55}$$

where $\gamma = \sqrt{(R + j\omega L)(G + j\omega C)}$ and j is the imaginary unit. The general solutions to Equations 2.54 and 2.55 are:

$$V(z) = V_0^+ e^{-\gamma z} + V_0^- e^{\gamma z}, \tag{2.56}$$

$$I(z) = I_0^+ e^{-\gamma z} + I_0^- e^{\gamma z}. \tag{2.57}$$

The $e^{-\gamma z}$ terms represent wave propagation in the $+z$ direction with voltage (current) magnitude V_0^+ (I_0^+) and the $e^{+\gamma z}$ terms represent wave propagation in the $-z$ direction with voltage (current) magnitude V_0^- (I_0^-). The transmission line has a characteristic impedance Z_0, given by:

$$Z_0 = \frac{V_0^+}{I_0^+} = \frac{-V_0^-}{I_0^-} = \sqrt{\frac{R + j\omega L}{G + j\omega C}} \tag{2.58}$$

which, for an assumed lossless line, becomes $Z_0 = \sqrt{L/C}$.

For a co-axial transmission line, with inner radius a and outer radius b (as shown in Figure 2.6), the electronic parameters are given as [56]:

$$L = \frac{\mu}{2\pi} \ln \left(\frac{a}{b} \right) \tag{2.59}$$

$$R = \frac{R_s}{2\pi} \left(\frac{1}{a} + \frac{1}{b} \right) \tag{2.60}$$

$$C = \frac{2\pi\epsilon'}{\ln \left(\frac{a}{b} \right)} \tag{2.61}$$

$$G = \frac{2\pi\omega\epsilon''}{\ln \left(\frac{a}{b} \right)} \tag{2.62}$$

where R_s is the surface resistance of the conductors. The insulator between the two concentric lines has a complex permittivity $\epsilon = \epsilon' - j\epsilon''$ and permeability μ. Now consider the termination of a lossless transmission line at $z = 0$ with a load impedance Z_L. We can say that the load impedance must be equal to $Z_\mathrm{L} = V(0)/I(0)$. Using this with Equation 2.58 gives:

$$Z_\mathrm{L} = \frac{V_0^+ + V_0^-}{I_0^+ + I_0^-} = \frac{V_0^+ + V_0^-}{V_0^+ - V_0^-}Z_0 \tag{2.63}$$

Rearranging this for V_0^- gives

$$V_0^- = \frac{Z_0 - Z_L}{Z_0 + Z_L}V_0^+ = |R|V_0^+ \tag{2.64}$$

The term $|R|$ is called the voltage reflection coefficient and tells us the amplitude of the reflected voltage signal V_0^- normalised to the amplitude of the incoming wave V_0^+. To avoid unnecessary loss and deliver maximum power, $|R|$ should be minimised. To do this, we need to minimise $Z_0 - Z_L$, or equivalently, make Z_L equal to Z_0. This process is called impedance matching, and improves the signal to noise ratio of the circuit. Consider the components in an equivalent circuit for Z_L. The two reactive constituents that can be added are the capacitor and the inductor, with an impedance of $Z_\mathrm{c} = 1/i\omega C$ and $Z_\mathrm{l} = i\omega L$ respectively [57]. A resistive constituent has an impedance of $Z_\mathrm{R} = R$. For a particular frequency ω, the careful adjustment of these constituent components allows Z_L to be matched to Z_0, minimising $|R|$. Impedance matching can be achieved with the aid of a Smith chart, for a chosen frequency ω.

2.4.2 Phase Readout of Capacitance

RF reflectometry is a good tool for measuring subtle changes in parameters that make up the load impedance Z_L. Very small changes in capacitance can be detected using an electrical resonator as the load impedance [55, 43, 58, 59, 60, 28, 61]. Consider the circuit shown in Figure 2.7. The total load impedance of this circuit is

$$Z_\mathrm{L} = \frac{1}{i\omega C_\mathrm{c}} + \frac{1}{i\omega(C + C_\mathrm{v}) + \frac{1}{i\omega L}}, \tag{2.65}$$
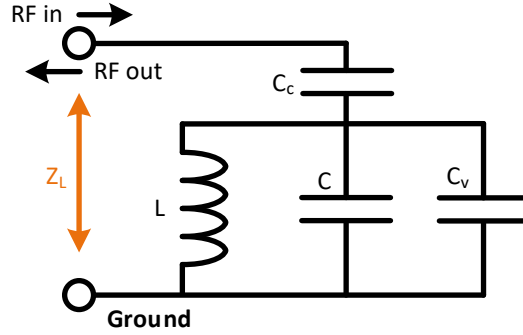
Figure 2.7: A schematic showing an example load impedance Z_L for an electrical resonator. L and C are the resonator inductor and capacitor respectively. C_c is a coupling capacitor for non-galvanic RF connection. C_v is a variable capacitance the circuit is designed to detect.

where C_c is the 'coupling' gateway capacitor for the signal, C is a constant capacitance, L is a constant inductance and C_v is a variable capacitance that we want to detect. When $C_\mathrm{v} = 0$, the resonant frequency of the impedance is given by:

$$\omega_0 = 1/\sqrt{L(C + C_\mathrm{c})}. \tag{2.66}$$

The voltage reflection amplitude $|R|$ from Equation 2.64 can be rewritten as:

$$|R| = e^{i\Delta\phi}, \tag{2.67}$$

where $\Delta\phi$ is the phase between the incoming and reflected RF waves. This difference in phase is equal to:

$$\Delta\phi = \arctan\left(\frac{2Q(\omega - \omega_0)}{\omega_0}\right), \tag{2.68}$$

where Q is the unloaded Q factor, which describes how underdamped the resonator is. Consider the case where the circuit is driven at ω_0 and $C_\mathrm{v} \neq 0$. The resonant frequency will then shift to $\omega_1 = 1/\sqrt{L(C + C_\mathrm{c} + C_\mathrm{v})}$. If this shift occurs whilst the resonator is driven at the bare resonance frequency ω_0, then the corresponding change in reflected wave phase would be equal to:

$$\Delta\phi = \arctan\left(\frac{2QC_\mathrm{v}}{C + C_\mathrm{c}}\right). \tag{2.69}$$
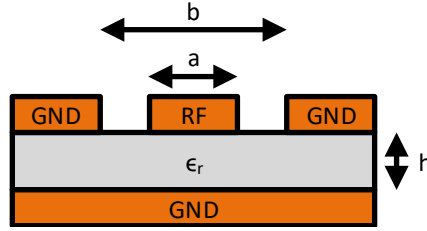
Figure 2.8: A cross section of a coplanar waveguide line on a PCB. The line has width *a* and, including the gaps, total width *b*. The board has a dielectric with thickness *h* and relative permittivity ϵ_r between the two conducting layers.

If $C_v \ll C + C_c$, then the small angle approximation gives:

$$\Delta\phi \approx \frac{2Q}{C + C_c} C_v \tag{2.70}$$

In this case, the RF phase readout is proportional to a small change in capacitance $\Delta\phi \propto C_v$. For this to work, like in all experiments, the signal we wish to detect must be greater than the noise floor of the equipment. To help amplify the signal the circuit must be designed to minimise the background capacitance $C + C_c$ and maximise Q with good impedance matching, as this increases the responsivity of $\Delta\phi$ to C_v.

2.4.3 Coplanar Waveguide Design

Printed circuit boards (PCBs) are extremely useful in RF circuits as they are highly customisable and provide an excellent interface between transmission lines and devices in low temperature environments.

On the PCB surface, a coplanar waveguide with conductor width *a* and total 'conductor and gap' width *b*, running on a double sided PCB with thickness *h* and relative permittivity ϵ_r (as shown in Figure 2.8), will have a characteristic impedance given by the following formula [62, 63]:

$$Z_0 = \frac{60\pi}{\sqrt{\epsilon_{\text{eff}}}} \left(\frac{K(a/b)}{K(\sqrt{1 - (a/b)^2})} + \frac{K(k_1)}{K(\sqrt{1 - k_1^2})} \right)^{-1} \tag{2.71}$$

where $K(k)$ is the complete elliptic integral of the first kind, which can be defined as

$$K(k) = \frac{\pi}{2} \sum_{n=0}^{\infty} \left[\frac{(2n-1)!!}{(2n)!!} \right]^2 k^{2n}, \tag{2.72}$$

where the operation '!!' represents a double factorial. k_1 is defined by

$$k_1 = \frac{\tanh(\pi a/4h)}{\tanh(\pi b/4h)}, \tag{2.73}$$

and the effective permittivity is

$$\epsilon_{\text{eff}} = \left(1 + \epsilon_{\text{r}} \frac{K(\sqrt{1-(a/b)^2})}{K(a/b)} \frac{K(k_1)}{K(\sqrt{1-(k_1)^2})} \right) \left(1 + \frac{K(\sqrt{1-(a/b)^2})}{K(a/b)} \frac{K(k_1)}{K(\sqrt{1-(k_1)^2})} \right)^{-1}. \tag{2.74}$$

The effective permittivity can be thought of as the dielectric constant of a theoretical homogeneous medium that surrounds the waveguide and replaces the real dielectric with finite thickness h.

These equations may look unpleasant, yet it is a useful tool to help impedance match the PCB coplanar waveguide with the transmission lines. Aiming for the lab standard characteristic impedance of $Z_0 = 50\Omega$ is important so as to give minimal reflection at the PCB-transmission line interface for both incoming and outgoing waves.

2.5   Insulator Thermal Conductivity

A cryostat's base temperature is limited by the heat transferred from the warm surroundings to the cold parts of the equipment, or the 'heat leak'. A heat leak reduces the cooling power of the fridge and can elevate the base temperature. To reduce unwanted heat leak, there needs to be good thermal isolation between fridge components, and the warm surroundings. Thermal insulator materials that work well in low temperature environments are therefore useful for providing isolation and structural support for cryogenic components, for example radiation spacers and support rods. Insulators like this are useful in all of cryogenics, but also for the progression of quantum circuits and computing, which relies on isolated temperature for operation and coherence. Popular choices for these materials are plastics,
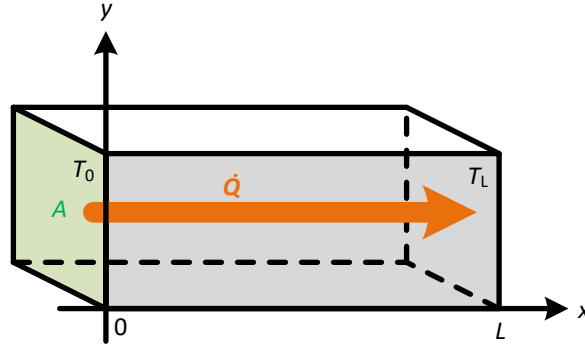
Figure 2.9: Simple picture of an insulator with thermal connection area A on both ends, and length L. At $x = 0$ and $x = $ L, the insulator is thermally coupled to a reservoir at temperature T_0 and T_L, respectively. $\dot{Q}$ is the heat flow from $x = 0$ to $x = $ L.

such as Vespel, or ceramics, such as Macor [30, 64]. This section outlines the theory of the thermal conductivity power law, and how it can be used to analyse the new solid-void insulators tested in Chapter 5.

For an insulating solid, the transfer of heat is mostly, and sometimes entirely, dependent on phonons travelling through the material. Consider a non-magnetic crystalline insulator with area A and end-to-end length L (Figure 2.9). At low temperatures the phonon density of states is parabolic as a function of frequency due to the linear dispersion relation for phonons. In the Debye model, this is described by [65]:

$$g_{\text{ph}}(\omega) = \begin{cases} \frac{3AL}{2\pi^2 v_{\text{s}}^3}\omega^2, & \omega \leq \omega_{\text{D}}, \\ 0, & \omega > \omega_{\text{D}}, \end{cases} \tag{2.75}$$

where v_{s} is the average value of longitudinal and transversal velocity of sound. The phonon density of states $g_{\text{ph}}(\omega)$ must contain all phonon frequencies below the Debye frequency ω_{D}. For an insulator material with atom density N_0, it must therefore satisfy

$$\int_0^{\omega_D} g_{\text{ph}}(\omega)\mathrm{d}\omega = 3N_0 \tag{2.76}$$

The factor of 3 comes from the three degrees of freedom for each atom's potential and kinetic energy. We can therefore rewrite the phonon density of

Material	$\lambda \, [\mathrm{Wm^{-1}K^{-(n+1)}}]$	n
Macor [67]	5.83×10^{-3}	2.24
Vespel SP 1 [68, 30]	1.8×10^{-3}	1.2
Vespel SP 22 [68, 30]	1.7×10^{-3}	2.0
Wood [69]	9.3×10^{-3}	2.7
AXM-5Q [64]	1.2×10^{-3}	1.2

Table 2.1: Some experimental sub-Kelvin parameters for material thermal conductivity power law model $\kappa = \lambda T^n \, \mathrm{Wm^{-1}K^{-1}}$.

states below the Debye frequency as:

$$g_{\mathrm{ph}}(\omega) = 9N_0 \omega^2 / \omega_{\mathrm{D}}^3. \tag{2.77}$$

The cut-off Debye frequency ω_{D}, has a corresponding temperature metric, the Deybe temperature $\Theta_{\mathrm{D}} = (\hbar/k_{\mathrm{B}})\omega_{\mathrm{D}}$. Below the Debye temperature, the phonons begin to freeze out and heat flow is restrained.

To calculate the specific heat capacity of the insulator material, we first consider the internal energy of lattice vibration, which is given by:

$$U(T) = \int_0^{\hbar \omega_{\mathrm{D}}} \hbar \omega g_{\mathrm{ph}}(\omega) F(\omega, T) \mathrm{d}\omega, \tag{2.78}$$

where $F(\omega, T)$ is the Bose–Einstein distribution function [66]. The specific heat capacity is defined as $C_{\mathrm{v}} = \partial U / \partial T$, therefore combining Equations 2.77 and 2.78 we can define the specific heat of an insulator:

$$C_{\mathrm{v}} = 9N_0 k_{\mathrm{B}} \left(\frac{T}{\Theta_{\mathrm{D}}}\right)^3 \int_0^{x_{\mathrm{D}}} \frac{x^4 e^x}{(e^x - 1)^2} \mathrm{d}x, \tag{2.79}$$

where $x = \hbar\omega/k_{\mathrm{B}}T$ and $x_{\mathrm{D}} = \hbar\omega_{\mathrm{D}}/k_{\mathrm{B}}T$. Solving the integral then gives us the specific heat:

$$C_{\mathrm{v}} = \frac{12\pi^4}{5} N_0 k_{\mathrm{B}} \left(\frac{T}{\Theta_{\mathrm{D}}}\right)^3. \tag{2.80}$$

Now consider the material thermal conductance coefficient κ, which is defined within the following expression [66, 30]:

$$\frac{\dot{Q}}{A} = \kappa \nabla T. \tag{2.81}$$

Using a simple description of heat conduction where we consider the insulator to contain an ideal gas of phonons, we can describe the energy transfer using the Equations of the kinetic theory of gases. In this approximation, the thermal conductivity is given by

$$\kappa = \frac{1}{3}C_\mathrm{v}v_\mathrm{s}\lambda_\mathrm{ph}, \tag{2.82}$$

where λ_ph is the mean-free path of the phonons. When $T \ll \Theta_\mathrm{D}$, Equation 2.80 shows that $C_\mathrm{v} \propto T^3$. But the thermal conductivity temperature dependence is also linked to the mean-free path of the phonons. If we continue to consider a crystalline insulator, at very low temperatures there are very few phonon-phonon scattering events. This creates a large λ_ph, and therefore most phonon scattering occurs at the crystallite boundaries. This removes the temperature dependence of λ_ph and therefore $\kappa \propto T^3$. However the insulator materials we wish to test are produced from amorphous plastics which are strongly disordered, and therefore the mean free path determined by the scattering of phonons on defects can become very small, even approaching atomic distances. This reduces the thermal conductivity considerably, but also alters the temperature dependence of λ_ph by introducing more scattering events. Phonon–dislocation scattering and phonon–point defect Rayleigh scattering can create a temperature dependence of $\lambda_\mathrm{ph} \propto T^{-1}$ and $\propto T^{-4}$ respectively. To include these scattering events in the model, we define the thermal conductivity power law:

$$\kappa = \lambda T^n, \tag{2.83}$$

where λ is the thermal conductivity scaling constant with units $[\mathrm{Wm^{-1}K^{-(n+1)}}]$, and n is the exponent of the insulator temperature T. We know that $n \approx 3$ from Equation 2.80, but also that for amorphous plastics with lots of phonon scattering this parameter will typically be reduced to around $n \approx 2$. Some examples of insulator thermal conductivity and temperature dependence when $T < 1\,\mathrm{K}$ are given in Table 2.1. To experimentally measure κ, we consider the heat flow $\dot{Q}$ from one end of a plastic insulator rod where $x = 0$, to the other end where $x = L$:

$$\dot{Q} = \int_0^L \dot{q}\,\mathrm{d}x = \int_{T_0}^{T_\mathrm{L}} \kappa(T)\,\mathrm{d}T \tag{2.84}$$

where T_0 and T_L are the temperature at $x = 0$ and $x = L$, respectively. Evaluating this integral with Equation 2.83 gives

$$\dot{Q} = \lambda \frac{A}{L} \frac{(T_L^{n+1} - T_0^{n+1})}{n+1}. \tag{2.85}$$

By monitoring the temperatures on either side of the insulator with respect to the total heat flow, we can calculate λ and n, which defines the thermal conductivity power law in Equation 2.83.

Chapter 3

Building a Single-Wire Quantum Dot Thermometer

This chapter details the construction of a QD electron thermometer, including readout circuitry, used in the experiments described in Chapter 4. The thermometer is built to be calibrated and operated using only non-galvanic measurements, and require only a single gate connection to the QD. This involves building a dedicated RF phase reflectometry circuit that is capacitively coupled to the QD. This chapter includes a close look at the devices and apparatus used in Sections 3.1 and 3.2, the construction and optimisation of the RF reflectometry circuit in Section 3.3, and the behaviour of the QD-reservoir system in Section 3.4.

3.1 Devices

The key component of the electron thermometer is a silicon chip that contains a gated QD, tunnel coupled to two conducting reservoirs, whose electron tunnelling properties tells us the temperature of the electrons within the reservoirs. Therefore the type of device used to define the QD and it's tunnel barriers is fundamental to the effectiveness of the thermometer. In this section we will first discuss briefly the intended quantum system for the thermometer, and then the realisation.

Consider the a QD coupled to a reservoir, shown in Figure 3.1. The theory of this system is discussed in Section 2.1.5. It has a differential capacitance to ground from the perceptive of the QD top gate given by Equation 2.26. One
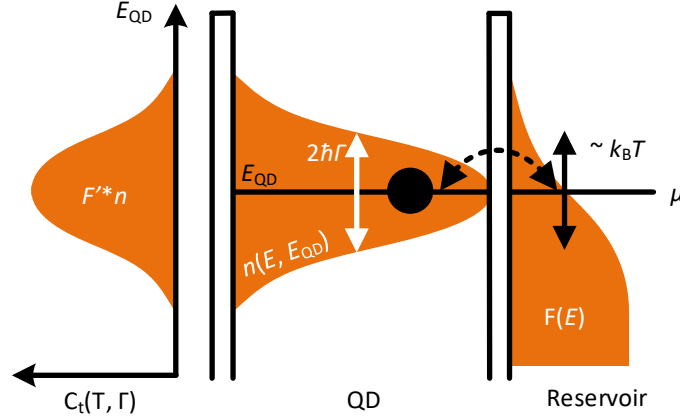
Figure 3.1: Energy diagram of a QD tunnel-coupled to a conducting reservoir. The reservoir has an average occupation of electron states given by the Fermi-Dirac distribution F, described by Equation 2.31. The Fermi-Dirac distribution is broadened proportional to $k_B T_e$, where T_e is the electron temperature. The QD energy level E_{QD} is broadened by tunnel coupling to the reservoir, with a density of states n described by Equation 2.32. The FWHM of n is $2\hbar\Gamma$, where Γ is the tunnelling rate between the QD and the reservoir. The tunnelling capacitance C_t as a function of E_{QD} has a shape proportional to $F' * n$.

element of this is the tunnelling capacitance C_t, given by Equation 2.38. This parameter is non-zero when the QD is on a Coulomb peak and is sensitive to the broadening of the peak. The relationship $\partial V_{tg} = -\partial E_{QD}/e\alpha$ is used to convert the theory outlined in Section 2.1.5 from energy space into voltage space, where $\alpha = C_{tg}/C_\Sigma$ is the top gate QD lever arm and C_Σ is the total QD capacitance. Therefore the tunnelling capacitance can be defined as:

$$C_t(V_{tg}) = e\alpha(F' * n), \tag{3.1}$$

where V_{tg} is the top gate voltage. The electron temperature T_e dependence of C_t is sourced from the Fermi-Dirac distribution F' (Equation 2.39) and is the basis for the non-galvanic QD thermometer. To get a good detection of C_t, the QD device needs very strong coupling to the top gate.

Silicon-based QD devices have proven to be an excellent candidate in the progression of QD physics and quantum circuitry [70, 71, 72, 59, 73, 60, 74, 75, 76, 77]. The QD device used in our experiment is a silicon-on-insulator trigate accumulation-mode field-effect transistor (FET), shown in Fig 3.2a and b [72,
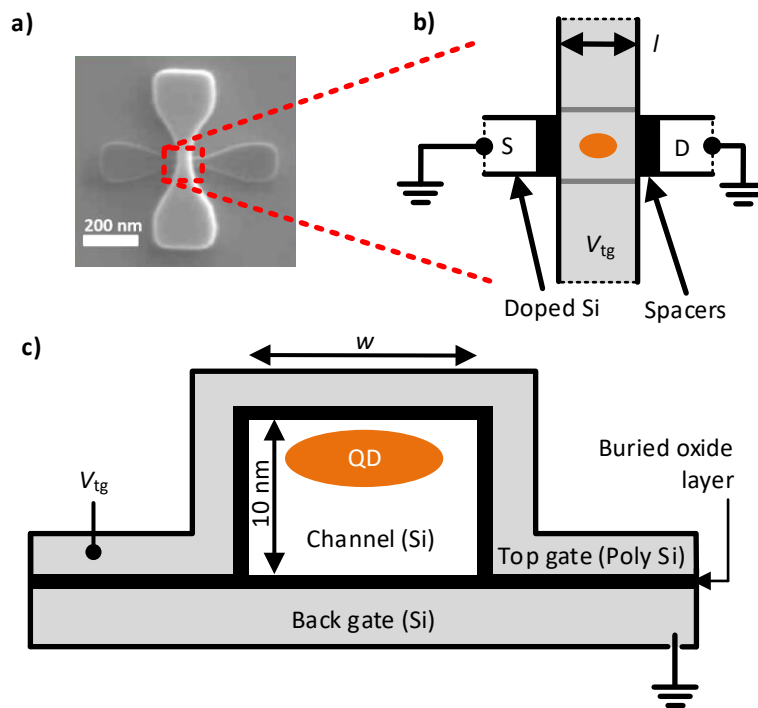
Figure 3.2: Details of FET geometry. The FETs were fabricated to a range of different dimensions. **a)** Top view SEM image of FET. The lower (dark grey bow-tie shape) Si is the source-drain channel and the upper (light grey bow-tie shape) Si is the top gate **b)**. Top view schematic of device, zoomed in on the interface between the channel and the top gate. The transistor consists of an undoped 1-D Si channel, 10 nm high, and a length in the order of $l \sim 10$ nm. A polycrystalline silicon top gate bridges over the channel, separated by a layer of Si oxide. The source (S) and drain (D) channel connection points are n-doped to allow electronic conduction at low temperatures. Two spacers are used to prevent doping of the Si channel under the top gate. **c)** Cross-section schematic of the device. The Si channel has a width in the order of $w \sim 10$ nm. A grounded Si back gate is beneath the channel, separated from the channel with a Si oxide layer.

60, 28, 78]. For this type of FET, the QD forms directly underneath the top gate, and so C_{tg} takes up a large fraction of the total dot capacitance C_Σ. This makes it ideal for non-galvanic measurements as the capacitive coupling between the QD energy levels and V_{tg} is significant, i.e the top gate lever arm α is relatively large, making the detection of C_t easier. A large number of these devices are fabricated on a single Si chip, with varying geometry. Each device consists of two major elements, the Si channel and the top gate. The channel is for source-drain transport, and has a length and width in the order of ~ 10 nm, with a height of 10 nm. The channel is made of Si, with n-doped source-drain connections to allow conduction. It is bridged by a polycrystalline silicon top gate. The top gate and channel are electronically insulated by a layer of SiO2 which is 145 nm thick. Two spacers flank either side of the top gate, over the channel. These spacers act like an umbrella during the doping of the Si channel, and therefore roughly define the un-doped area of the channel, including under the top gate.

When the FET is at cryogenic temperatures and a positive DC voltage V_{tg} is applied to the top gate, a localisation potential materialises in the Si chan-nel underneath the gate, which can produce conducting regions and allow transport between the source and drain. If the channel is wide, two QDs can sometimes appear in the corners where the top gate angles around the chan-nel. If the channel is narrow, a single QD can form in the centre of the channel, again under the top gate. The characteristics of the conducting islands that appear depend mostly on the channel geometry (described in Section 3.4). With this type of QD device, the top gate has two jobs, first to accumulate bound electron states and therefore create the QD, and secondly to act as a plunger gate to tune the QD. If V_{tg} is too low, there is no transport through the undoped silicon, whereas if V_{tg} is too high, the conducting region that appears in the channel will be large and will act as a simple conductor be-tween the source and the drain. In the intermediate values, if we adjust V_{tg} from low to high values, (ideally) the QD transitions from a small island with a large charging energy, passes through several conduction resonances, with the QD getting larger as V_{tg} increases, until the charging energy is too small to retain the Coulomb blockade. The dot can be tuned to any of these con-duction resonances by adjusting V_{tg} as desired.

3.2 Refrigerators

The thermometer was built for use in two cryostat systems; the IO 1 K pot fridge and the LD250 dilution refrigerator, both of which are described in Section 2.3. By testing the single-wire thermometer calibration and operation in two different system, we can verify the versatility of the technique. In this chapter, all of the initial testing and construction was completed in the IO fridge. The comparisons with the LD250 experimental setup are made where necessary and for future reference. In both systems, the fridge temperature is monitored by a ruthenium oxide resistance thermometer which was thermally anchored to the coldest stage of each fridge during data collection. The reading of the ruthenium oxide thermometer is denoted as T_f. Each fridge ultimately has the same RF circuitry and Si FET device installed, however the total attenuation for each system will be different, as discussed in Section 3.3.4. Each fridge also has an effect on the RF circuit resonance, as discussed in Section 3.3.2. For the measurements discussed in Chapter 4, the QD thermometer was mounted within both the IO the LD250 cryostat systems. The results from the IO and LD250 are discussed in Sections 4.2 and 4.3, respectively.

3.3 Radio-Frequency Circuit

The purpose of the RF reflectometry circuit is to detect the change in the tunnelling capacitance C_t (described in Section 3.1), and therefore measure the QD electron transitions with no galvanic measurements. The completed RF reflectometry circuit was built in both the IO and LD250, as shown in Figure 3.3. Completing the circuit involved solving many experimental problems at once, (described in the following subsections), but the author has attempted to describe the process in an appropriate order. Realising a low temperature electrical resonator is discussed in Section 3.3.1, and the impedance matching process is detailed in Section 3.3.2. Demodulating the reflected signal is discussed in Section 3.3.3 and optimising the completed reflectometry circuit is discussed in Section 3.3.4.

First, we consider how the reflectometry will work to read out C_t. The device is mounted on a carefully designed PCB (described in Section 3.3.1) which
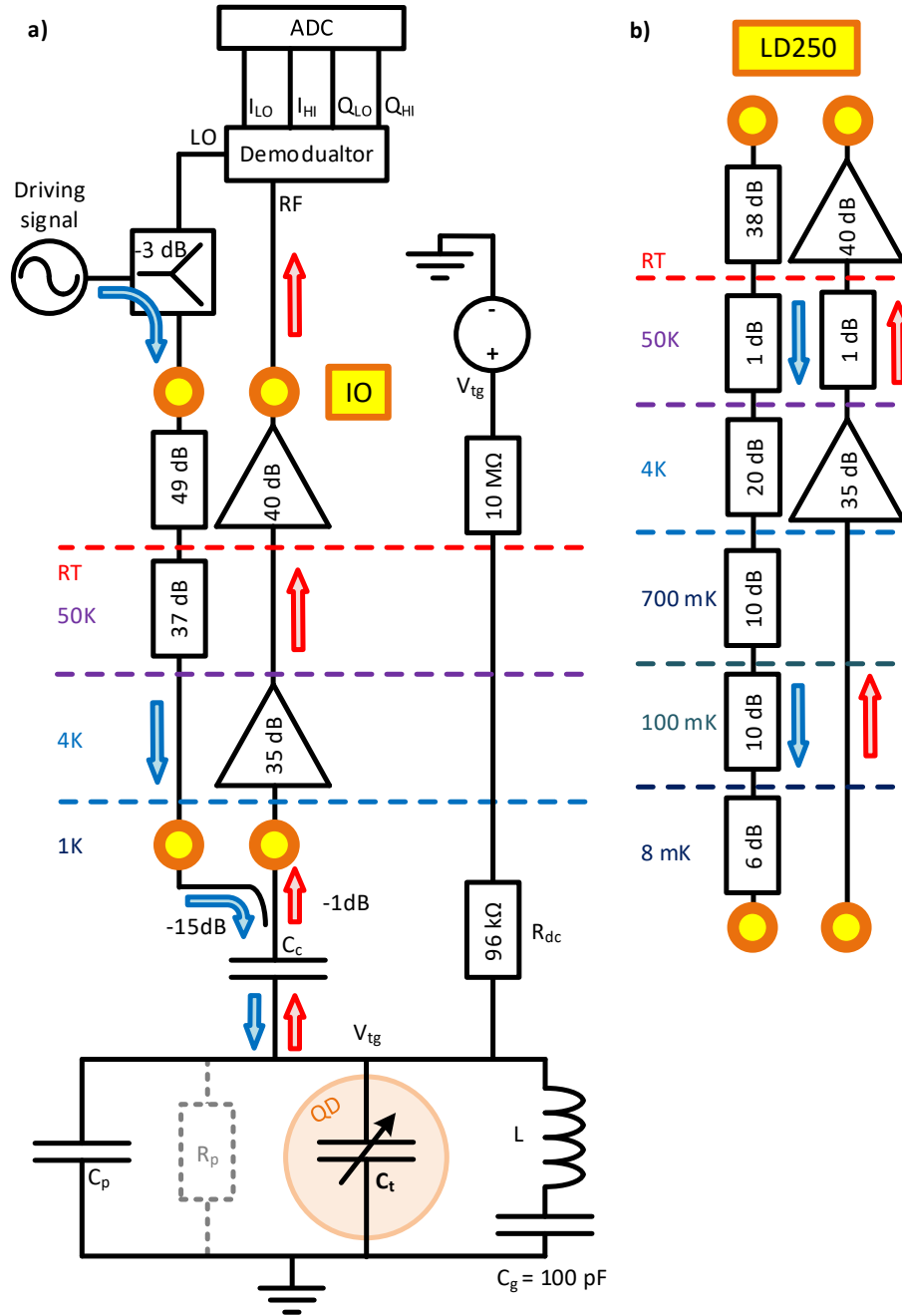
Figure 3.3: Schematic of the completed measurement circuit. **a)** The reflectometry circuit within the IO cryostat. The resonant circuit is comprised of the inductor L, the parasitic capacitance C_p, coupling capacitance C_c and the variable QD tunnelling capacitance C_t, which is the physical parameter monitored for thermometry. R_p is a modelled parasitic loss resistance to ground which impacts the resonant circuit Q-factor. The inductor line has a 100 pF capacitor to provide a DC break between the top gate and ground. The 96 kΩ resistor limits top gate RF signal loss to the DC line. V_{tg} is the controllable DC top gate voltage. The driving signal is a tone from the output of the RF generator. The demodulator is shown in more detail in Figure 3.9. LO and RF represent the local oscillator and return RF signal inputs of the demodulator. I_{LO}, I_{HI}, Q_{LO} and Q_{HI} are output signals from the demodulator, which are logged by an analogue to digital converter (ADC). **b)** The fridge lines corresponding to the LD250 cryostat. This replaces the IO fridge lines at the end points highlighted by yellow-orange circles, to complete the LD250 circuit.

also houses an electrical resonator, which in electrical engineering is commonly referred to as the tank circuit. The tank circuit is formed by a coupling capacitor C_c and an inductor L, chosen for good impedance matching (described in Section 3.3.2). To measure the electrical resonance a driving signal is sent to the tank circuit, and the reflected signal is detected using a homodyne detection scheme. This is achieved by demodulating the information bearing return signal with respect to the driving signal (described in Section 3.3.3). The demodulation of the reflected signal reads the RF reflection power $|S_{11}|$ and phase ϕ at the original driving frequency $f = \omega/2\pi$. A parasitic capacitance C_p and parasitic resistance R_p also affect the properties of the resonant circuit. To measure these parameters they are included as fitting parameters in a circuit model, that can be fit to the measured RF reflection $|S_{11}|$ and phase ϕ. The parasitic capacitance C_p includes the geometric gate capacitance C_{tg} for modelling purposes. The parasitic resistance R_p models the circuit loss to ground, which affects the resonance Q-factor [61]. The resonant circuit model has an impedance similar to Equation 2.65 but with the extra parasitic parameters added in:

$$Z_L = \frac{1}{i\omega C_c} + \frac{1}{i\omega(C_p + C_t) + \frac{i\omega C_g}{1 - \omega^2 L C_g} + \frac{1}{R_p}}, \tag{3.2}$$

where ω is the angular frequency of the driving signal and $C_g = 100\,\text{pF}$ is the grounding capacitor. The magnitude of the reflected power relative to the driving power, in decibels, is given by

$$|S_{11}|\,(\text{dB}) = 20\log\left(\text{Re}\left(\frac{Z_L - Z_0}{Z_L + Z_0}\right)\right) + R_c, \tag{3.3}$$

where R_c is the circuit background in dB and $Z_0 = 50\,\Omega$ is the characteristic impedance of the circuit. For clarity, $|S_{11}| = |R| + R_c$, where $|R|$ is the reflection coefficient from Equation 2.64. The phase of the reflected signal relative to the phase of the driving signal is given by

$$\phi\,(\text{rads}) = \text{Im}\left(\frac{Z_L - Z_0}{Z_L + Z_0}\right) + w\omega + \phi_c, \tag{3.4}$$

where $w\,(\text{rad\,Hz}^{-1})$ is the circuit phase winding and ϕ_c is the circuit phase

offset. The resonant frequency ultimately depends on total top gate capacitance and inductance via $\omega_0 = 1/\sqrt{L(C_c + C_p + C_t)}$. When driving the tank circuit at ω_0, $\phi \propto C_t$, when $C_t \ll C_p + C_c$ (as shown in Section 2.4.2). Combining that with Equation 3.1 gives a change in reflected signal phase that depends on electron temperature T_e according to:

$$\phi - \phi_0 = Ae^2\alpha^2 \left(F' * n \right), \qquad (3.5)$$

where A is the phase responsivity, which tells us the phase change due to a small change in capacitance, and ϕ_0 is the circuit phase offset at the resonant frequency when $C_t \approx 0$. From Equation 2.70, we can say that

$$A = 2Q_L / (C_p + C_c). \qquad (3.6)$$

If the constants A, α and Γ are known, measuring $\phi - \phi_0$ as a function of $V_{tg} - V_0$ and fitting the model described by Equation 3.5 gives a readout of electron temperature T_e.

3.3.1   Radio-Frequency Tank Circuit Design

The printed circuit board (PCB) is an important stage in assembling the RF reflectometry apparatus as it is the physical interface between the QD device chip and the electronics within the fridge. The device chip is directly glued to the PCB with conducting silver paint. The tank circuit is built onto the PCB, so the parasitic impedances intrinsic to the PCB will affect the circuit resonance. The surface mount components of the PCB include C_c, L, C_g and R_{dc} from Equation 3.2 and Figure 3.3. This makes the PCB a very influential element in regards to the behaviour of the reflectometry.

For the thermometry experiments in Chapter 4, the QD thermometer only requires a DC and RF bias tee connection to V_{tg}, but the PCB design includes also a back gate connection, and the two source-drain connections, as shown in Figure 3.4. These extra connections are included so that measurements can be taken to confirm that the thermometer is working as intended.

The chosen PCB material is 'Rogers 4003', a hydrocarbon ceramic laminate fabricated with a 'FR4' glass-reinforced epoxy material [79]. The ceramic
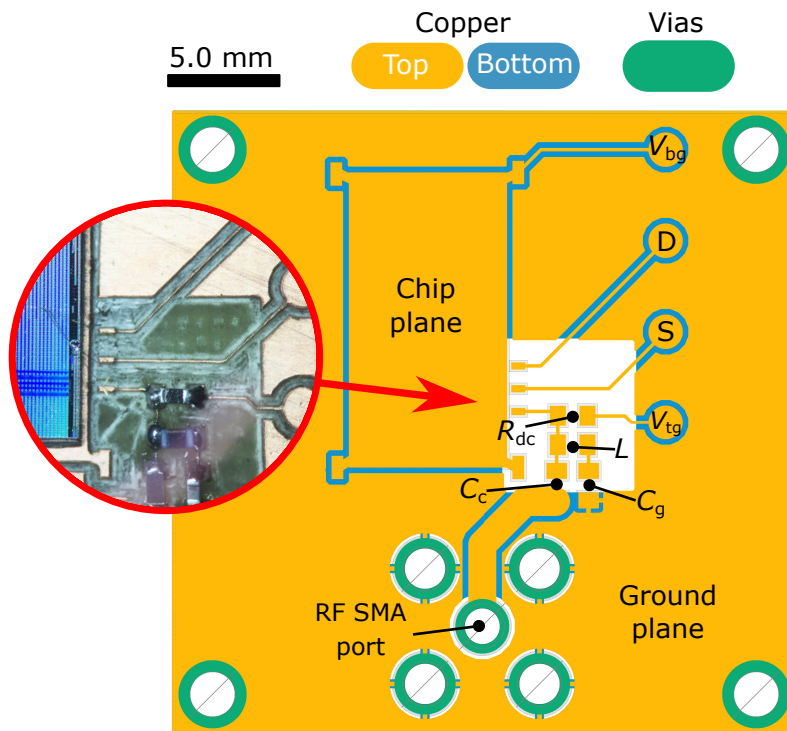
Figure 3.4: The design of the PCB used for mounting the FET chip into the cryostats. The insert shows a photo of the physical PCB, with the wire-bonded Si chip, and soldered surface mount components that make up the tank circuit used for the RF reflectometry measurements. The PCB design includes 0402 imperial code package spaces for the surface mount components; the top gate resistor R_{dc}, the inductor L, the coupling capacitor C_c and the grounding capacitor C_g. The inductor L package space can also be used to house a small spiral inductor chip, which is wire-bonded to the appropriate pads. V_{bg} shows the pogo-pin landing pad connection for the chip plane voltage, which is connected to the chip back gate via conducting silver paint. 'S' and 'D' represent the connections for the source and drain lines respectively. V_{tg} shows the DC connection for the top gate line, and the RF SMA port provides the top gate AC connection. The copper ground plane covers both the top and bottom surfaces, but the area around the top gate connection is removed from both sides to reduce the parasitic capacitance.

has a thermal expansion coefficient of $\sim 10^{-5}\,\mathrm{K}^{-1}$, which is very similar to copper, so it is good for use in a cryostat. The relative dielectric constant $\epsilon_\mathrm{r} = 3.38 \pm 0.05$ is low, which reduces the parasitic capacitance. This makes the material ideal for RF electronics with low loss at frequencies $f > 500\,\mathrm{MHz}$. The thickness of the layer of dielectric material within the PCB is $h = 0.813\,\mathrm{mm}$.

The purpose of the resonant tank circuit is to pick up a small change in tunnelling capacitance C_t, as shown in Section 2.4.2, so the PCB top gate parasitic capacitance C_p needs to be minimised to get the best possible signal via Equation 3.6. Several design choices are made to do this. First, the PCB metal directly connected to the top gate of the device is kept to a minimum footprint, with the tank circuit surface mount component package spaces organised in such a way to achieve this. Secondly, the ground plane is removed around the top gate metal, on both the top and bottom ground planes for the PCB.

The RF circuit is connected to the PCB via a 'SubMiniature version A' (SMA) connector. Because the circuit has a characteristic impedance of $Z_0 = 50\,\Omega$, the PCB coplanar waveguide track should match this impedance via Equation 2.71 to avoid reflection of the signal at the RF line-PCB interface. The waveguide therefore has a track width of $a = 1.27\,\mathrm{mm}$ and a total width (track width plus spacing on either side) of $b = 1.77\,\mathrm{mm}$. This gives the waveguide a characteristic impedance of $Z_0 = 51.3\,\Omega$, which matches well with the rest of the circuit. This creates an effective permittivity of $\epsilon_\mathrm{eff} = 2.369$ via Equation 2.74.

The reflectometry driving frequency will be somewhere between $500\,\mathrm{MHz}$ and $1\,\mathrm{GHz}$, which corresponds to a wavelength of $\lambda = 0.6\,\mathrm{m}$ and $0.3\,\mathrm{m}$ respectively. The PCB dimensions are $28\,\mathrm{mm} \times 28\,\mathrm{mm}$, which is much smaller than the wavelength, so wave interference on the board is not an issue.

Some of the surface mount component values could be chosen relatively easily. The device requires a DC bias V_tg to be applied to the top gate, so a $C_\mathrm{g} = 100\,\mathrm{pF}$ capacitor is placed in series with the inductor to avoid DC-shorting the device and to create a good RF ground at the frequency of operation. This value was chosen because it was large enough to create a relatively

low impedance so as not to affect the tank circuit, but also the self-resonance of the component was safely far away from the expected operating frequencies. Also, a $R_{dc} = 96\,k\Omega$ resistor is used on the top gate DC line to prevent a loss of RF signal power along this line.

3.3.2 Resonator Impedance Matching

The remaining PCB surface mount components i.e the coupling capacitor C_c and the inductor L, were more difficult to choose, since their optimum value depends on both characteristics of the PCB at low temperatures, and their own temperature dependence. A selection of surface mount components were soldered to the PCB, and cooled within the IO cryostat to test the completed tank circuit. Thin-film AVX Accu-P series multilayer ceramic capacitors were used with a temperature coefficient of $0 \pm 30\,ppm/C^\circ$. The range of inductors trialled for impedance matching were Coilcraft HP series (1005) ceramic-core chip inductors, also with a 0402 package size. These inductors have a temperature coefficient of $25 - 125\,ppm/C^\circ$. The values of L and C_c were selected to impedance match the resonant tank circuit. The procedure used here was to first estimate the PCB parasitic loss to ground at base temperature, including the resistance R_p and capacitance C_p. Then, using these values, the appropriate values for L and C_c can be calculated and tested.

Initially, C_p and R_p are unknown quantities, however a guess was made based on previous literature [74, 28, 61, 78] which suggested values in the order of $C_p \sim 0.1\,pF$ and $R_p \sim 100\,k\Omega$. Therefore, drawing out Z_L from Equation 3.2 on a $Z_0 = 50\,\Omega$ Smith chart shows that a logical choice for impedance matching of the tank circuit is in the order of $C_c \sim 0.1\,pF$ and $L \sim 100\,nH$. A few combinations of these components were trialled at room temperature to get a decent match, before being cooled in the IO as shown in Figure 3.5. The characteristics of the resonance change gradually and significantly from room temperature down to $\sim 1\,K$. This occurs as the surface mount components that make up the tank circuit shift in value, for example from changes in resistance and shrinking geometry. Fitting Equation 3.3 to the resonances with defined values for L, C_g and $C_t = 0$ reveals how load impedance Z_L is changing with temperature, shown in Figure 3.6. At lower
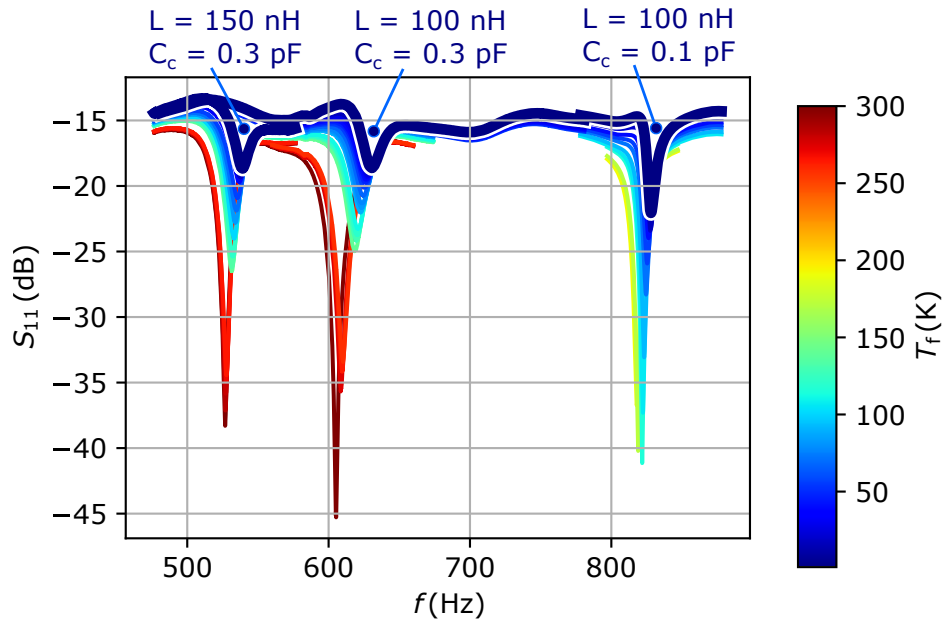
Figure 3.5: Three tests of the tank circuit resonance during a cool-down in the IO, measured with a network analyser. The y-axis shows the transmitted signal S_{11} from the LO port to the RF port of Figure 3.3, and the x-axis is drive frequency f, in the vicinity of the resonance. Each test has a (labelled) choice of inductor L and coupling capacitance C_c, which gives the resonance unique characteristics. Each resonance was tested from room temperature down to $\sim 1\,\mathrm{K}$, throughout which there is a gradual shift in the circuit characteristics.
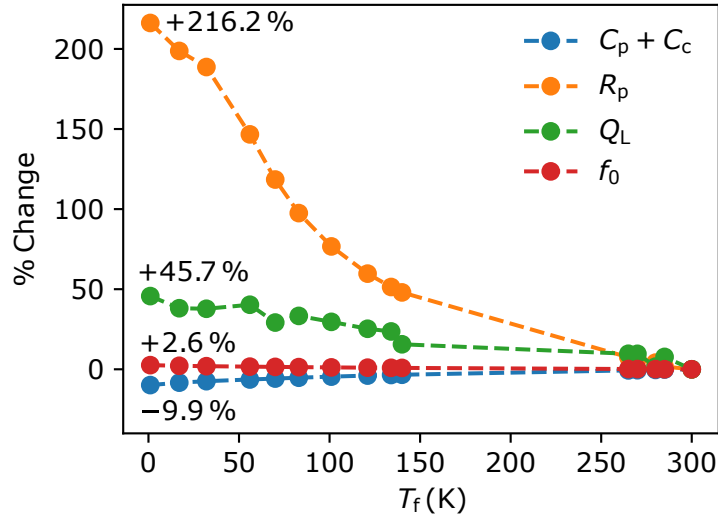
Figure 3.6: Estimated percentage change of tank circuit parameters with respect to their room temperature values, down to 1.3 K, the base temperature of the IO. The values are estimated from a model fit to the resonance as the fridge is cooled. R_p is the parasitic resistance, C_p and C_c are the parasitic and coupling capacitors respectively, from the circuit diagram in Figure 3.3. Q_L is the loaded Q-factor and f_0 is the resonant frequency.

temperatures, there is a negative shift in the total capacitance $C_p + C_c$, which causes a positive shift in the resonant frequency f_0. There is also a positive shift in parasitic resistance R_p at lower temperature, which causes an increase in the loaded Q-factor Q_L, despite the larger magnitude of minimum reflection $|R_{min}|$. From these tests, the parasitic parameters of the board with surface mount components are $C_p \approx 0.28 \, \text{pF}$ and $R_p \approx 74.5 \, \text{k}\Omega$.

These values were then used in the final stage of impedance matching, where a simulation was performed to test every variation of L and C_c to find the optimum choice for the selection components available, shown in Figure 3.7. The figure of merit for each simulation was the minimum reflection $|R_{min}|$, which highlights where the board is well matched. A condition of $500 \, \text{MHz} < f_0 < 1000 \, \text{MHz}$ was set as this allows a high enough frequency for fast reflectometry readout but still works with the other RF components in the circuit, including the demodulator discussed in Section 3.3.3. This simulation suggested the theoretical best choice for the components was $C_c = 0.2 \, \text{pF}$ and $L = 100 \, \text{nH}$, and so these components were chosen to complete the tank circuit. A simultaneous fit of Equations 3.3 and 3.4 to the $|R|$ and phase
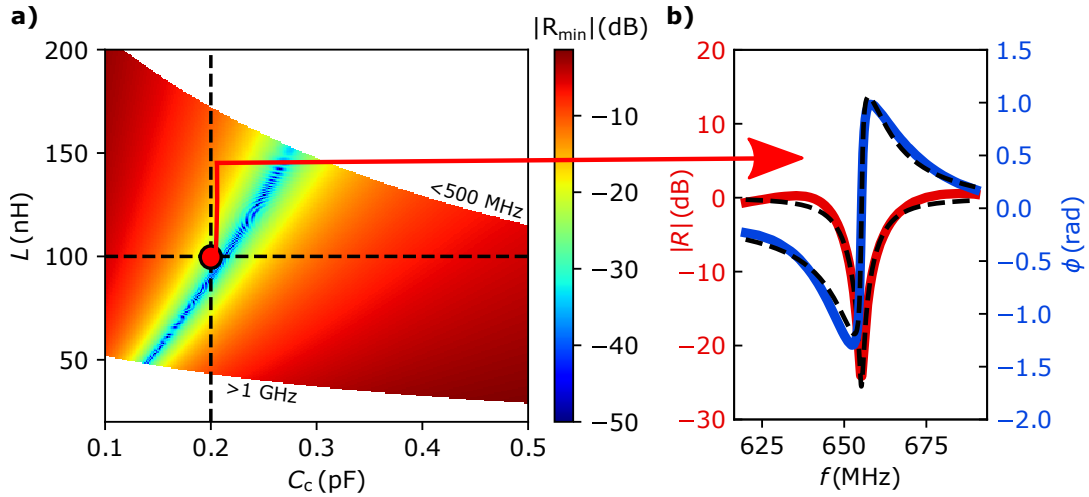
Figure 3.7: Impedance matching with the aid of simulation. **a)** a simulation of minimum reflection $|R_{min}|$ against inductor and coupling capacitor, L and C_c respectively, from the circuit in Figure 3.3. The dashed lines represent the chosen component values, which was partially based on what compatible options were available. The simulation assumes a parasitic capacitance $C_p \approx 0.28\,\text{pF}$ and resistance $R_p \approx 74.5\,\text{k}\Omega$ obtained from earlier tests in Figure 3.5. The white areas show where the resonant frequency goes above the 1 GHz boundary and below 100 MHz boundary. The red dot shows the values of the components selected to impedance match the tank circuit, considering the limited range of values manufactured to work at low temperatures (which is why it is not dead centre in the $|R_{min}|$ valley). **b)** The resonance of the tank circuit with the selected components, measured with a network analyser. The tank circuit is mounted within the IO at base temperature. The black dashed line shows a model fit with a loaded Q-factor of $Q_L = 35.2$ and resonant frequency $f_0 = 655.2\,\text{MHz}$. $|R|$ and ϕ are respectively the reflection and phase of the signal, from the tank circuit.

Figure 3.8: Comparison of completed RF circuit resonance curves within the IO and LD250 cryostats, including Al-bonded spiral inductor and FET. For both plots, the reflected signal magnitude $|R|$ and phase ϕ is shown in red and blue, respectively. The data was taken with a network analys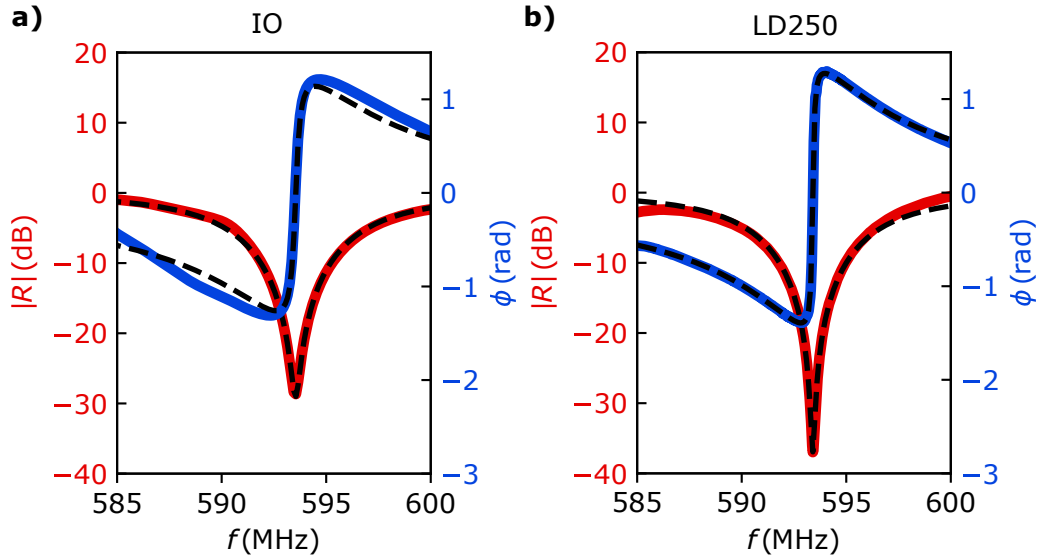er. The x axis shows the RF drive frequency f. The black dashed lines show the fitting of $|R|$ and ϕ with Equations 3.3 and 3.4 respectively, using the load impedance model described by Equation 3.2. The fit estimates the parasitic capacitance C_p and resistance R_p. **a)** The circuit resonance in the IO. The resonance has a Q-factor of $Q_L = 59.3$ and a resonant frequency of $f_0 = 593.6\,\text{MHz}$. The fit estimates a parasitic capacitance of $C_p = 0.57\,\text{pF}$ and a parasitic resistance of $R_p = 40.3\,\text{k}\Omega$. **b)** The circuit resonance in the LD250. The resonance has a Q-factor of $Q_L = 63$ at a resonant frequency of $f_0 = 593.4\,\text{MHz}$. The fit estimates a parasitic capacitance of $C_p = 0.57\,\text{pF}$ and a parasitic resistance of $R_p = 43.2\,\text{k}\Omega$.

ϕ of the tanks circuit resonance estimates the parasitic parameters. This estimated a parasitic capacitance of $C_p = 0.39\,\text{pF}$ and resistance $R_p = 121.8\,\text{k}\Omega$. The circuit has a loaded Q-factor of 35.2 and a resonant frequency of $f_0 = 655.2\,\text{MHz}$.

To finalise the circuit, the surface mount inductor was switched for a superconducting NbTiN-on-quartz spiral, which is expected to have much lower signal loss, and therefore should increase the unloaded Q-factor and boost phase responsivity. The inductor has 11 turns with $6\,\mu\text{m}$ spacing, which gives it inductance $L = 96\,\text{nH}$ (via the Wheeler formula [80]), similar to the $100\,\text{nH}$ surface mount inductor used previously. At this point, the QD chip was mounted and connected via $17\,\mu\text{m}$ diameter aluminium bond wires. The

tank circuit was built to be extremely sensitive to capacitance, so these additions affect the behaviour of the resonator, as shown with the new resonance in Figure 3.8a. A fit of Equations 3.3 and 3.4 to the new resonance estimates that the parasitic capacitance increases significantly to $C_p = 0.57\,\text{pF}$, presumably from the extra metal that connects the QD top gate. The parasitic resistance increases to $R_p = 40.3\,\text{k}\Omega$. The Q-factor increased to 41.7 and the resonant frequency drops to $f_0 = 593.6\,\text{MHz}$. The increased R_p and loaded Q-factor is a result of the lower losses in the high-Q spiral inductor. The coupling capacitor is assumed to have reduced in capacitance by 10 % from the cooling, to $C_c = 0.18\,\text{pF}$.

The choice of cryostat has a small, but noticeable, effect on the external circuit properties. When mounted in the cooled LD250 dilution refrigerator, the circuit model estimated a parasitic capacitance of $C_p = 0.57\,\text{pF}$ and a parasitic resistance of $R_p = 43.2\,\text{k}\Omega$. Comparing to the IO circuit, the resonance frequency was very similar at $f_0 = 593.4\,\text{MHz}$ with an increase in Q-factor to 63.

3.3.3   Demodulation of Reflected Signal

The reflectometry circuit is operated at the resonant frequency f_0, which acts as the carrier frequency. Any modulation that occurs at this frequency needs to be measured. When the reflected signal returns via the amplified return line, it is demodulated at f_0 into the reflected signal power S_{11} and the difference in phase ϕ (relative to the ingoing signal). To do this, the driving signal and return signal are connected to an active ADL5387 quadrature demodulator chip, shown in Figure 3.9. The chip was mounted within grounded metal housing along with several RF circuit components and the $+5\,\text{V}$ power lines. The housing had high-frequency SMA ports for the LO and RF inputs, and Bayonet Neill–Concelman (BNC) ports for the demodulated outputs. The LO input is connected to a $\times 2$ frequency multiplier (MC model No. MK-5) followed by a high pass filter (MC model No. SHP-900+). The high pass filter has a cut off at $f = 910\,\text{MHz}$, which prevents the local oscillator driving frequency f interfering with the chip, whilst allowing the $2f$ signal through. The ADL5387 requires double the local oscillator frequency on the LOIP pin (refer to Figure 3.9), with a signal power of $0 \pm 6\,\text{dBm}$ for the demodulation
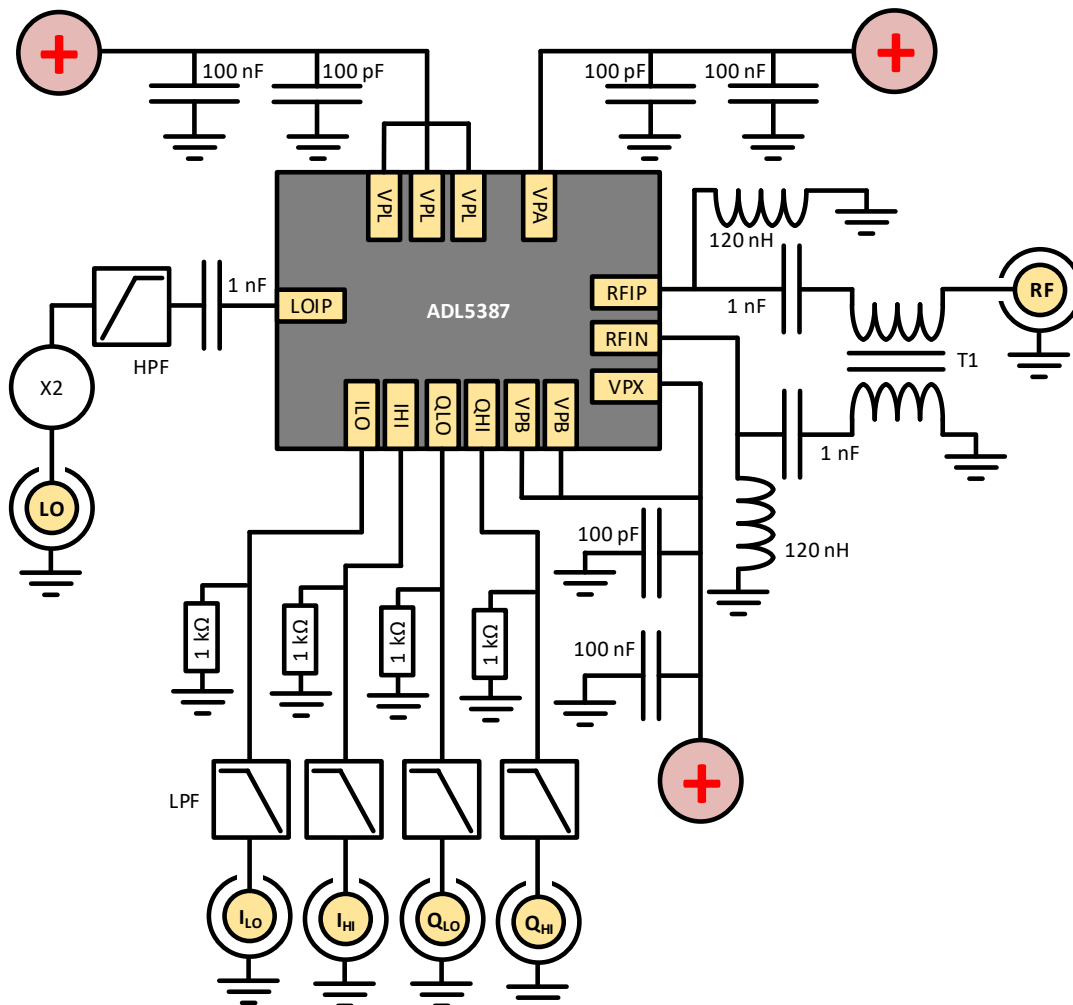
Figure 3.9: The custom demodulator setup, using a quadrature ADL5387 chip. RFIN and RFIP pins are for RF input. A single-ended signal is applied to the RF input pins through a *T1* 1:1 balun. Ground-referenced inductors are also connected to the RF input pins for noise reduction. LOIP is the local oscillator pin, which requires double the driving frequency $2 \times f$. This is achieved with a $\times 2$ frequency multiplier on the LO input, which has 13 dB of attenuation. A 910 MHz high pass filter (HPF) allows $2 \times f$ through to the LOIP pin. Both the LO and RF input pins have AC coupling capacitors at 1 nF. ILO, IHI, QLO and QHI pins are the I-channel and Q-channel mixer baseband outputs. Each of these lines has a ground-referenced resistor and 48 MHz low pass filter (LPF) for noise reduction. VPA, VPL, VPB, VPX are power supply pins for for LO, RF, biasing and baseband sections, respectively. The $+5$ V input to each of these pins is filtered with 100 pF and 100 nF capacitors.

to work. The RF input line is connected to a balun which creates a balanced signal pair for the RF input (returning from the reflectometry circuit) via the RFIP and RFIN pins. Both the LO and RF lines have AC coupling capacitors at $1\,\mathrm{nF}$. The demodulated output signal is carried on four lines, I_{LO}, I_{HI}, Q_{LO} and Q_{HI}. The values of $I = I_{\mathrm{HI}} - I_{\mathrm{LO}}$ and $Q = Q_{\mathrm{HI}} - Q_{\mathrm{LO}}$ represent the Cartesian coordinates of the demodulated signal. Each output for I and Q has a $50\,\Omega$ differential output impedance ($25\,\Omega$ per pin). The bias level on the four I-Q pins are $-2.8\,\mathrm{V}$. Each output line is filtered with low pass filters with a $48\,\mathrm{MHz}$ cutoff (MC model No. SLP-50+), which reduce noise in the demodulated signal. External to the metal housing, the four voltage readings I_{LO}, I_{HI}, Q_{LO} and Q_{HI} were each connected to the inputs of a USB-6356 NI DAQ, which converts the four analogue voltages into digital data at a maximum sample rate of $2.6 \times 10^5\,\mathrm{s}^{-1}$. The reflection from the circuit S_{11} can be calculated from these readings via:

$$S_{11} = \sqrt{(I_{\mathrm{HI}} - I_{\mathrm{LO}} + I_0)^2 + (Q_{\mathrm{HI}} - Q_{\mathrm{LO}} + Q_0)^2}, \qquad (3.7)$$

where $Q_0 = 6.0 \times 10^{-4}\,\mathrm{V}$ and $I_0 = 0.13\,\mathrm{V}$ are output voltage offsets. The phase ϕ can be read via

$$\phi = \arctan\left(\frac{Q_{\mathrm{HI}} - Q_{\mathrm{LO}} + Q_0}{I_{\mathrm{HI}} - I_{\mathrm{LO}} + I_0}\right). \qquad (3.8)$$

Power was supplied to the active demodulator chip at $+5\,\mathrm{V}$ ($> 180\,\mathrm{mA}$) connected in parallel to each appropriate pin with $100\,\mathrm{pF}$ and $100\,\mathrm{nF}$ capacitors to filter out noise and provide steady power.

3.3.4   Reflectometry Optimisation

Optimising the power and frequency of the driving and reflected signals is important to increase measurement responsiveness whilst minimising disturbance to the QD-reservoir system. Once the QD is tuned and a Coulomb resonance has been located, the reflectometry circuit can be optimised to get the best possible responsivity to the QD total capacitance.

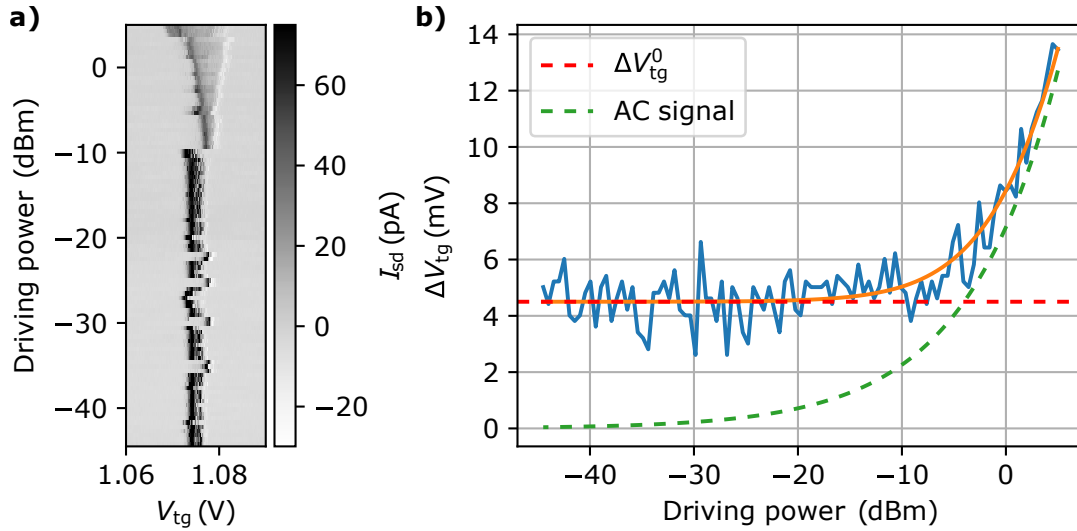The completed reflectometry circuit has several signal power requirements

Figure 3.10: Calibration of RF power on the FET. The DC top gate voltage V_{tg} is swept over a single Coulomb peak while the AC RF driving power is adjusted. The measurements are taken from within the IO at base temperature. **a)** The single conduction Coulomb peak observed by monitoring the source-drain current I_{sd} with a small source-drain bias voltage $V_{sd} = 1.05\,\text{mV}$. The source-drain voltage is small enough that the AC signal can create a small negative current on the edge of the Coulomb peak. When the driving power is reduced, the width of the peak, ΔV_{tg}, narrows. The peak shifts around the V_{tg} axis due to the charge noise induced by the relatively high AC power on the top gate. **b)** The measured width of the Coulomb peak ΔV_{tg} against the driving power, from the same data. The width converges at around $-20\,\text{dBm}$. The orange line is a fit of the Pythagorean addition of two broadening effects, the background broadening and the AC power broadening. The red dashed line represents the converged value for the background width ΔV_{tg}^0, which is related to the bias V_{sd} and other broadening effects. The green dashed line represents the AC peak-to-peak voltage V_{pp} from the driving power, which from the fit estimates the attenuation from the ingoing fridge lines to be $-39\,\text{dB}$, which agrees with the circuit design.

for successful operation. The driving signal needs to be attenuated as it travels to the cooled environment within the fridge. This helps prevent any unwanted warming of the device, and in this case it is essential to the experiment. The attenuation is spread across the multiple stages of the cryostat, so as to attenuate any unwanted thermal noise that may get in from black body radiation. A RF signal at the tank circuit resonant frequency will oscillate the QD energy level by $\Delta E_{\mathrm{RF}} = |e\alpha V_{\mathrm{pp}}|$, where V_{pp} is the peak-to-peak AC voltage at the QD top gate. The nature of the experiment requires the observation of several broadening mechanisms, including thermal and tunnel broadening, which cannot be observed if the RF signal power is too high. Therefore we need to meet the condition:

$$\Delta E_{\mathrm{RF}} \ll k_{\mathrm{B}}T, \hbar\Gamma. \tag{3.9}$$

A very convenient method of ensuring this condition is met is to reduce the driving power whilst monitoring the width of a single QD Coulomb resonance. This is done by measuring the source-drain current I_{sd} with a small source-drain bias voltage $V_{\mathrm{sd}} = 1.05\,\mathrm{mV}$ (which is around 1/30 the QD charging energy) as demonstrated within the IO in Figure 3.10. When performing this experiment, the fridge was held at base temperature $T_{\mathrm{f}} = 1.268 \pm 0.001\,\mathrm{K}$. The driving signal is directly connected into the fridge lines, i.e. there is no room temperature attenuation. During the experiment, the relatively high power caused extra charge noise and switching events, but the width of the peak is mostly unaffected, as it was measured comparatively quickly. As the power is lowered, the width of the peak in top gate voltage, ΔV_{tg}, narrows and then settles at the width defined by V_{sd} and the QDs intrinsic broadening mechanisms. For the IO circuit shown in Figure 3.3, a driving power of $< -20\,\mathrm{dBm}$ is low enough to have no effect on the Coulomb peak width. Considering the ingoing fridge attenuation of $52\,\mathrm{dB}$, this equates to a device signal power of $< -72\,\mathrm{dBm}$. The driving frequency needs to be operating at $19\,\mathrm{dBm}$ to get the appropriate power in the demodulator chip LO input, so a $49\,\mathrm{dB}$ attenuator is placed on the ingoing RF line, which makes the device signal power $-82\,\mathrm{dBm}$. Reducing the power further would deteriorate the signal. The LD250 has an ingoing fridge attenuation of $71\,\mathrm{dB}$, so a room temperature $38\,\mathrm{dB}$ attenuator was added to the ingoing
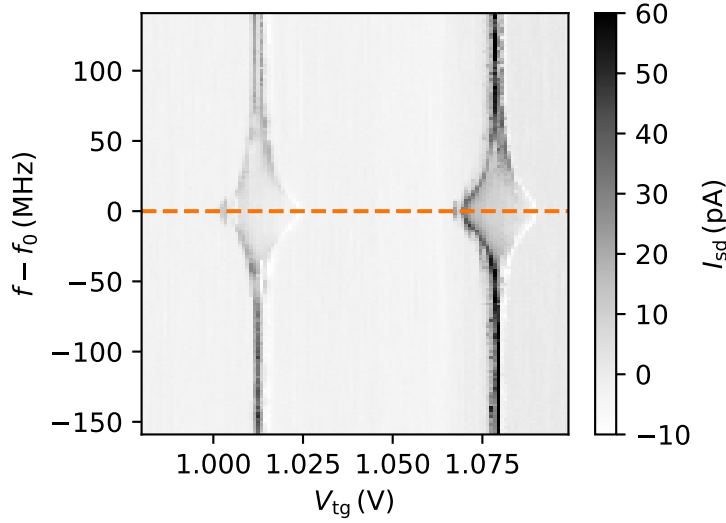
Figure 3.11: Coulomb peak detection of tank circuit resonance, in the IO cryostat at base temperature. The top gate voltage V_{tg} is swept over two Coulomb peaks as the driving RF frequency f is adjusted, while the source-drain current I_{sd} is monitored. There is a small source-drain bias voltage $V_{sd} \approx 0.3\,mV$. The source-drain voltage is small enough that the AC signal can create a small negative current on the edge of the Coulomb peak. The RF power at the device was $-41\,dBm$. The width of the Coulomb peaks hits a maximum when the driving frequency matches the resonant frequency of the tank circuit. This allows the observation of the resonance to be made via the device instead of from the reflected signal. The orange line shows the resonance at $f_0 = 595.5\,MHz$, which is slightly higher than the network analyser $|S_{11}|$ measured resonance $f_0 = 593.6\,MHz$ (observed in Figure 3.8). The equivalent experiment from the LD250 circuit gives a device-measured resonance of $f_0 = 593.5\,MHz$.

line, which creates a similar device power of $-90\,dBm$.

A convenient technique to optimise the driving frequency is to observe the resonant frequency f_0 from the response of the QD. This was done by setting the driving frequency power to an appropriately high level, so that when the tank circuit is in resonance $\Delta E_{RF} > k_B T, \hbar\Gamma$. The width of the QD Coulomb peaks in top gate voltage ΔV_{tg} was observed (again by measuring the source-drain current I_{sd} with a small source-drain bias voltage $V_{sd} \approx 0.3\,mV$) as the driving frequency f is varied, demonstrated within the IO (at base temperature) in Figure 3.11. When $f = f_0$, the transmission of power into the QD top gate is maximised, which also maximises the width of the Coulomb peak,

revealing the optimum driving frequency to maximise phase responsivity.

The returning RF signal (from the cooled device to the RF demodulator pins) needs to have a high enough power for the demodulator to function properly (between $-40\,\mathrm{dBm}$ and $+10\,\mathrm{dBm}$), so two amplifiers are included in the return line. At the $4\,\mathrm{K}$ fridge stage, a cryogenic SiGe low noise amplifier (CMT model No. CITLF3) is added to the return line which contributes $35\,\mathrm{dB}$ of amplification. This cryogenic amplifier has a low noise temperature ($4.5 \pm 1\,\mathrm{K}$ at a temperature of $4\,\mathrm{K}$) and therefore it boosts our signal whilst contributing less noise than a room-temperature amplifier. An extra room temperature $40\,\mathrm{dB}$ amplifier is added on the return line. Combined with the cryo-amp, this produces a $75\,\mathrm{dB}$ total gain from the device, which brings the power level back to $\sim -10\,\mathrm{dBm}$ at room temperature, ideal for the demodulator chip.

3.4   Quantum Dot Geometry

The final stage of building the thermometer was to choose an appropriate Si FET device geometry from the device chip (detailed in Section 3.1) to create a suitable QD system. The FET chip was mounted on the PCB (detailed in Section 3.3.1). These devices were trialled in the IO cryostat.

The first FET that was measured had a Si channel with a width of $30\,\mathrm{nm}$ and a length of $200\,\mathrm{nm}$ (which also corresponds to a top gate width of $200\,\mathrm{nm}$). A stability diagram was taken (at IO base temperature) with both I_{sd} and ϕ measured simultaneously, shown in Figure 3.12a. This device required a large top gate voltage $V_{\mathrm{tg}} \sim 1\,\mathrm{V}$ to get source-drain transport to appear, and so some regions were fairly unstable with charge noise and switching events. Coulomb diamonds were observed with a charging energy of $E_{\mathrm{c}} = 56.9\,\mathrm{meV}$ and top gate lever arm $\alpha = 0.86$. However there is also a second set of smaller diamonds within the first set, with a charging energy of $E_{\mathrm{c}} \approx 5.5\,\mathrm{meV}$ and top gate lever arm $\alpha \approx 0.9$. The second set of diamonds are even clearer in the reflected phase measurement, where a distinct phase response is picked up from each 'drain resonance' side of the diamonds. Periodic lines like this suggest the charging of a second floating object [81]. It is likely two QDs
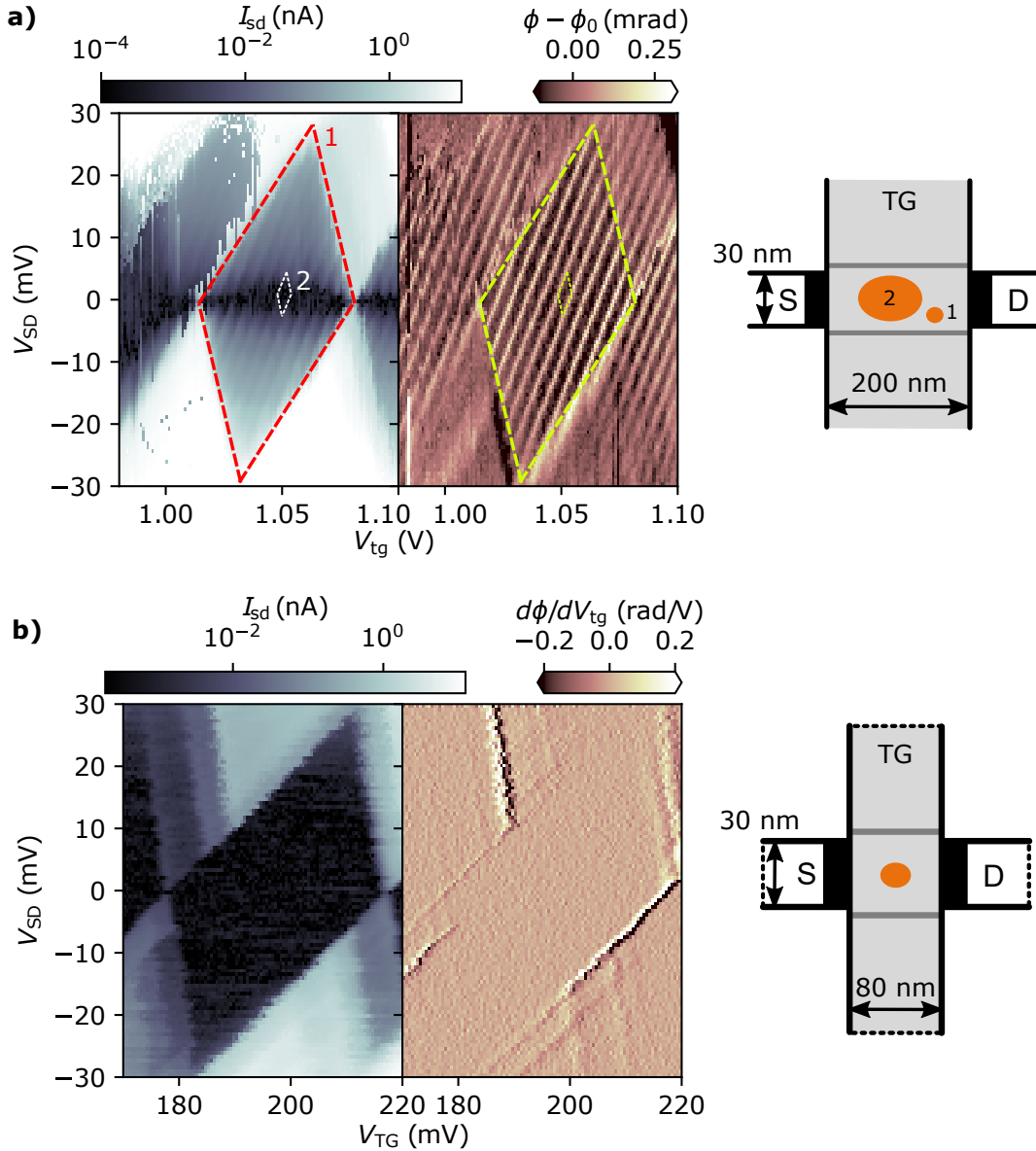
Figure 3.12: Charge stability diagrams measured by reflectometry technique and DC transport in IO cryostat. For both diagrams the fridge was held at temperature $T_f = 1.268 \pm 0.001\,\text{K}$. **a)** The stability diagram shows the QD source-drain current $|I_{sd}|$ in log scale on the left, and the simultaneous reflected signal phase is shown on the right. Two sets of Coulomb diamond can be observed, labelled '1' and '2'. On the right there is a schematic of the FET (not to scale) that details the device geometry and illustrates how two QDs might appear in the device, labelled '1' and '2' to match the respective Coulomb diamonds. **b)** The stability diagram shows the QD source-drain current $|I_{sd}|$ in log scale on the left, and the simultaneous derivative of reflected signal phase in relation to the top gate voltage $d\phi/dV_{tg}$ is plotted on the right. On the right there is a schematic of the FET (not to scale) that details the device geometry, in this case only one QD appears.

have formed, with both a large and small QD forming under the top gate in response to large V_{tg}.

The second FET trialled had a top gate 80 nm wide, and a Si channel 30 nm wide. The idea was to reduce the width of the top gate (or the length of the undoped Si channel under the top gate), which should reduce the V_{tg} needed to get source-drain transport. A stability diagram was taken (at IO base temperature) with both I_{sd} and ϕ measured simultaneously, shown in Figure 3.12b. In this case to get source-drain transport the top gate was only $V_{\text{tg}} \sim 0.1$ V. A single set of stable Coulomb diamonds was observed, and the QD existed over several Coulomb peaks in the V_{tg} axis.

To choose a Coulomb peak to use for thermometry, the source-drain connections on this device were grounded (so $V_{\text{sd}} = 0$) and the top gate was scanned, revealing the Coulomb peaks which are picked up by the phase reflectometry, shown in Figure 3.13. The peaks were chosen for the thermometry location based on demonstrating a clear phase responsivity and low charge noise. The position of the Coulomb peak along the V_{tg} axis must be stable enough so that the magnitude of variance is much lower that the FWHM. This prevents charge noise interfering with the shape of the peak. A narrow peak suggests a reduced tunnel broadening (as they are all at the same temperature), which is desirable for thermometry.
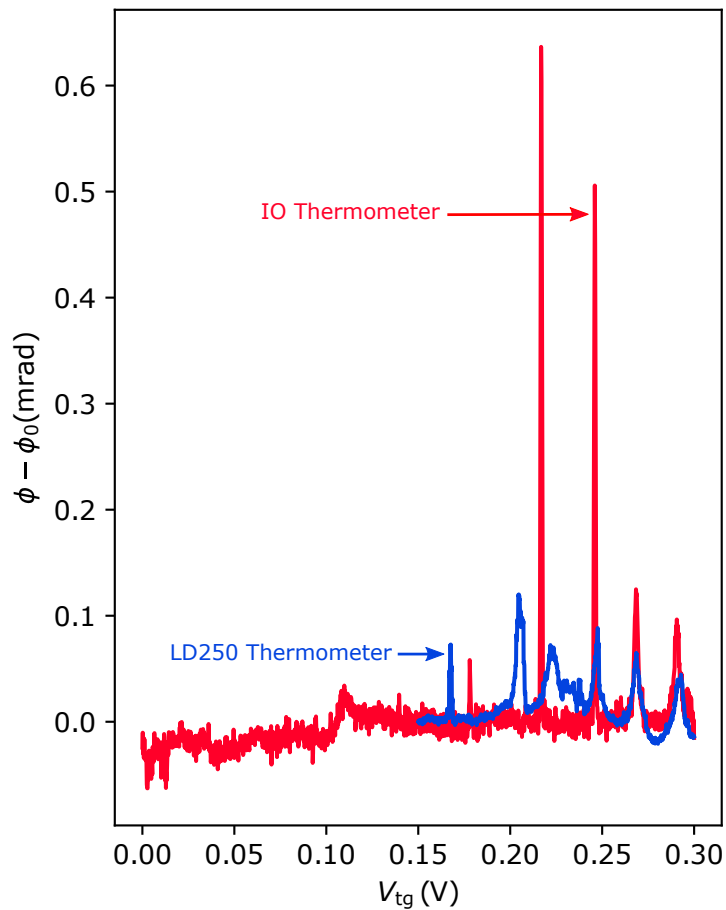
Figure 3.13: Coulomb peaks observed from phase reflectometry by sweeping top gate voltage V_{tg}. The red data shows measurements taken from within the IO at base temperature, and the blue data shows the LD250 data from the same FET. The QD source and drain connections are grounded during the measurements. The peaks show the QD electron transitions, where thermometry can be performed. The arrows show the peaks used for thermometry in Chapter 4.

Chapter 4

Operating a Single-Wire Quantum Dot Thermometer

This chapter details the results from the calibration and operation of the QD electron thermometer described in Chapter 3. Both the calibration and operation of the thermometer are performed with a single capacitive measurement of the QD. This chapter includes a description of the experiment in Section 4.1, the results from the IO and LD250 fridges in Sections 4.2 and 4.3, respectively, the description of a physical model of the thermometer in Section 4.4, thermometry error analysis in Section 4.5 and a close look at the QD energy scales in Section 4.6. The implications of the results are discussed in Section 4.7. Some of these results are accepted for publication in Physical Review Applied.

4.1   Calibration and Operation

Here, the process of thermometer calibration and operation with a single-wire is described in detail. These techniques are used in the experiments described in Sections 4.2 and Sections 4.3 for the IO and LD250 cryostats, respectively.

The experimental data discussed in this chapter come from two separate cool-downs of the FET device, in two different cryostats; the IO 1 K pot cryostat and the LD250 dilution refrigerator (details on these systems are in Section 2.3). The RF reflectometry measurement circuits were mounted in both cryostats, described in Chapter 3, and shown in Figure 3.3. The Si FET device

used is detailed in section 3.4. Each cool-down has two stages to the experiment, the calibration of the QD thermometer which also estimates a physical model of the system, and then the subsequent operation to measure electron temperature. Additionally, because these are first-time demonstrations, this is also a 'confirmation' stage in Section 4.4 where source-drain connection are used to confirm the validity of the physical model.

The calibration of the QD thermometer has two purposes. First of all, to make sure the electron temperature readout from the thermometer is accurate, but secondly, to fill in unknown physical parameters within the model that makes up Equation 3.5. The FET is tuned to a QD Coulomb peak with a positive V_{tg}, shown in Figure 3.13. With the driving frequency f set to the tank circuit bare resonance frequency f_0, the phase of the demodulated signal ϕ is monitored as the DC QD top gate voltage V_{tg} is swept across the chosen QD Coulomb peak, located at top gate voltage V_0 (this measurement will be referred to as a phase trace). The calibration process involves a single Chi-square fit (described in Section 2.2.1) of Equation 3.5 over several phase traces taken at a variety of fridge temperatures. These temperatures need to be across a large enough range so that the phase traces are distinct enough to determine electron temperature dependence. The calibration temperatures also need to be high enough that it can be assumed the electrons are thermalised with the cryostat. The measurements are designed to require no use of the source-drain QD connections, so the usual method of characterising the QD via a stability diagram is not possible. This means there are three parameters unaccounted for within Equation 3.5; the top gate lever arm α, the tunnel rate Γ, and the phase responsivity A. The calibration fit shapes the model over all the phase traces by adjusting α, Γ and A, which have no dependence on temperature and are distinct enough to avoid crossover in the fitting between the estimation of each parameter. All three of these parameters remain constant over a single QD conduction resonance. The phase responsivity A can be calculated via Equation 3.6, but the introduction of the demodulator chip (discussed in Section 3.3.3), and the large attenuation of signals entering the fridge, alters the loaded Q-factor from what is observed with the network analyser in Figure 3.8. Allowing A to be a fitting parameter reduces the chance of calibration error and also increases the versatility

of the calibration process. For example, different circuits would have variations in parasitic capacitance or loaded Q-factor, and the calibration fit would include the influence of these factors within A, and no extra measurements would be needed. Each phase trace has an individual fit for ϕ_0 and V_0. These values can change if there is a long pause between data sweeps, if there is significant charge noise, or a different ambient lab temperature effecting the room temperature electronics. Extracting ϕ_0 and V_0 from each phase trace is trivial, so it has no effect on the fitting of α, Γ and A. The difference in temperature between the phase traces within the calibration data is crucial to capturing the physical picture of the QD. Once α, Γ, and A are defined from the calibration fit, then the QD thermometer is ready for operation.

Operating the calibrated thermometer is a more straightforward process. At a stable fridge temperature, a phase trace is measured. The electron temperature T_e is then estimated by fitting Equation 3.5 to the sweep, equipped with the values α, Γ and A previously determined from the calibration. A single electron thermometry fit has three fitting parameters, T_e, ϕ_0 and V_0. Like with the calibration, these last two parameters are trivial to estimate.

Another electron thermometry technique is to measure the phase at the centre of the Coulomb peak, when the DC top gate voltage is set to $V_{tg} = V_0$. With this condition, the tunnelling capacitance C_t is at its maximum value, so the phase response peaks such that $\phi - \phi_0 = \phi_{MAX}$. The calibrated Equation 3.5 predicts a relationship between ϕ_{MAX} and T_e, allowing a conversion between the two. This method allows fast readout because only one phase value needs to be measured and converted, instead of an entire phase trace being measured and fitted to. The precision of this measurement is entirely dependent on the averaging time that goes into each ϕ_{MAX} data point. The electron temperature readout can be affected by charge noise in the Coulomb peak. The technique can stop working if there is a significant charge jump in the Si FET, causing the location of the Coulomb peak to shift, which would mean relocating V_0 to continue the thermometry. This is rare with a stable fridge temperature, and the likelihood decreases with time spent in the cryostat. If the fridge temperature is changed then it is likely the peak position has moved, and hence V_0 should be relocated.

4.2   IO Cryostat Results

This section details the results of the QD thermometer calibration and electron thermometry from within the IO 1 K pot cryostat, at fridge temperatures $1.3 < T_f < 3.0$ K. The FET used is discussed in Section 3.4 and the tank circuit is discussed in Section 3.3.1. The complete circuit can be seen in Figure 3.3. The driving frequency was set to the resonant frequency of the IO circuit $f_0 = 598.0$ MHz (from Figure 3.11).

To collect the calibration data, the fridge temperature was stabilised at a particular value using a PID controlled heater mounted on the 1 K plate, and a set of 10 reflected signal phase traces were taken by sweeping V_{tg} across the QD Coulomb peak. This was done at three particular fridge temperatures $T_f = 2.0, 2.5, 3.0$ K. The temperatures are purposely high to guarantee the electrons are well thermalised with the fridge (via phonons described in Section 2.1.6), and the temperatures are well spaced enough to create a variety of distinct phase traces, which helps the calibration. The difference in temperature is crucial for the calibration to estimate realistic parameters within the physical model.

A single least-squares fit of Equation 3.5 was performed on the collection of phase traces for all three temperatures. Some example phase traces from the calibration fit are shown in Figure 4.1. The model was fitted simultaneously to all the phase traces by adjusting α, Γ and A. These three parameters have a fixed value across all of the calibration data and they are distinct enough to avoid crossover in the fitting. Each phase trace has an individual fit for ϕ_0 and V_0, which are both trivial to define for each phase trace, so they have very little influence on the fitting of α, Γ and A. All the calibration data was taken at 2 K and above, so it is assumed that the electrons are well thermalised with the fridge temperature, i.e $T_e = T_f$, in Equation 3.5

The IO calibration fit estimated the values of the model parameters to be $\alpha = 0.74 \pm 0.02$, $\Gamma = 270 \pm 20$ ns^{-1} and $A = 5.13 \pm 0.06$ rad pF^{-1}. This implies $\Gamma \gg 2\pi f_0$, therefore dissipative effects are assumed not to occur and the cyclic tunnelling is considered adiabatic. The parameter estimate error from the fit (detailed in Section 2.2.2) is low ($< 3\%$), suggesting there was no issue with crossover between the parameters during the fit. With the three
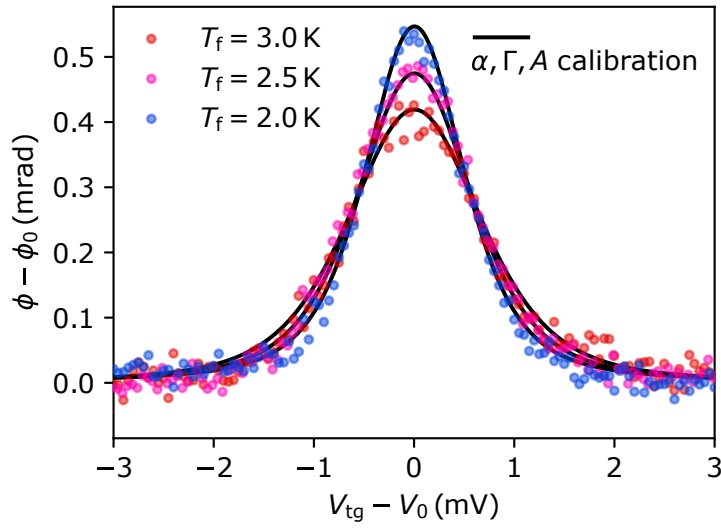
Figure 4.1: QD thermometer calibration in IO cryostat, showing three experimental phase traces taken at fridge temperatures $T_f = 2.0, 2.5, 3.0$ K. The fridge temperature T_f is read from a ruthenium oxide resistance thermometer thermally linked to the FET device. Each trace shows the change in reflected signal phase $\phi - \phi_0$ against top gate voltage $V_{tg} - V_0$, where V_0 is the location of the QD Coulomb peak. The solid black lines show the least-square fit of Equation 3.5 onto the data, assuming the electron temperature T_e equals the fridge thermometer readout T_f. This calibration procedure estimates $\alpha = 0.74 \pm 0.02$, $\Gamma = 270 \pm 20 \, \text{ns}^{-1}$ and $A = 5.13 \pm 0.06 \, \text{rad} \, \text{pF}^{-1}$. For each of the three temperatures 10 traces were measured to complete the calibration data, but for clarity this plot only shows one example trace for each temperature group.
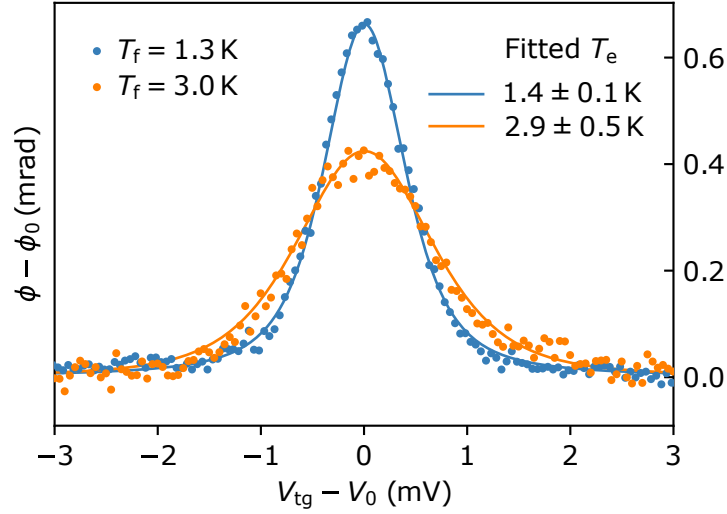
Figure 4.2: Example of electron thermometry in the IO. The data here shows two reflected signal phase $\phi - \phi_0$ measurements against top gate voltage $V_{tg} - V_0$ around the charge degeneracy point of the QD. The fridge temperature T_f is read from a ruthenium oxide resistance thermometer thermally linked to the FET device. The blue and orange points were taken at $T_f = 1.3\,\mathrm{K}$ and $3.0\,\mathrm{K}$, respectively. The blue and orange lines show the fit of the calibrated model (Equation 3.5) to their respective phase trace, which returns an estimate of $T_e = 1.4\,\mathrm{K}$ and $2.9\,\mathrm{K}$, respectively.

parameters estimated completing the physical model, the thermometer was calibrated and ready for thermometry operation.

To test the calibrated electron thermometer, a series of phase traces were taken at varying fridge temperatures between $T_f = 3.0\,\mathrm{K}$ and $1.3\,\mathrm{K}$. The fridge temperature was stepped by $0.1\,\mathrm{K}$ intervals and at each temperature 10 phase traces were measured. This range contains temperatures lower than the calibration data to test if the the model can capture the QD behaviour at lower temperatures. The electron temperature T_e is estimated by fitting Equation 3.5 to the sweep, equipped with the values $\alpha = 0.74 \pm 0.02$, $\Gamma = 270 \pm 20\,\mathrm{ns}^{-1}$ and $A = 5.13 \pm 0.06\,\mathrm{rad\,pF}^{-1}$ (from the calibration). A demonstration of operating the calibrated thermometer is shown in Figure 4.2. A single electron thermometry fit has three fitting parameters, T_e, ϕ_0 and V_0, although the last two are trivial to define.

To verify the validity of the electron thermometry, the QD thermometer electron temperature readout, T_e, was compared with the fridge temperature, T_f, in Figure 4.3. The results show a striking agreement between the QD
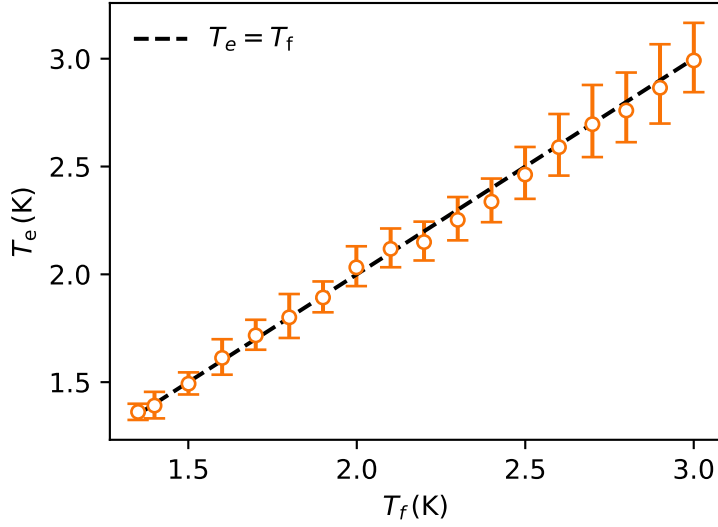
Figure 4.3: Electron temperature T_e readout from QD thermometer in the IO cryostat for various fridge temperatures. The fridge temperature T_f is read from a ruthenium oxide resistance thermometer thermally linked to the FET device. The dashed line highlights where $T_e = T_f$. The T_e error bars show the standard error from the fitting.

electron thermometer and fridge thermometer, even down to temperatures much lower than the calibration data. This suggests that the calibration had been successful in modelling the system, as it correctly predicted the temperature dependence of the phase trace curve at lower temperatures. The physical model accurately predicted the influence of the tunnelling and thermal broadening mechanisms. This is discussed in detail in Section 4.6.

To operate the thermometer in its fastest readout mode, the QD was tuned to the centre of the Coulomb peak where $V_{tg} = V_0$ so that $\phi - \phi_0 = \phi_{MAX}$. The value of ϕ_{MAX} can be converted into an electron temperature using the calibrated Equation 3.5, with the assumption $V_{tg} = V_0$. To test faster electron temperature readout the maximum phase ϕ_{MAX} was monitored at different values of T_f, and compared with the prediction from Equation 3.5 (assuming $T_e = T_f$), shown in Figure 4.4. Each reading of ϕ_{MAX} took ≈ 0.3 s. The ϕ_{MAX} data and the model prediction line up well, so the physical model can be used to convert ϕ_{MAX} to T_e.
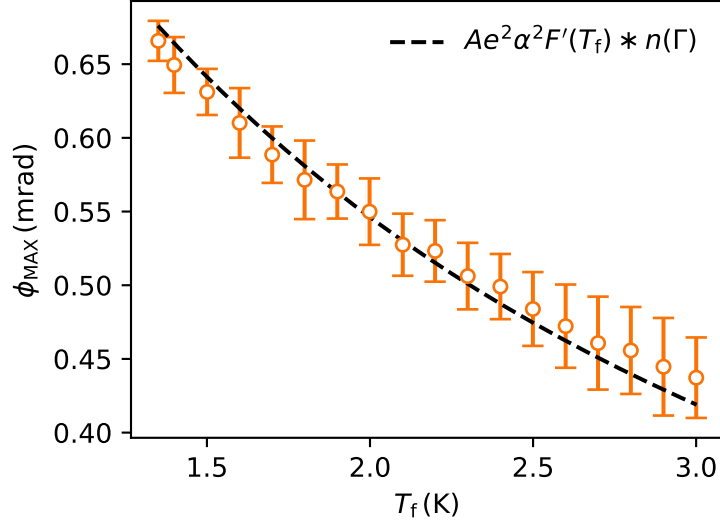
Figure 4.4: Maximum phase ϕ_{MAX} readout from QD thermometer in the IO cryostat for a variety of fridge temperatures. ϕ_{MAX} is the peak phase measured at the centre of the QD Coulomb peak $V_{\text{tg}} = V_0$. The fridge temperature T_{f} is read from a ruthenium oxide resistance thermometer thermally linked to the FET. The dashed line represents the model prediction (not a fit) from calibrated Equation 3.5 assuming both $V_{\text{tg}} = V_0$, and $T_{\text{f}} = T_{\text{e}}$.

4.3　LD250 Cryostat Results

This section details the results of the QD thermometer calibration and electron thermometry from within the LD250 dilution refrigerator, at fridge temperatures in the range of $0.2 < T_{\text{f}} < 1.6\,\text{K}$. This experiment tests to see if the QD thermometer calibration and operation work in a completely different system, and also to find the low temperature limit of the thermometer. The exact same FET and tank circuit used in the IO experiment (Section 4.2) were also mounted in the LD250 for this experiment, and the same room temperature electronics were used. The complete circuit can be seen in Figure 3.3. The driving frequency was set to the resonant frequency of the LD250 circuit $f_0 = 593.5\,\text{MHz}$.

To collect the calibration data, the fridge temperature was adjusted by removing some $^3\text{He}/^4\text{He}$ mixture from circulation, which reduces cooling power and causes the mixing chamber temperature to settle at a higher temperature (more information in Section 2.3). At each fridge temperature a set of ~ 100 reflected signal phase traces were taken by sweeping V_{tg} across the
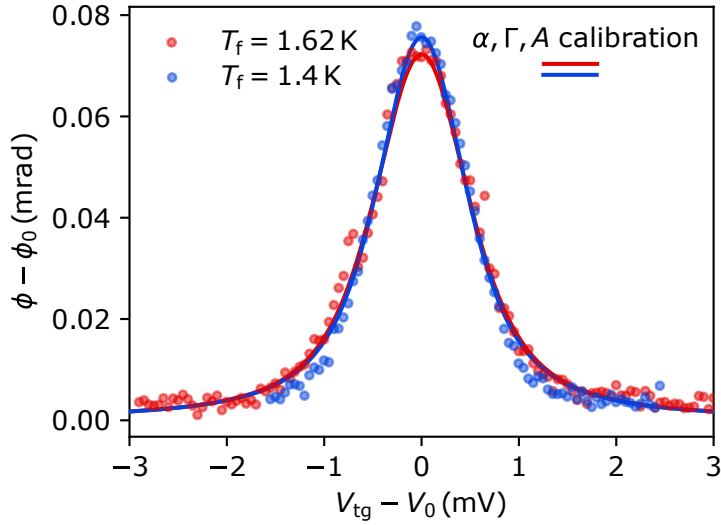
Figure 4.5: QD thermometer calibration in LD250 cryostat, showing two experimental phase traces taken at fridge temperatures $T_f = 1.62, 1.40\,\mathrm{K}$. The fridge temperature T_f is read from a ruthenium oxide resistance thermometer thermally linked to the FET device. Each trace shows the change in reflected signal phase $\phi - \phi_0$ against top gate voltage $V_{tg} - V_0$ around the Coulomb peak of the QD. The solid blue and red lines show the least-square fit of Equation 3.5 onto the data at $T_e = 1.40\,\mathrm{K}$ and $1.62\,\mathrm{K}$, respectively, assuming the electron temperature T_e equals the fridge thermometer readout T_f. This calibration procedure estimates $\alpha = 0.84 \pm 0.03$, $\Gamma = 510 \pm 10\,\mathrm{ns}^{-1}$ and $A = 0.75 \pm 0.07\,\mathrm{rad\,pF}^{-1}$. For each of the three temperatures, 10 traces were measured to complete the calibration data, but for clarity this diagram only shows one example trace for each temperature.

QD Coulomb peak, although for the calibration data only 10 phase traces were chosen at random per temperature. This was done at two particular fridge temperatures $T_f = 1400, 1620\,\mathrm{mK}$. The temperature range is purposely high, when compared to the base temperature of the fridge, to guarantee the electrons are well thermalised with the fridge temperature (via phonons described in Section 2.1.6), and each temperature is well spaced enough to help the calibration.

A single least-squares fit of Equation 3.5 was performed on the collective phase traces across both temperatures, as shown in Figure 4.5. The model was fitted to the phase traces simultaneously by adjusting α, Γ and A. Each phase trace has an individual fit for ϕ_0 and V_0. All the calibration data was

taken at 1.4 K and above, so it can be assumed that the electron temperature is well thermalised with the fridge temperature. Therefore during the calibration fit we assume that $T_e = T_f$ in Equation 3.5, i.e. the fridge temperature reading is interpreted as the electron temperature.

The LD250 calibration fit estimated the values $\alpha = 0.84 \pm 0.03$, $\Gamma = 510 \pm 10\,\text{ns}^{-1}$ and $A = 0.75 \pm 0.07\,\text{rad}\,\text{pF}^{-1}$. This implies $\Gamma \gg 2\pi f_0$, therefore dissipative components were neglected and the cyclic tunnelling was considered adiabatic. The difference in α, Γ and A as compared with the IO calibration can be attributed to the differences between the two cryostat systems and the Si FET having undergone a thermal cycle. For example, the PCB tank circuit is extremely sensitive to the nearby metallic geometry of the fridge, which can change the value A via the top gate parasitic capacitance C_p or QD geometric capacitance C (in Equation 3.6). It seems unlikely that the parasitic capacitance has shifted as the circuit model suggests there is no change (details in Section 3.3.2). Instead, it is possible the geometric capacitance C of the QD has changed. The QD parameters α and Γ are also sensitive to the shape and position of the QD in the Si channel, which are likely to change after a thermal cycle. Also the location of the Coulomb peak is different between the two cryostats (shown in Figure 3.13), which changes the QD geometry during the measurements, which affects C.

The re-calibrated thermometer was then used for electron thermometry. A series of phase traces were taken at the following fridge temperatures $T_f = 180, 630, 1400,$ and $1620,$ mK. At each temperature ~ 100 phase traces were measured, but in the thermometry analysis only 10 phase traces were randomly chosen to be used per temperature. This range contains temperatures lower than the calibration data to test the effectiveness of the calibration. The electron temperature T_e was then estimated by fitting Equation 3.5 to the sweep, equipped with the values $\alpha = 0.84 \pm 0.03$, $\Gamma = 510 \pm 10\,\text{ns}^{-1}$ and $A = 0.75 \pm 0.07\,\text{rad}\,\text{pF}^{-1}$ (from the calibration). Each single electron thermometry fit has three fitting parameters, T_e, ϕ_0 and V_0.

To analyse the electron thermometry, the QD thermometer electron temperature readout T_e was compared with the fridge temperature T_f in Figure 4.6. Using the electron thermometer in a different system at lower temperature
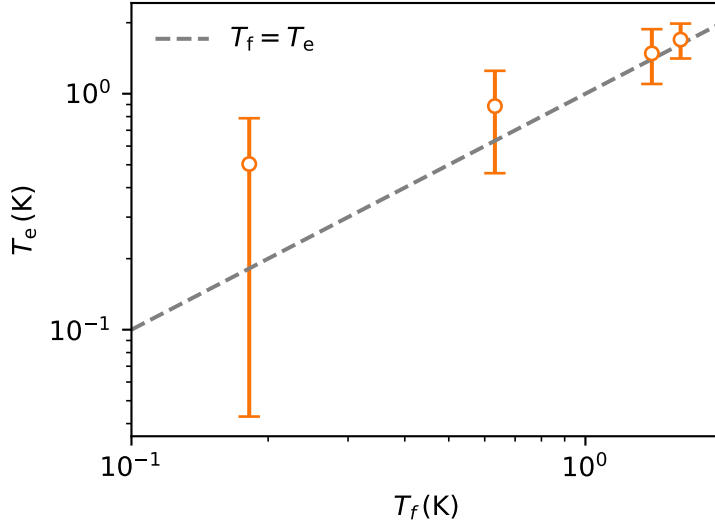
Figure 4.6: Electron temperature T_e readout from recalibrated QD thermometer in the LD250 cryostat, for various fridge temperatures. The fridge temperature T_f is read from a ruthenium oxide resistance thermometer thermally linked to the FET device. The dashed line highlights where $T_e = T_f$. The T_e error bars show one standard deviation of certainty. The readout of T_e deviates from the T_f below 1 K, as the QD goes further into the strongly coupled regime $k_B T_f < \hbar\Gamma$.

gave a reasonable agreement above $T_f = 1\,\text{K}$, despite $k_B T_f \sim \hbar\Gamma$ (from calibration estimation). Below $T_f = 1\,\text{K}$ there was a considerable increase in T_e readout error from the the fit. This is because the thermometer was entering the regime where the QD energy level is strongly tunnel broadened, and therefore C_t has much weaker temperature dependence. This is discussed in detail in Section 4.6. The error for an individual fit of T_e increases with lower temperatures due to the weaker temperature dependence (the calculation of the error is described in Section 2.2.2). The $T_e = T_f$ line does remain with the standard deviation error from the electron thermometry. To compound the issue of strong tunnel broadening, it is likely there are elevated electron temperatures from a weaker electron-phonon coupling (described in Section 2.1.6).

An attempt was made to operate the QD thermometer in a faster readout mode by tuning to the centre of the Coulomb peak where $V_{tg} = V_0$, so that $\phi - \phi_0 = \phi_{MAX}$. The value of ϕ_{MAX} can be converted into an electron temperature using the calibrated Equation 3.5, with the assumption $V_{tg} = V_0$.
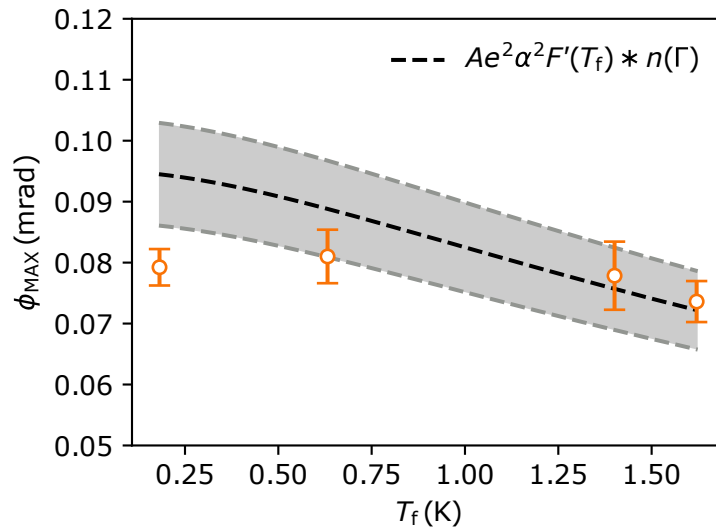
Figure 4.7: Max phase ϕ_{MAX} readout from QD thermometer in the LD250 cryostat for a variety of fridge temperatures. ϕ_{MAX} is the peak phase change measured at the centre of the QD Coulomb peak $V_{\text{tg}} = V_0$. The error on the data points show one standard deviation of certainty based on the range of values measured (not from any fitting procedure). The fridge temperature T_{f} is read from a ruthenium oxide resistance thermometer thermally linked to the FET. The black dashed line represents the model prediction (not a fit) from calibrated Equation 3.5 assuming both $V_{\text{tg}} = V_0$, and $T_{\text{f}} = T_{\text{e}}$. The grey shaded area shows one standard deviation of error in the model prediction.

The maximum phase ϕ_{MAX} was monitored at different values of T_{f}, and compared with the prediction from Equation 3.5 (assuming $T_{\mathrm{e}} = T_{\mathrm{f}}$), shown in Figure 4.4. The ϕ_{MAX} data and the model prediction line up relatively well, however the projection of the calibrated physical model into lower temperatures deviates slightly from what was then measured at low temperatures. The height of all the phases traces is almost constant, which is due to dominant tunnel brodening. This means that ϕ_{MAX} thermometry can not be done accurately below 1 K with this particular FET. The solution to this problem is to reduce the tunnel coupling.

4.4 Validity of Physical Model

The calibration process described in Sections 4.1 produces estimations for the parameters α, Γ and A from Equation 3.5, each of which represent a real physical property in the model. To verify the validity of the calibration fit, a stability diagram of the QD was measured for both the IO and the LD250 experiments. To do this, the FET source and drain connections were ungrounded to apply a source-drain voltage V_{sd} over the QD.

In the IO, the charge stability diagram was measured by monitoring the source-drain current I_{sd} as both V_{sd} and V_{tg} were adjusted, shown in Figure 4.8. Using the relationship from Equation 2.20 the value for α predicted by the calibration fit was added onto the stability diagram in the form of two gradients; the gradient along the 'drain resonance' side of a Coulomb diamond $m_d = \Delta V_{\mathrm{tg}}^d / \Delta V_{\mathrm{sd}}^d$ and the 'source resonance' side $m_s = \Delta V_{\mathrm{tg}}^s / \Delta V_{\mathrm{sd}}^s$. The drain resonance and source resonance cross at the location of the Coulomb peak used in the thermometry. The calibrated lever arm $\alpha = 0.74 \pm 0.02$ matches well with the Coulomb diamond geometry, suggesting the value has been correctly estimated. Above and below the thermometry Coulomb peak, the order of magnitude of the source-drain current $|I_{\mathrm{sd}}|$ from the unblockaded QD was found to be $\sim 10\,\mathrm{nA}$. This agrees with the calibration fit prediction of the tunnel coupling $\Gamma = 270 \pm 20\,\mathrm{ns}^{-1}$ which suggests a source-drain current of $e\Gamma \sim 6.9 \pm 0.5\,\mathrm{nA}$. The agreement of both α and Γ between the calibration prediction and the measured stability diagram suggest strongly that the physical model is accurate. Considering the calibration is based on

Figure 4.8: Charge stability diagram measured from source-drain transport, in the IO cryostat. V_{tg} is the top gate voltage, V_{sd} is the source-drain voltage and $|I_{sd}|$ is the source-drain current, plotted in log scale. The fridge was held at temperature $T_f = 1.268 \pm 0.001$ K. Red lines highlight the source and drain resonance gradients, m_s and m_d, respectively, which match up with the calibration fit lever arm prediction, $\alpha = 0.74 \pm 0.02$, via Equation 2.20. The two gradients cross at the the Coulomb peak where the thermometry took place. Here the on-resonance current has an order of magnitude $I_{sd} \sim 10$ nA, which is similar to the single electron current defined by the calibration fit tunnel coupling $e\Gamma \approx 6.9 \pm 0.5$ nA.
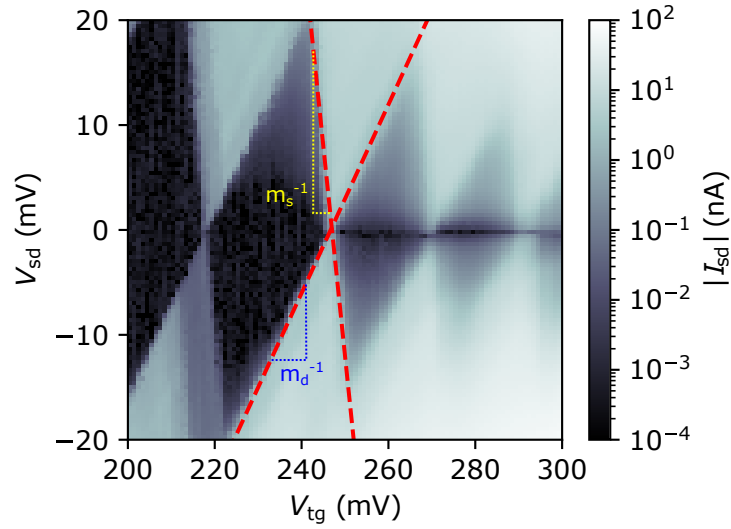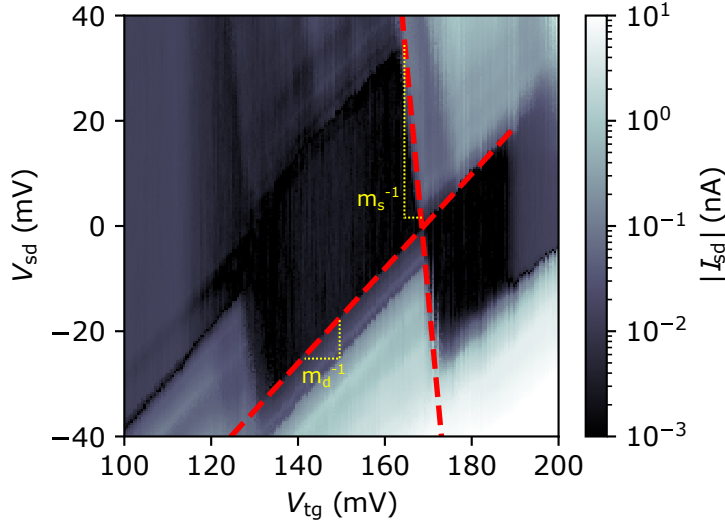
Figure 4.9: Charge stability diagram measured from source-drain transport, in the LD250 cryostat. V_{tg} is the top gate voltage, V_{sd} is the source-drain voltage and $|I_{sd}|$ is the source-drain current, plotted in log scale. The fridge was held at temperature $T_f = 8.70 \pm 0.05$ mK. Red lines highlight the source and drain resonance gradients, m_s and m_d, respectively, which match up with the calibration fit lever arm prediction, $\alpha = 0.84 \pm 0.03$, via Equation 2.20. The two gradients cross at the the Coulomb peak where the thermometry took place. Here the on-resonance current has a order of magnitude $I_{sd} \sim 10$ nA, which is similar to the single electron current defined by the calibration fit tunnel coupling $e\Gamma \approx 13.1 \pm 0.3$ nA.

measurements made at three relatively high temperatures, the technique is good at characterising the QD and predicting how it will behave at lower temperatures.

In the LD250, the charge stability diagram was also measured, shown in Figure 4.9. Using the relationship from Equation 2.20 the value for α predicted by the calibration fit was added onto the stability diagram in the form of the source and drain resonance gradients that cross at the location of the Coulomb peak used in the thermometry. The calibrated lever arm $\alpha = 0.84 \pm 0.03$ matches well with the Coulomb diamond geometry, suggesting the value has been correctly estimated. This demonstrates that this single-gate technique to measure the lever arm of a QD is a reliable technique across independent experiments in different systems. Above and below the thermometry Coulomb peak, the order of magnitude of the source-drain current $|I_{sd}|$ from the unblockaded QD was found to be ~ 10 nA. This agrees with the

calibration fit prediction of the tunnel coupling constant $\Gamma = 510 \pm 10\,\text{ns}^{-1}$ which suggests a source-drain current of $e\Gamma \sim 13.1 \pm 0.3\,\text{nA}$.

In both the IO and the LD250 the calibration has correctly estimated the top gate lever arm, despite the change in value. This demonstrates that the lever arm of a QD can be obtained using a single non-galvanic gate connection, and measurements spanning a range of temperatures. The appropriate estimations of Γ provide more evidence that this technique completes a realistic model of the QD broadening.

4.5   Electron Temperature Error Analysis

This section takes a necessary look at the confidence in the electron thermometry. This includes the electron temperature readout certainty for the fitting procedure in Section 4.5.1, and the temperature sensitivity when measuring ϕ_{MAX} in Section 4.5.2.

4.5.1   Phase Trace Fit Error

The electron thermometry error is an important parameter as it shows where the temperature limits of this technique lie. The thermometry readout for T_{e} is meaningless if there is no certainty in the measurement. To quantify the error, a constant Chi-square boundary technique is used during the fit for T_{e}.

The technique used here involves forcing a range of guesses for T_{e}, and observing how well the model fits the phase trace. The calibrated estimates of α, Γ and A are included in the phase model Equation 3.5, leaving only electron temperature T_{e} as a fitting parameter, along with ϕ_0 and V_0. We assume that for a given phase trace at constant temperature, each phase data point has a measurement error that is random within the same normal Gaussian distribution, with standard deviation σ, i.e. $\sigma_i = \sigma$ for all phase data points i. Therefore from equation 2.47, for a given phase trace, each guess of T_e returns a goodness of fit χ^2 that can be quantified via

$$\chi^2 = \sum_{i=0}^{N-1} \frac{[\phi^i - \phi(V_{\text{tg}}^i|T_{\text{e}}, \phi_0, V_0)]^2}{\sigma(N-3)}, \tag{4.1}$$

where N is the number of data points in the phase trace, ϕ^i and V_{tg}^i are the values of phase and top gate voltage, respectively, for the ith data point [51]. It is the case that σ vary between traces, for example if the temperature is different. The minimum value of χ^2, which we will label χ^2_{min}, corresponds to the final fit estimate for T_e, and should meet the condition $\chi^2_{min} < 10$ if the fit is good. To work out the certainty of this measurement, a constant confidence boundary of $\chi^2_{min} + 1$ surrounds χ^2_{min}, creating an interval which represents one standard deviation of confidence (described in Section 2.2.2). Because ϕ_0 and V_0 are trivial to define, they have very little impact on the goodness of the fit, so we can plot χ^2 against the proposed guess for T_e to see where the confidence boundaries lie.
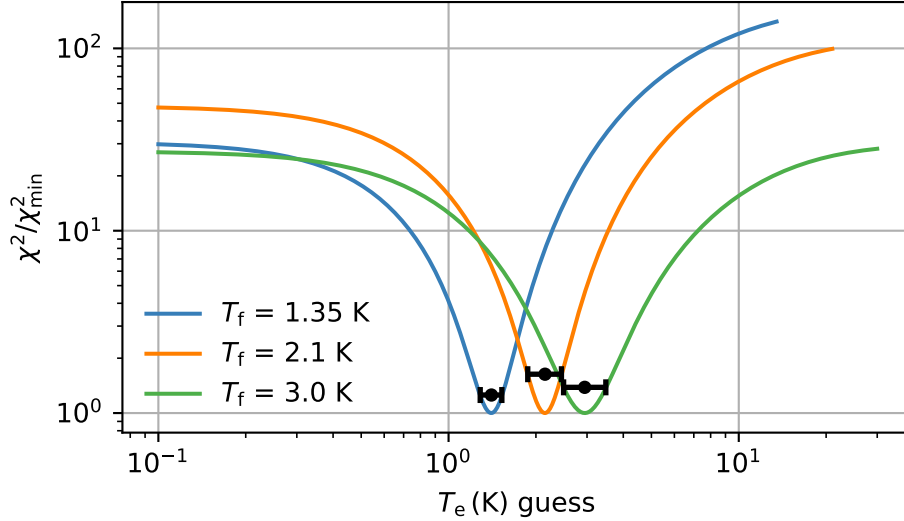

Figure 4.10: Electron thermometry goodness of fit χ^2/χ^2_{min}, against electron temperature T_e guess, for a variety of phase traces from the IO cryostat. Three example phase traces are taken from fridge temperatures at $T_f = 1.35\,K$, $2.1\,K$ and $3.0\,K$. The black points represent the T_e fit where χ^2 is minimum. The height of these points is the confidence boundary $\chi^2 = \chi^2_{min} + 1$ which defines the confidence region shown by the error bars, representing one standard deviation of uncertainty.

First we will take a look at the error for the IO electron thermometry. Figure 4.10 demonstrates this process with a few example phase traces taken at fridge temperatures of; $T_f = 3.0\,K$, $2.1\,K$ and $1.35\,K$. The location of χ_{min} is well defined, with one standard deviation of uncertainty being around $\pm 10\%$ for a single readout of T_e. The condition $\chi_{min} < 10$ is true for all the phase

traces, which indicates a good quality fit. The confidence boundary decreases with lower fridge temperature. This is because the thermal noise and charge noise are both reduced and the signal height ϕ_{MAX} is larger, which both contribute to a tighter tolerance on the model fit.
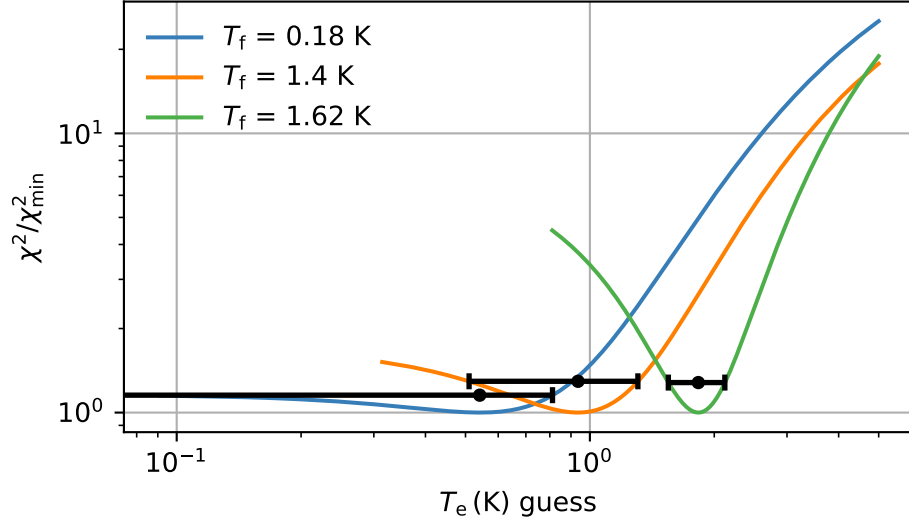

Figure 4.11: Electron thermometry goodness of fit $\chi^2/\chi^2_{\mathrm{min}}$, against electron temperature T_{e} guess, for a variety of phase traces from the LD250 cryostat. Three example phase traces are taken from fridge temperatures at $T_{\mathrm{f}} = 0.18\,\mathrm{K}$, $1.4\,\mathrm{K}$ and $1.62\,\mathrm{K}$. The black points represent the T_{e} fit where χ^2 is minimum. The height of these points is the confidence boundary $\chi^2 = \chi^2_{\mathrm{min}} + 1$ which defines the confidence region shown by the error bars, representing one standard deviation of uncertainty.

Now we will take a look at the error for the LD250 electron thermometry. Figure 4.11 demonstrates this process with a few example phase traces taken at fridge temperatures of $T_{\mathrm{f}} = 0.18\,\mathrm{K}$, $1.4\,\mathrm{K}$ and $1.62\,\mathrm{K}$. At $T_{\mathrm{f}} > 1\,\mathrm{K}$, the location of χ_{min} is well defined, with one standard deviation of uncertainty being around $\pm 20\%$ for a single readout of T_{e}. Pushing the QD thermometer to its lower temperatures creates a transition from having a single clear location of χ_{min}, to a regime where there is a large spread of possible T_e values, all of similar validity. This represents the area where the tunnel coupling dominates the thermal energy, i.e $k_{\mathrm{B}}T_{\mathrm{e}} < \hbar\Gamma$, so the thermal energy has very little impact on the phase trace shape. The dependence of the measured trace on electron temperature gets weaker with lower values. Despite this, the condition $\chi_{\mathrm{min}} < 10$ is true for all the phase traces, which indicates a good fit. At

$T_f = 0.18\,\text{K}$, some of the T_e error bar lower bounds extend towards $0\,\text{K}$. At this point it can be said the QD thermometer has reached its lower temperature limit for operation.

4.5.2 Max Phase Sensitivity

Measuring the maximum phase ϕ_{MAX} has been demonstrated to work as a fast method of electron readout above $1\,\text{K}$, for the particular FET used, in Section 4.2. The precision of this measurement is improved with more averaging. An experiment was carried out to determine the sensitivity of the ϕ_{MAX} thermometry for this particular experimental set-up and equipment. The analogue to digital converter used to record the demodulated return signal has a maximum sample rate of $1.25\,\text{Ms}^{-1}$. For each value of ϕ, the demodulator chip output voltages I_{LO}, I_{HI}, Q_{LO} and Q_{HI} (details in Section 3.3.3) all need to be recorded simultaneously. Therefore the maximum sample rate for recording phase is $0.26\,\text{Ms}^{-1}$.

With the FET and circuit mounted in the LD250, a single set of phase data was taken for $60\,\text{s}$ at the maximum sample rate (15.6 million phase values). This was divided into 128 sets of data, each of which was converted into a phase spectral density estimation via Welch's method [82]. The 128 spectral densities were averaged, producing Figure 4.12. The background spectral density is notably flat, although there are features on top of the flat background. These spikes are much narrower than their typical spacing (most only having a single data point), therefore contribute relatively little to the total noise. Averaging the spectral density over the entire bandwidth gives an effective white noise phase sensitivity of $1.1 \pm 0.1\,\mu\text{rad}/\sqrt{\text{Hz}}$. From the IO calibration of Equation 3.5 (with the condition $V_{\text{tg}} = V_0$), we can use $\text{d}\phi/\text{d}T_e$ to convert the phase spectra into a temperature spectra. This gives an approximate white noise temperature sensitivity of $11 \pm 1\,\text{mK}/\sqrt{\text{Hz}}$ at $3.0\,\text{K}$, and $4.0 \pm 0.3\,\text{mK}/\sqrt{\text{Hz}}$ at $1.3\,\text{K}$. For example, if ϕ_{MAX} is recorded with measurement frequency of $10\,\text{Hz}$ at a fridge temperature of $1.3\,\text{K}$, the error in the recorded T_e data would be $\pm14\,\text{mK}$. There was a similarity between the noise measured on the tail and peak of the phase trace. This suggests that the noise measured is dominated by the experimental measurement chain, and the QD
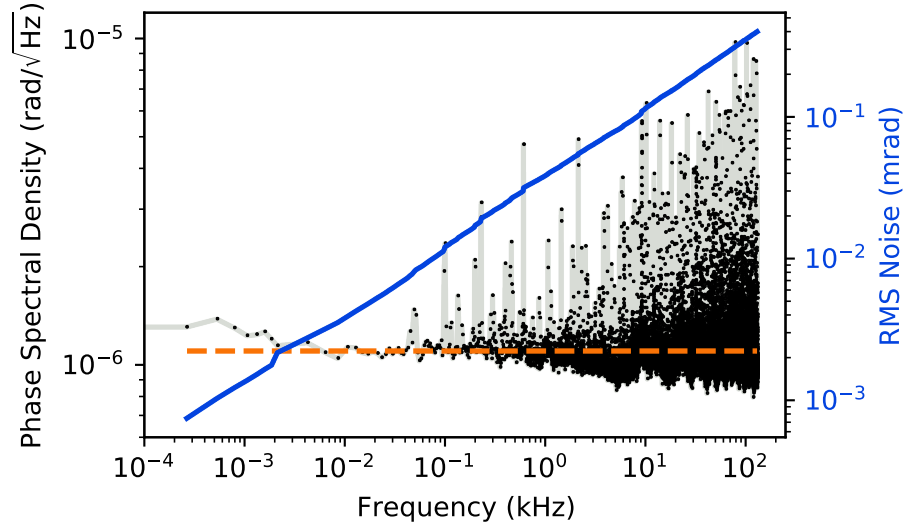
Figure 4.12: Spectral density of reflected phase readout from RF reflectometry taken at 8.7 mK in the LD250 cryostat. A total of 2^7 samples of phase data were read, each one at a sample rate of $2.6 \times 10^5 \, \text{s}^{-1}$ for 0.5 s, and converted to a spectral density via the Welch's method, represented by the black data points linked with grey lines (left y-axis). The spectral densities were averaged to produce the plot. The blue line shows the total RMS phase noise (right y-axis), which is the integral of the spectral density between 0.27 Hz and the frequency indicated. The orange dashed line corresponds to the average spectral density over the whole bandwidth, which is equal to a effective white noise phase sensitivity of $1.1 \pm 0.1 \, \mu\text{rad}/\sqrt{\text{Hz}}$.

charge noise (which would likely have a $1/f$ dependence) is somewhere underneath this noise floor. Therefore, the sensitivity values mentioned here are not device limited.

4.6   Quantum Dot Energies and Behaviour

Several energy scales are involved in the experiment that impact the behaviour of the QD, described in Section 2.1.2. The magnitude of the tunnel coupling is of particular interest as a strongly tunnel coupled QD limits the range of electron thermometry [28]. Here we show the different energy scales for the experiments in both cryostats, and use them to explain the thermometer's behaviour. A brief look at how electron spin effects the location of the Coulomb peak, V_0, is also included.

The tunnel coupling $\hbar\Gamma$ is estimated from the QD thermometer calibration process. The QD excited state confinement energy E_{con} and QD charging energy $E_c = e\Delta V_{sd}$ can be observed from the stability diagram. To extract the voltage ΔV_{sd}, the average height was taken from the Coulomb diamonds on either side of the conduction resonance where the thermometry was performed. The confinement energy is measured by $E_{con} = -e\alpha\Delta V_{tg}^{con}$, where ΔV_{tg}^{con} is the difference in top gate voltage between the drain resonance and the first observed excited state, which is detected from an increase in source drain conduction.
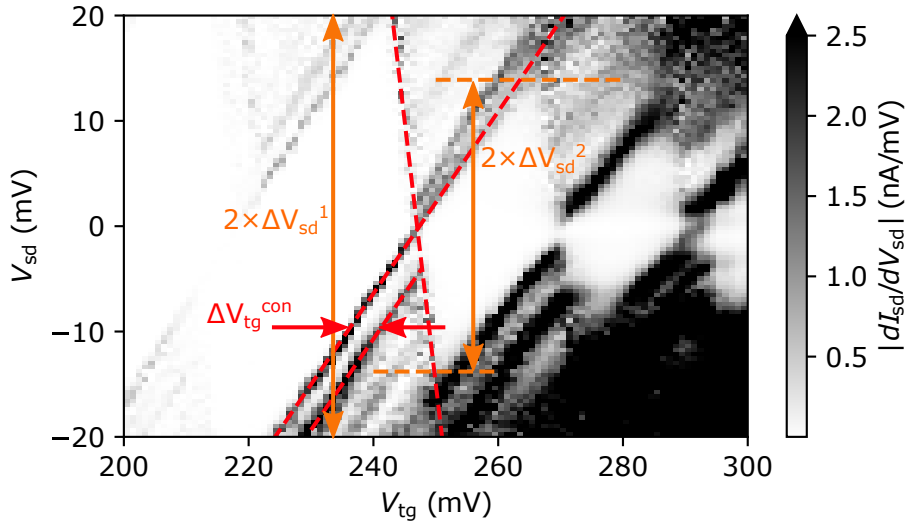

Figure 4.13: QD stability diagram from IO mounted FET. V_{tg} is top gate voltage, V_{sd} is source-drain voltage and I_{sd} is source-drain current. The black and white scale shows the differential of the source-drain current with respect to the source-drain voltage $|dI_{sd}/dV_{sd}|$. The crossed red dashed lines highlight the Coulomb resonance where the thermometry was performed, and the gradients correspond to the lever arm as measured from the QD calibration process, $\alpha = 0.74 \pm 0.02$. The lowest red dashed line highlights the first excited state of the QD. ΔV_{tg}^{con} is the corresponding top gate voltage interval for the first excited state. ΔV_{sd}^1 and ΔV_{sd}^2 represents the height of the Coulomb diamonds to the left (1) and to the right (2) of the thermometry Coulomb peak, respectively. The charging energy can therefore be estimated as $E_c = e(\Delta V_{sd}^1 + \Delta V_{sd}^2)/2$.

For the IO experiment, the stability diagram gives a charging energy of $E_c = 16.9$ and a confinement energy of $E_{con} = 3.7$, which are estimated from ΔV_{sd} and $\Delta V_{pg}^{(con)}$, shown in Figure 4.13. The thermal energy $k_B T_e$ is approximately

extracted from the range of fridge temperatures used during the experiment, $1.3 < T_f < 3.0$ K. The tunnel coupling from the calibration process gives $\Gamma = 270 \pm 20\,\text{ns}^{-1}$.
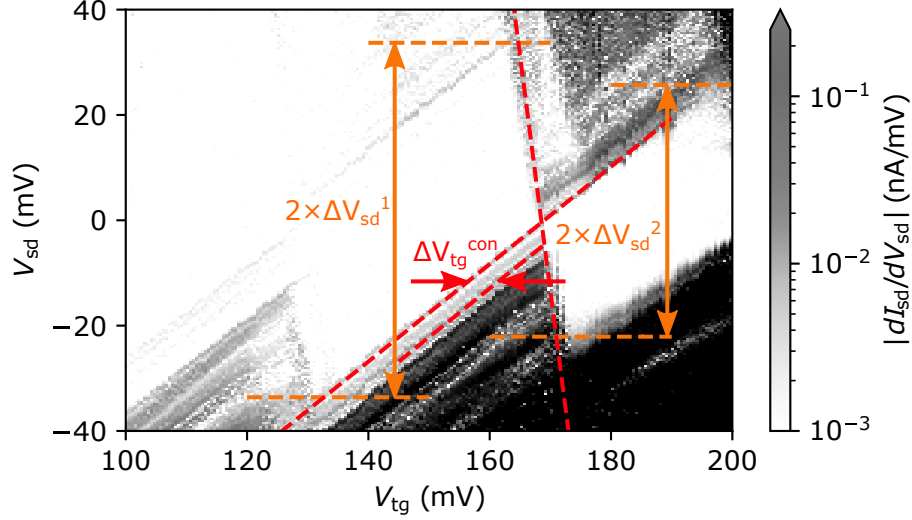

Figure 4.14: QD stability diagram from LD250 mounted FET. V_{tg} is top gate voltage, V_{sd} is source-drain voltage and I_{sd} is source-drain current. The black-and-white map shows the magnitude of the source-drain current differential with respect to the source-drain voltage $|dI_{\text{sd}}/dV_{\text{sd}}|$, in log scale. The crossed red lines highlight the Coulomb resonance where the thermometry was performed, and the gradients correspond to the lever arm as measured from the QD calibration process, $\alpha = 0.84 \pm 0.03$. The lowest red line highlights the first excited state of the QD. $\Delta V_{\text{tg}}^{(\text{con})}$ is the corresponding top gate voltage interval for the first excited state. $\Delta V_{\text{sd}}^{(1)}$ and $\Delta V_{\text{sd}}^{(2)}$ represents the height of the Coulomb diamonds to the left (1) and to the right (2) of the thermometry Coulomb peak, respectively. The charging energy can therefore be estimated as $E_c = e(\Delta V_{\text{sd}}^{(1)} + \Delta V_{\text{sd}}^{(2)})/2$.

For the LD250 experiment, the stability diagram gives a charging energy of $E_c = 28.8$ and a confinement energy of $E_{\text{con}} = 4.2$, shown in Figure 4.14 . The thermal energy $k_B T_e$ is approximated from the range of electron temperatures measured during the experiment, $0.18 < T_f < 1.62$ K, assuming the electron temperatures are roughly similar. The tunnel coupling from the calibration process gives $\Gamma = 510 \pm 10\,\text{ns}^{-1}$.

All the energy scales for both systems are stated in Table 4.1 for comparison.

Energy Scale	$k_B T_e$	$\hbar\Gamma$	E_{con}	E_c
Cryogen-free 1K cryostat	$0.12 - 0.26$	0.18	3.7	16.9
Dilution refrigeration system	$0.015 - 0.14$	0.32	4.2	28.8

Table 4.1: Energy scales associated with the experiments in the two fridge systems. T_e is the electron temperature, which has been obtained from the fit of the model to the experimental data. The experiments took place over a range of temperatures, so the thermal energy scale is shown as a range. Γ is the QD tunnel rate. E_{con} is the confinement energy for the first excited state in the QD. E_c is the charging energy for the QD.

From these measurements and estimates, we can say that for the IO experiment, the hierarchy of energy scales was

$$k_B T_e \sim \hbar\Gamma < E_{con} < E_c. \tag{4.2}$$

In this case the Coulomb-blockaded QD was affected significantly, but not dominated, by tunnel coupling. The tunnel coupling is included within the physical model, and so when the calibration fit was performed it was technically estimating the balance between the two main broadening mechanisms, tunnelling and thermal. The thermometry in Figure 4.3 works well because the calibration correctly predicts how the two broadening mechanisms affect the phase trace, at different electron temperatures. For the LD250 experiment, the hierarchy of energy scales was

$$k_B T_e < \hbar\Gamma < E_{con} < E_c. \tag{4.3}$$

In this case the Coulomb-blockaded QD was strongly tunnel coupled, and the tunnel broadening was consistently larger than the thermal broadening within the fridge temperature range tested. This makes the electron temperature dependence of the phase trace much weaker, and as the temperature was reduced it weakened further. This is what is observed in Figure 4.6, where the QD thermometer reaches its lower temperature limit at around $T_e \sim 0.2\,\text{K}$. To use the thermometer at lower temperatures, the tunnel broadening must be reduced to allow the thermal broadening more influence on the phase trace. This can sometimes be done by applying a negative back gate voltage to increase the tunnel barrier resistance. Another effective solution is to use a different QD geometry, where the source and drain contacts
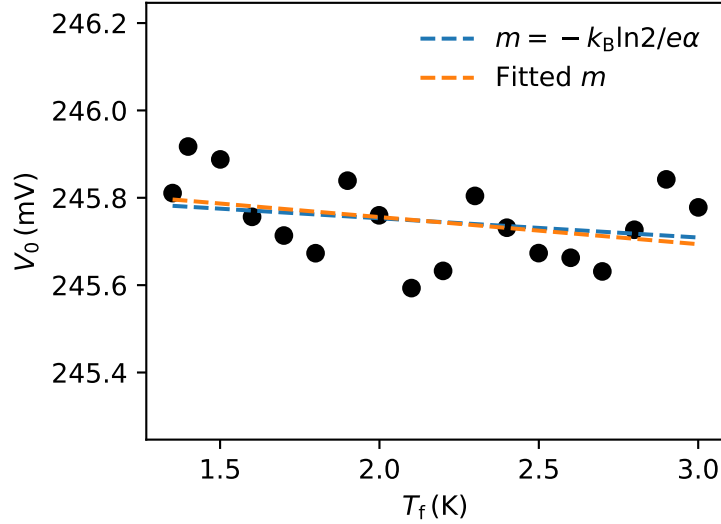
are less strongly coupled to the QD.

Figure 4.15: Location of the Coulomb Peak centre, V_0, against fridge temperature, T_f, in the IO cryostat. The voltage V_0 represents where the QD occupation probability $P_{QD} = 1/2$. The orange line shows the theoretical temperature dependence of V_0 with a gradient of $m = k_B \ln 2 / e\alpha \, \text{VK}^{-1}$. The green line shows a linear fit to the data which predicts a gradient of $m = -(6 \pm 4) \times 10^{-5} \, \text{VK}^{-1}$.

It has been shown that for a QD-reservoir system, the QD state has a different spin degeneracy corresponding to N and $N + 1$ electrons in the QD. This creates a temperature dependence for the value of QD energy which creates $1/2$ occupation probability, described by Equation 2.40 in Section 2.1.5. The top gate voltage value for $P_{QD} = 1/2$, labelled V_0, is recorded for each phase trace measured across a range of temperatures. Figure 4.15 shows a subtle negative correlation between V_0 and the fridge temperature T_f. The theoretical gradient $dV_0/dT_f = -k_B \ln 2 / e\alpha \, \text{VK}^{-1}$ is certainly believable when compared with the measured V_0, and a linear fit returns $dV_0/dT_f = -(6 \pm 4) \times 10^{-5} \, \text{VK}^{-1}$. Although the correlation is clouded by charge noise, the relationship between V_0 and T_f is consistent with the theory.

4.7 Discussion

In summary, the QD thermometer built in Chapter 3 was successfully calibrated and operated as an electron thermometer with a single capacitive gate

in two separate cryostats. This introduces and demonstrates a new level of simplicity and versatility for measuring electron temperature.

The thermometer was calibrated via a single fitting of a physical model to reflected RF signal phase data taken at 2.0 K, 2.5 K and 3.0 K, within the IO cryostat. The calibration uses limited data to generate a physical model of the QD-reservoir system, which correctly estimates physical parameters such as the QD top gate lever arm. Electron thermometry was successfully performed with the calibrated QD thermometer in a 1.0 K to 3.0 K range. The QD thermometer was also used for faster readout by monitoring the phase when the QD has an occupation probability of 1/2. In this mode of operation the QD thermometer was shown to have a sensitivity of $4.0 \pm 0.3 \, \text{mK}/\sqrt{\text{Hz}}$ and $11 \pm 1 \, \text{mK}/\sqrt{\text{Hz}}$, at 1.3 K and 3.0 K, respectively.

The thermometer was also calibrated via a single physical model fit to data taken at 1.40 K and 1.62 K, within the LD250 cryostat. The calibration procedure once again correctly estimated physical parameters such as the QD top gate lever arm. Electron thermometry was performed with the calibrated QD thermometer down to 0.18 K. The QD thermometer can even operate in the case where $k_\text{B} T_\text{e} \sim \hbar \Gamma$, however with the system and techniques used here, the thermometry uncertainty starts to increase below 1 K due to strong tunnel coupling. Careful analysis of the thermometry uncertainty reveals the coldest limit of the QD thermometer, when the electron temperature confidence boundary increases dramatically and extends towards 0 K.

The ability to fully calibrate and operate a non-galvanic electron thermometer with a single RF line simplifies the application of the device substantially. This device provides a versatile, sensitive and effective tool for monitoring electron temperature in nanoelectronic devices at cryogenic temperatures.

Looking to the future, an appropriately redesigned FET geometry could allow a QD to form with a reduced tunnel rate. This would reduce the influence of tunnel broadening and allow more accurate electron temperature readout at lower temperatures.

Chapter 5

New Thermal Insulators for Sub-Kelvin Environments

This chapter will describe our experiments demonstrating new methods of improving insulation within sub-Kelvin environments. We present results on plastic-based solid-void structures, including a structure fabricated from commercially available modular 'LEGO' blocks, and three other custom designs fabricated using a 3D printer, described in Section 5.1. A detailed description of the thermal conductivity experiment is included in Section 5.2, and the results are shown in Chapter 5.3, where the samples tested are found to have excellent properties as a low temperature insulator. The significance of these results is discussed in Chapter 5.4. Some of these results are published in Scientific Reports [31].

5.1 New Insulator Sample Designs

We investigated several structures to be used as insulators within low temperature environments. The objective was to create a mechanically strong solid-void structure which maximises thermal insulation whilst retaining good strength. All the samples discussed here are shown in Figure 5.1.

The first sample is a readily available commercial solution: a modular acrylonitrile butadiene styrene (ABS) structure comprised of four standard LEGO block elements (Catalog No 3001) stacked vertically. These elements are injection moulded with a precision of $\sigma_x \approx 5\,\mu$m [84], so each element is almost
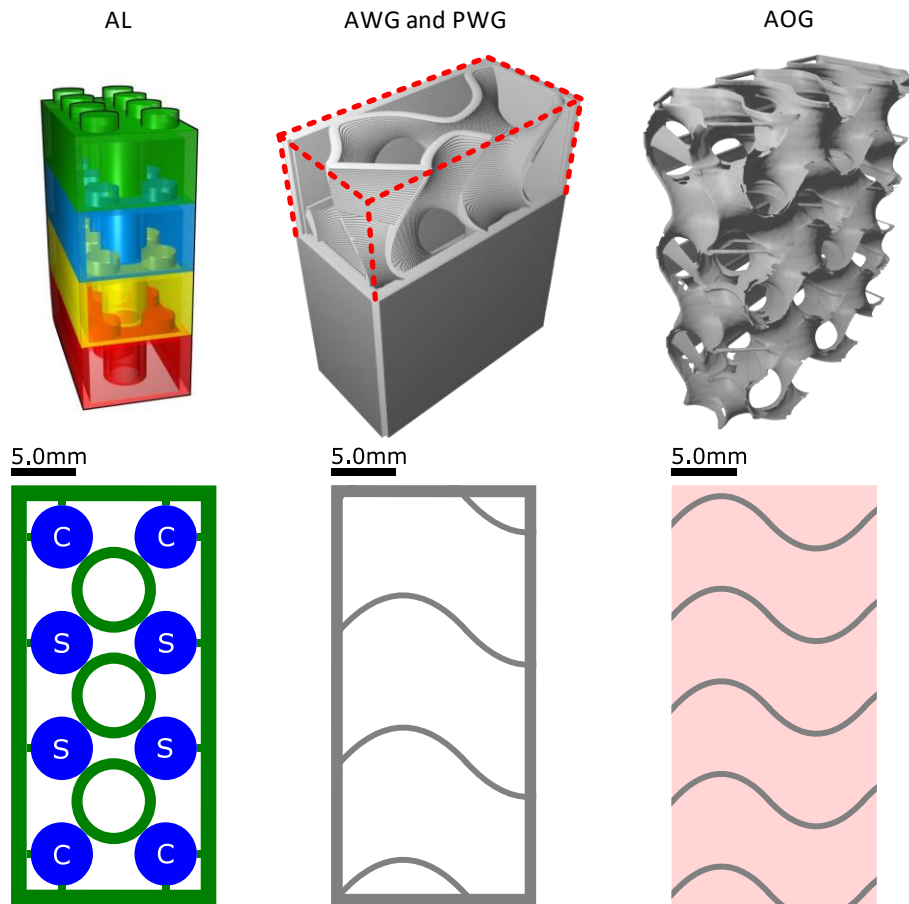
Figure 5.1: A 3D render (**top**) and cross-section (**bottom**) for each of the three solid-void insulators tested. Sample AL (**left**) is fabricated from four modular ABS LEGO elements (Catalog No 3001) stacked vertically [83]. The cross section shows the interface between the green and blue elements. The green shaded area is against the surface of the blue element below, however the blue shaded area does not contact the green element above, but clutches to the green element via friction between the two geometries, with a height of 1.8 mm. There are four such corner connections and four side connections, labelled 'C' and 'S' respectively. Samples AWG and PWG (**centre**) are 3D printed walled gyroid structures, fabricated with ABS and PLA filaments respectively, and have a 5% volume fill factor. The cross-section shows an example of the walled gyroid geometry in the x-y plane, but this geometry will change depending on where the sample is sliced. Sample AOG (**right**) is the 3D printed open gyroid structures, fabricated with ABS filament and an 8% volume fill factor. The cross-section shows an example of the gyroid geometry in the x-y plane, but this geometry will change depending on where the sample is sliced.

identical. The elements were held together entirely by their interlocking geometry clamping power, with no added adhesive material. The sample had a total height of $h = 40.2$ mm, length $l = 31.8$ mm and width $w = 15.8$ mm, giving a footprint area of $A = 502$ mm^2. The total mass of the sample was 9.28 ± 0.01 g. The wall thickness is 1.2 mm. This ABS LEGO sample is labelled **'AL'**.

3D printing is an ideal technique to create sophisticated stuctures with a high level of detail, so we also tested 3D printed structures for use as insulators. The printed samples discussed here were created using a 'Prusa i3 mk3s' model printer equipped with a nozzle which prints filaments of 0.45 mm in diameter. Two printer filaments were used for printing samples: a clear ABS plastic with tensile strength $P_{TS} = 39.2 \pm 0.5$ MPa and an opaque white polylactide (PLA) plastic with tensile strength $P_{TS} = 120 \pm 20$ MPa. A periodic minimal surface gyroid pattern [85, 86] was chosen as the core geometry for the printed samples, due to its strength capabilities with a limited volume of material [87]. Gyroids can be challenging and expensive to manufacture due to the complexities of their geometry, but 3D printing bypasses these difficulties.

The second sample was printed with the ABS filament, and has a total height of $h = 40.2$ mm, length $l = 31.8$ mm and width $w = 15.8$ mm (footprint area $A = 502$ mm^2), to match the AL sample. The faces have walls which are 0.9 mm thick, consisting of 2 print layers, and the gyroid interior was printed with a nominal volume fill factor of 5%. The finished ABS walled-gyroid sample has a mass of $m = 4.80 \pm 0.01$ g, and is labelled **'AWG'**.

The third sample was also printed with the ABS filament, and has the same total height of $h = 40.2$ mm and footprint area $A = 502$ mm^2, to match the standard. The sample was designed with no walls, so consists entirely of an open gyroid structure. A 5% volume fill factor is too low for a stable structure with these dimensions, so this was increased to 8%. The finished ABS opengyroid sample has a mass of $m = 1.69 \pm 0.01$ g, and is labelled **'AOG'**.

The fourth sample was printed with the PLA filament, and has the same total height of $h = 40.2$ mm and footprint area $A = 502$ mm^2, to match the standard. The faces have walls which are 0.9 mm thick, consisting of 2 print

layers, and the gyroid interior was printed with a volume fill factor of 5%. The finished PLA walled-gyroid sample has a mass of $m = 5.343$ g, and is labelled **'PWG'**.

Samples AWG and PWG have identical geometry to facilitate direct comparison between thermal conductivity of ABS and PLA. Samples AWG and AOG are printed from identical plastic to facilitate direct comparison between thermal conductivity of the open and walled gyroid designs.

5.2   Thermal Conductivity Measurement Details

The insulator samples were mounted in succession within a Lancaster-built ^{3}He/^{4}He dilution refrigerator to obtain their thermal conductivity. Details on the refrigerator are in Section 2.3. Each sample was sandwiched between two copper plates at either end of the sample's height, as shown in Figure 5.2. The 'lower' copper plate connects to the dilution refrigerator mixing chamber via a silver wire. This thermally anchors one end of the sample to the coldest body within the refrigerator. The 'upper' copper plate is thermally isolated via the sample. Vacuum grease was applied to both copper plates to create a firm thermal contact with the sample [88]. On the upper copper plate, a calibrated RuO$_2$ resistance thermometer was mounted to monitor the temperature of the insulated body. This was used for measuring the upper plate temperature T_{high} using a 4-point measurement with a Lake Shore 370 AC Resistance Bridge. The resistance was calibrated with temperature readout from a Lake Shore Ge thermometer, with both devices previously mounted on the mixing chamber plate in another dilution refrigerator, as shown in Figure 5.3. To calibrate the thermometer, a least squares fit was performed on the resistance data, with the equation $R_{\text{t}} = A/T_{\text{t}} + C$, where A and C are fit parameters. To take a temperature reading of the upper plate, the Lake Shore resistance bridge measures R_{t}, which is then converted to T_{high} via the calibration equation. A heater was also mounted on the upper plate. This consisted of a 3.1 Ω resistor, controlled and measured using another 4 point measurement setup. Bare NbTi wires, 40 cm long and 62 μm diameter, were used for electrical connections from the connector plate (thermalised with the
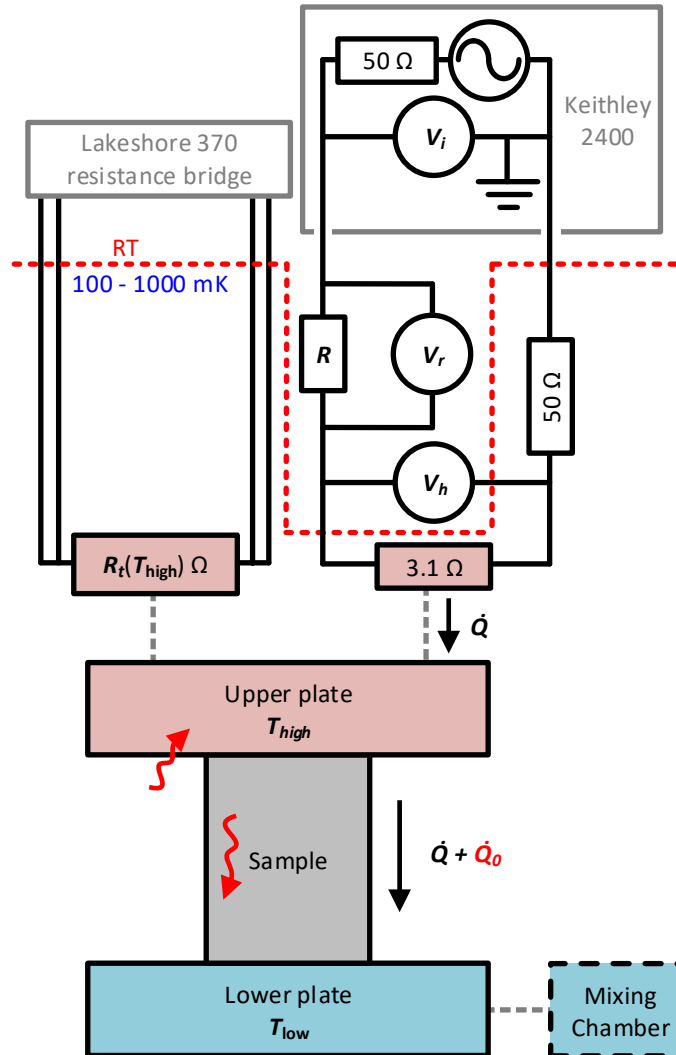
Figure 5.2: Schematic of experimental setup for low temperature thermal conductivity measurements. The sample is sandwiched between two copper plates, the 'upper' plate and the 'lower' plate (not to scale). The lower plate is connected thermally to the dilution refrigerator mixing chamber via a silver wire. This keeps the lower plate anchored at temperatures in the order of $T_{\text{low}} \sim$ mK. The upper plate is thermally connected to both the resistance thermometer with resistance R_{t} and a heater resistor which supplies heat $\dot{Q}$. Heat leaks to the upper plate and from the sample are modelled as an effective heat leak $\dot{Q}_0$, so the total heat flowing through the sample at thermal equilibrium is $\dot{Q} + \dot{Q}_0$. The resistance thermometer is controlled and measured with a Lake Shore 370 resistance bridge at room temperature. The heater is controlled by a Keithley 2400 function generator supplying an AC RMS voltage V_{i}. A SR830 lock-in amplifier was used to monitor the RMS voltage over the heater resistor, V_{h}. The RMS voltage V_{r} over a large series resistor R is monitored with another SR830 lock-in amplifier.
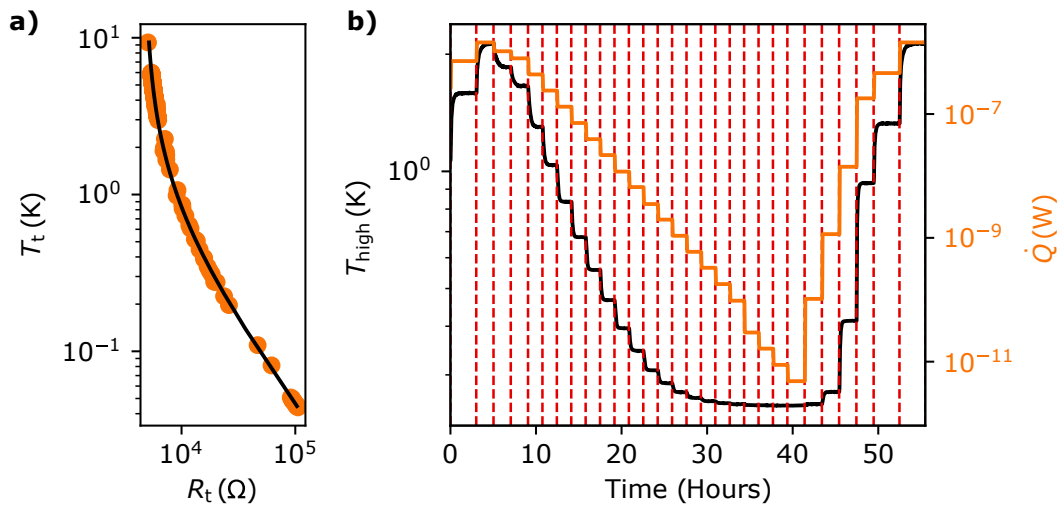
Figure 5.3: Thermal conductivity measurement with PWG sample. **a)** Resistance
thermometer calibration. The orange data points show the value of ther-
mometer resistance R_t recorded for a provided temperature T_t from a
Lake Shore Ge thermometer. This is fit with a simple model, shown with
the solid black line, which can be used to convert resistance R_t into a
temperature reading. **b)** an example of the thermal conductivity mea-
surement process, here showing data for the PWG sample. As the input
heat $\dot{Q}$ is adjusted, the upper plate temperature T_{high}, as read from the
calibrated resistance thermometer, settles at a new value. $\dot{Q}$ is stepped
when T_{high} has stabilised, roughly 90 minutes after the previous step.
Each data point for Figure 5.4 is read from 2 minutes before $\dot{Q}$ is stepped,
shown by the dashed red lines.

mixing chamber) down to the thermometer and heater mounted on the insulated upper plate. A Keithley 2400 supplied an AC input root mean square (RMS) voltage amplitude V_i at a frequency $f_i = 13\,\text{Hz}$. SR830 lock-in amplifiers were used to monitor the RMS voltage across heater and a line resistor R, V_h and V_R respectively. The heat $\dot{Q}$ being applied from the heater is then:

$$\dot{Q} = V_h I = \frac{V_h V_r}{R}. \tag{5.1}$$

The $3.1\,\Omega$ resistor is small and will vary slightly with temperature, so we used the line resistor $R = 9.9829\,\text{k}\Omega$ to limit the current and provide accurate current readouts below $V_r = 1\,\text{V}$. Above $1\,\text{V}$, the reading of V_r reached a maximum limit, so in this situation, V_r was supplied from a calibration of V_i with the available correct data, owing to the fact that $V_i \propto V_r$.

Each sample was cooled in the refrigerator and measured using the setup detailed in Figure 5.2. The temperature of the dilute phase in the mixing chamber of the dilution refrigerator, T_{low}, was measured using a vibrating wire resonator [89]. With the measurement wires in place, this value is usually $T_{low} \approx 2.3\,\text{mK}$, but for the AL sample run it was around $T_{low} \approx 4.0\,\text{mK}$. To obtain the thermal conductance, a range of input RMS voltage V_i was applied step-wise. This provides a unique input heat $\dot{Q}$, via Equation 5.1. Each time $\dot{Q}$ was stepped to a new value, there would be a time interval, typically 90 minutes long, to allow the insulated upper plate temperature to reasonably reach thermal equilibrium before taking an upper plate thermometer reading T_{high}, demonstrated in Figure 5.3. Data points of T_{high} against $\dot{Q}$ were extracted from the raw data by reading the values 2 minutes before $\dot{Q}$ was stepped. Each sample will produce a parasitic heat, which is a slow leakage of heat from the plastic material itself [90]. For each cooldown, the mixing chamber plate was held at base temperature for at least 9 days before the experiment was carried out, so the parasitic heat is small compared to $\dot{Q}$. The parasitic heat of the sample, combined with heat leaks to the upper plate, contributes to the total heat flow through the insulator $\dot{Q}_\Sigma$, and was modelled by including an effective heat leak constant $\dot{Q}_0$ so that $\dot{Q}_\Sigma = \dot{Q} + \dot{Q}_0$. For the thermal conductance of insulating materials at temperatures well below the Debye temperature, we can usually use the power law expression

Sample	$\lambda\,[\mathrm{Wm^{-1}K^{-(n+1)}}]$	n	$\dot{Q}_0\,[\mathrm{W}]$
AL	$(8.7 \pm 0.3) \times 10^{-5}$	1.75 ± 0.02	3.4×10^{-11}
AWG	$(3.07 \pm 0.05) \times 10^{-5}$	1.72 ± 0.02	1.7×10^{-9}
AOG	$(7.33 \pm 0.13) \times 10^{-5}$	1.68 ± 0.02	8.4×10^{-10}
PWG	$(4.45 \pm 0.05) \times 10^{-5}$	1.64 ± 0.02	5.47×10^{-9}

Table 5.1: Fitted values for Equation (5.2) of the insulator samples, as can be seen in FIG 5.4. 'W' and 'O' represent walled and open samples respectively.

from Equation 2.83. The thermal conductivity scaling constant λ and exponent of the insulator temperature n are related in the expression

$$\lambda = \frac{\dot{Q}_\Sigma(n+1)h}{A(T_{\mathrm{high}}^{n+1} - T_{\mathrm{low}}^{n+1})},$$

(5.2)

where T_{high} and T_{low} are respectively the temperatures of the upper and lower copper plates sandwiching the insulator. A derivation of this expression from the Debye model is shown in Section 2.5. Since in all our measurements T_{high} is much greater than T_{low}, and for plastics $n \sim 2$, we can safely neglect T_{low} from Equation 5.2. This then gives us the upper plate temperature T_{high} as a function of applied heat $\dot{Q}$, which is

$$T_{\mathrm{high}}(\dot{Q}) = \left(\frac{(n+1)h(\dot{Q}+\dot{Q}_0)}{A\lambda}\right)^{-(n+1)}.$$

(5.3)

This can be fit to the experimental data to extract λ and n, and therefore tell us the thermal conductivity κ, as a function of temperature T.

5.3 Insulator Results and Comparison

The results for applied heat $\dot{Q}$ versus upper plate temperature T_{high} are presented in Figure 5.4, which also includes the least squares fit of Equation 5.3 to the experimental data. The measurements from all four insulator samples tested demonstrate clear power law dependence for thermal conductivity. The model fit of Equation 5.3 yielded the values for scaling constant λ, temperature exponent n and effective heat leak $\dot{Q}_0$, for the temperature range measured. All of the power law parameters for all of the samples are shown
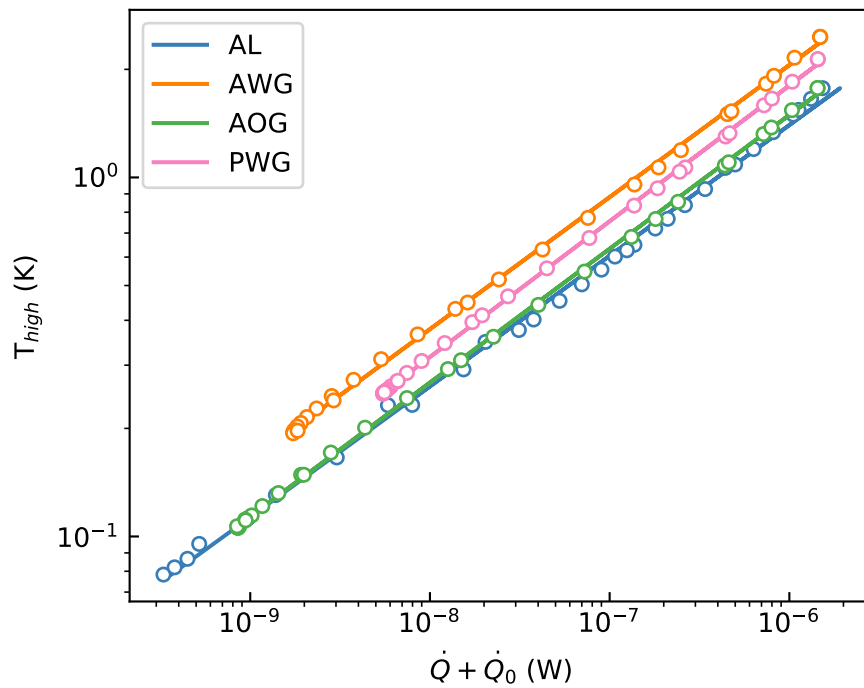
Figure 5.4: The relationship between settled upper plate temperature T_{high} and total heat applied $\dot{Q} + \dot{Q}_0$ for all three 3D printed samples (AWG, AOG and PWG), and the LEGO sample (AL). The dots show the experimental data points and the line represents the least-squared fit of Equation (5.2), which gives the values shown in Table 5.1.

in Table 5.1. These fitted values define the thermal conductivity κ power law via Equation (2.83). All of the ABS material samples, i.e samples AL, AWG and AOG, have a temperature exponent of around $n \approx 1.70$. For the PLA material sample, PWG, $n \approx 1.65$. This change in the temperature exponent is expected with a change in material. s m

The solid-void insulator samples were compared with previously measured bulk materials (from Table 2.1) in Figure 5.5. It can be seen that the new solid-void insulators offer an order of magnitude lower thermal conductance than the best bulk thermal insulators, such as Macor and Vespel-SP22 [64]. Thermal conductances in plastic materials at very low temperatures in general show T^n dependencies with n ranging between 1.7 and 2.4 [30], and all the samples we tested fall close to this range. The 3D printed structures are all more insulating than sample AL, which is likely due to the multi-layered nature of printed materials impeding heat flow. It has been shown that bulk 3D printed ABS has a thermal conductivity of $\kappa \approx 3.8\,\mathrm{WK^{-1}m^{-1}}$ at 4.2 K, with a $n = 0.5$ temperature dependence [91]. The thermal conductivity for the ABS samples (in fact, all our samples) begins to plateau with respect to temperature above 1 K, which suggest the ABS power law is changing at higher temperature to agree with the $T > 4.2\,\mathrm{K}$ experiment. The reduced value of λ we measure arises from the solid-void internal geometry of our ABS samples, and the natural next step in this analysis is to measure the thermal conductivity of bulk ABS and bulk 3D printed ABS below 1 K.

The new insulators all have a solid-void internal structure, which could be a concern for reliable mechanical strength. A single "No 3001" LEGO element was tested in a hydraulic press, with an increasing load applied until the material failed. It was found to withstand $\approx 290\,\mathrm{kg}$, demonstrating that it is mechanically robust despite the void space and will sustain any reasonable cryogenic experiment. The power input $\dot{Q}_\Sigma$ required to heat the top plate to $T_{\mathrm{high}} = 1\,\mathrm{K}$ when insulated with sample AL is $\dot{Q}_\Sigma = 0.4\,\mu\mathrm{W}$. To achieve the same level of insulation with commercial Vespel-SP22 (at the standard height of $h = 40.2\,\mathrm{mm}$), the cross sectional area of the insulator would need to be $A = 28.2\mathrm{mm}^2$. This is equivalent to a wall thickness of 0.3mm, assuming the standard sample length and width dimensions. In reality this would be a fragile design, and unlikely to withstand $\sim 290\,\mathrm{kg}$ of load. The power
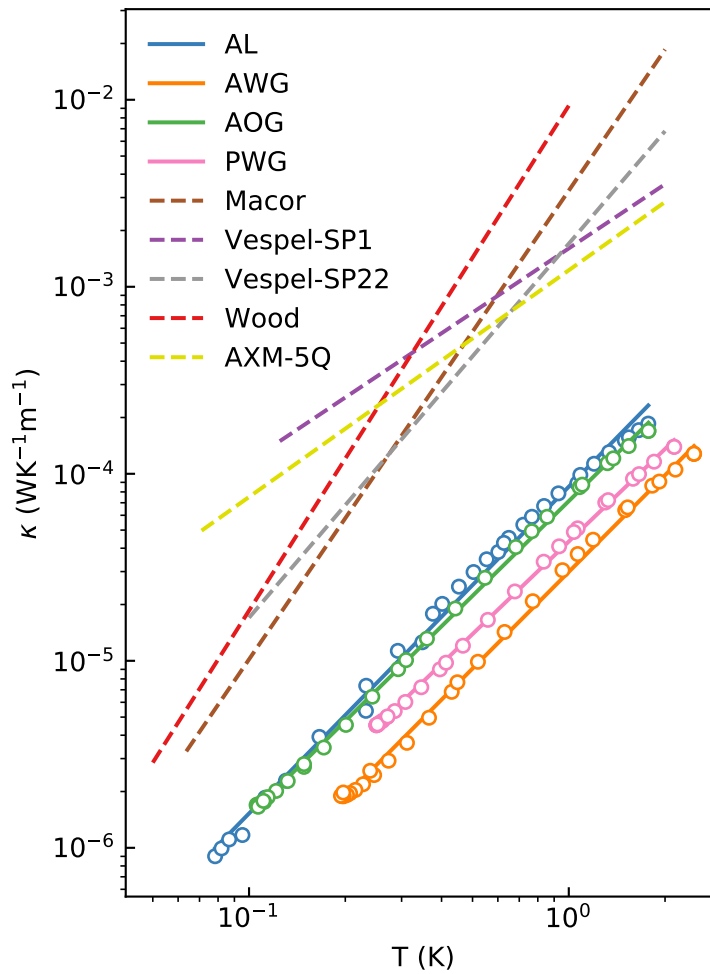
Figure 5.5: Comparison of the effective thermal conductivities κ of the insulator samples and other commonly used materials (and wood) at $T < 1\,\mathrm{K}$. The properties and citations for the other materials are shown in Table 2.1. The lines follow the thermal conductivity power law described by Equation 2.83

input $\dot{Q}_\Sigma$ required to make $T_{\text{high}} = 1\,\text{K}$ for sample AWG, AOG and PWG is $\dot{Q}_\Sigma = 0.14\,\mu\text{W}$, $0.34\,\mu\text{W}$ and $0.21\,\mu\text{W}$, respectively. This means for equivalent insulation, a Vespel-SP22 sample would need cross-sectional areas of $9.07\,\text{mm}^2$, $21.6\,\text{mm}^2$ and $13.2\,\text{mm}^2$, which would require a wall thickness of 0.10mm, 0.23mm and 0.14mm, respectively. Considering the printed samples have a wall thickness of 0.90mm and gyroid line thickness of 0.45mm, using Vespel-SP22 reduces the contact area and weakens the structure for the same insulation power.

5.4   Discussion

In this work, we have demonstrated that both commercially fabricated and 3D-printed plastic solid-void structures offer excellent thermal and structural properties at sub-Kelvin temperatures.

A structure fabricated from commercially available LEGO elements is shown to be surprisingly effective at insulating two bodies at sub-Kelvin temperatures, and is more effective than solid Macor or Vespel with the same volume footprint. The high level of insulation from this sample arises from the solid-void internal geometry combined with the contact resistance between the individual LEGO elements. The LEGO system contains a huge number of different compatible elements, so is an excellent basis for a versatile and customisable insulator solution. LEGO elements are moulded with a precision of $\sigma_x \approx 5\,\mu\text{m}$ [84], so reproducing structures accurately is very easy.

ABS and PLA gyroid structures produced by a 3D printer are shown to be even more effective as low-temperature insulators than the LEGO stack. The mechanical properties of 3D-printed plastic structures can be custom engineered and fine-tuned to match the required specifications beyond that which traditional machining can achieve. At the time of writing, the market price of a single sheet of Vespel of order $100\,\text{cm}^2$ would cover the cost of the whole 3D printer setup needed for creating the structures, which could be used repeatedly.

These features make solid-void insulators ideal for a range of applications.

For example a 3D-printed plastic structure could provide a way of supporting a classical processing unit at an elevated temperature very close to the sub-mK temperature of nearby quantum devices. An on-site classical processor can be used to control superconducting qubits, which is an essential step in the development of a scalable quantum computer [92, 93]. Industrial use of cryogenic technology will directly benefit from affordable cryogenic materials, for example performing passive terahertz imaging based on superconducting instruments [94]. The new insulators also have applications for space technology, especially 3D printed materials which can be manufactured in-orbit [95], to be used as versatile materials with well-established cryogenic properties [96]. The building of cryogenic refrigerators, specifically plastic mixing chambers and sample containers [29], could be improved with solid-void walls, reducing the parasitic heat leak from the walls while maintaining mechanical reliability.

The next stage in this project is to measure the thermal conductivity of both a bulk ABS sample and a 3D printed bulk ABS sample, below 1 K, for comparison with our results. This will give insight into which factors are contributing the most to the insulation properties of our samples. The bulk ABS sample will tell us to what degree the structure of samples AL, AWG and AOG have improved the insulation. The 3D printed bulk sample will tell us the impact on insulation for printed materials over the raw material. A similar set of measurements could also be made for the PLA material. All the samples discussed here need to undergo precise compressive and tensile testing to further determine the practicality of the samples' strength and compare with future design choices. The goal is to choose a sample geometry that minimises both the thermal conductivity and the impact on the samples' strength, as compared with bulk. Looking to the future, it would be useful to chart the cryogenic applications of other available 3D-printable materials, such as composite carbon fibre structures for high thermal conductivity and outstanding mechanical properties [97, 98].

Chapter 6

Conclusions

This thesis presents new techniques for both the measurement of electron temperature and the isolation of low temperature environments.

In this work, an electron thermometer built from a field-effect transistor was calibrated and operated with a single capacitive gate in two separate cryostats with different base temperatures. The experiments introduce and demonstrate a new level of simplicity and versatility for measuring electron temperature in a low temperature environment. The calibration of the thermometer generates a physical model of the quantum dot-reservoir system that exists within the field-effect transistor. In both cryostats this procedure correctly estimated physical parameters that characterise the quantum dot which would usually require source-drain connections to obtain. Electron thermometry was successfully performed with the calibrated thermometer in a $1.0\,\mathrm{K}$ to $3.0\,\mathrm{K}$ range. Below a fridge temperature of $1\,\mathrm{K}$, the electron temperature readout confidence boundary increases dramatically and extends towards $0\,\mathrm{K}$, due to strong tunnel coupling in the quantum dot. This defines the coldest limit of the electron thermometry for this specific thermometer and, more generally, demonstrates how this limit is observed. The electron thermometer was shown to have a sensitivity of $4.0 \pm 0.3\,\mathrm{mK}/\sqrt{\mathrm{Hz}}$ and $11 \pm 1\,\mathrm{mK}/\sqrt{\mathrm{Hz}}$, at $1.3\,\mathrm{K}$ and $3.0\,\mathrm{K}$ respectively.

The ability to calibrate and operate a non-galvanic electron thermometer with a single radio-frequency device connection simplifies the application of the device substantially. This new technique provides a versatile, sensitive and effective tool for monitoring electron temperature in nanoelectronic devices at cryogenic temperatures.

Looking to the future, a redesigned field-effect transistor geometry could allow a quantum dot to form with a weaker tunnel coupling to the reservoir. This would reduce the influence of tunnel broadening and allow more accurate electron temperature readout at lower temperatures, and a colder readout lower limit.

Also in this work, several plastic solid-void structures were demonstrated to offer excellent thermal isolation at sub-Kelvin temperatures. Thermally isolating refrigerator components and experiments can help reduce thermal noise and electron temperatures, for example within quantum circuits. They also provide a useful solution for containing elevated temperature experiments within a low temperature environment, which is useful in both research and industrial applications.

A structure fabricated from commercially available ABS LEGO elements was shown to be effective at thermally insulating two bodies at sub-Kelvin temperatures, and is more effective than commonly used solid insulators, such as Macor or Vespel, with the same volume footprint. The LEGO structure was found to follow a power law thermal conductivity of $\kappa = (8.7 \pm 0.3) \times 10^{-5} T^{1.75 \pm 0.02} \, \text{Wm}^{-1}\text{K}^{-1}$. The high level of insulation from this sample arises from the solid-void internal geometry combined with the contact resistance between the individual LEGO elements. 3D printed ABS and PLA gyroid structures were shown to be even more effective as low-temperature insulators than the LEGO structure. The ABS gyroid was found to have a thermal conductivity of $\kappa = (3.07 \pm 0.05) \times 10^{-5} T^{1.75 \pm 0.02} \, \text{Wm}^{-1}\text{K}^{-1}$ and $\kappa = (7.33 \pm 0.13) \times 10^{-5} T^{1.68 \pm 0.02} \, \text{Wm}^{-1}\text{K}^{-1}$ with and without outer walls, respectively. The walled sample has a lower thermal conductivity as the added structural support from the walls allows a lower density internal gyroid pattern. The walled PLA sample was found to have a thermal conductivity of $\kappa = (4.45 \pm 0.05) \times 10^{-5} T^{1.64 \pm 0.02} \, \text{Wm}^{-1}\text{K}^{-1}$. The mechanical properties of 3D-printed plastic structures can be custom engineered and fine-tuned to match the required specifications beyond that which traditional machining can achieve.

The LEGO system contains a huge number of different compatible elements, so is an excellent basis for a versatile and customisable insulator solution.

LEGO elements are moulded with remarkable precision, so reproducing structures accurately is very easy. However 3D printed structures are even more customisable and effective as insulators. The building of cryogenic refrigerators, specifically plastic mixing chambers and sample containers, could be improved with solid-void walls, reducing unwanted heat leak from the walls while maintaining mechanical reliability. They could also be useful for space technology, where the insulators can be manufactured in-orbit.

Looking to the future, a comprehensive comparison of the thermal properties of 3D printed materials with their respective bulk solids is needed to determine which factors contribute the most to the insulation properties of the measured samples. All the samples discussed in this thesis also need to be subject to multiple strength tests to quantify their practicality as a support structure. Gyroid structures appear to be strong and effective insulators, but with 3D printing an infinite number of possible designs can be tested. Therefore another future goal is to choose a new sample geometry that further minimises the thermal conductivity whilst maintaining good compressive and tensile strength.
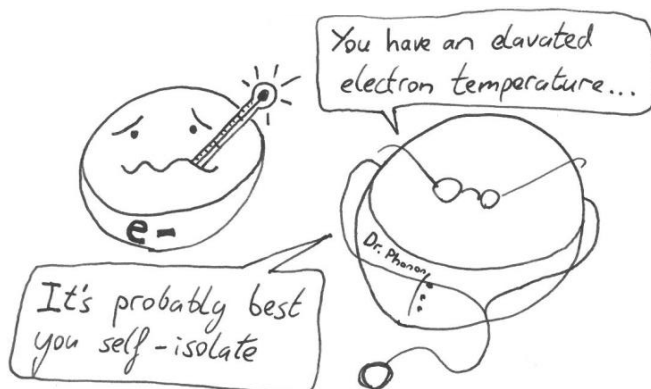
Bibliography

[1] J. G. Crowther. *British scientists of the nineteenth century*. Routledge & Paul, London, 1962.

[2] M. A. Nielsen and I. L. Chuang. *Quantum Computation and Quantum Information: 10th Anniversary Edition*. Cambridge University Press, USA, 10th edition, 2011.

[3] A. W. Harrow and A. Montanaro. Quantum computational supremacy. *Nature*, 549(7671):203–209, 2017.

[4] J. M. Gambetta, J. M. Chow, and M. Steffen. Building logical qubits in a superconducting quantum computing system. *Quantum Information*, 3(1):1–7, 2017.

[5] Y. A. Pashkin, O. Astafiev, T. Yamamoto, Y. Nakamura, and J. S. Tsai. Josephson charge qubits: a brief review. *Quantum Information Processing*, 8(2):55–80, 2009.

[6] T. Albash, V. Martin-Mayor, and I. Hen. Temperature scaling law for quantum annealing optimizers. *Physical review letters*, 119(11):110502, 2017.

[7] A. Dey and S. Yarlagadda. Temperature dependence of long coherence times of oxide charge qubits. *Scientific reports*, 8(1):1–9, 2018.

[8] P. A. M. Dirac. On the theory of quantum mechanics. *Proc. R. Soc. Lond.*, 112(762):661–677, 1926.

[9] F. Reif. *Fundamentals of statistical and thermal physics*. Waveland Press, 2009.

[10] D. S. Betts. Refrigeration and thermometry below one kelvin, 1976.

[11] C. Beenakker. Theory of coulomb-blockade oscillations in the conductance of a quantum dot. *Physical Review B*, 44(4):1646, 1991.

[12] F. Giazotto, T. T. Heikkilä, A. Luukanen, A. M. Savin, and J. P. Pekola. Opportunities for mesoscopics in thermometry and refrigeration: physics and applications. *Reviews of Modern Physics*, 78(1):217, 2006.

[13] A. Jones, C. Scheller, J. Prance, Y. Kalyoncu, D. Zumbühl, and R. Haley. Progress in cooling nanoelectronic devices to ultra-low temperatures. *Journal of Low Temperature Physics*, 2020.

[14] L. Spietz, K. W. Lehnert, I. Siddiqi, and R. J. Schoelkopf. Primary electronic thermometry using the shot noise of a tunnel junction. *Science*, 300(5627):1929–1932, 2003.

[15] Z. Iftikhar, A. Anthore, S. Jezouin, F. D. Parmentier, Y. Jin, A. Cavanna, A. Ouerghi, U. Gennser, and F. Pierre. Primary thermometry triad at 6 mk in mesoscopic circuits. *Nature communications*, 7(1):1–7, 2016.

[16] J. V. Koski, A. Kutvonen, I. M. Khaymovich, T. Ala-Nissila, and J. P. Pekola. On-chip maxwell's demon as an information-powered refrigerator. *Physical review letters*, 115(26):260602, 2015.

[17] J. Pekola, K. Hirvi, J. Kauppinen, and M. Paalanen. Thermometry by arrays of tunnel junctions. *Physical review letters*, 73(21):2903, 1994.

[18] D. I. Bradley, R. E. George, D. Gunnarsson, R. P. Haley, H. Heikkinen, Y. A. Pashkin, J Penttilä, J. R. Prance, M. Prunnila, L. Roschier, et al. Nanoelectronic primary thermometry below 4 mk. *Nature communications*, 7(1):1–7, 2016.

[19] O. Hahtela, E. Mykkänen, A. Kemppinen, M. Meschke, M. Prunnila, D. Gunnarsson, L. Roschier, J. Penttilä, and J. Pekola. Traceable coulomb blockade thermometry. *Metrologia*, 54(1):69, 2016.

[20] D. I. Bradley, A. M. Guénault, D. Gunnarsson, R. P. Haley, S. Holt, A. T. Jones, Y. A. Pashkin, J. Penttilä, J. R. Prance, M. Prunnila, et al.

On-chip magnetic cooling of a nanoelectronic device. *Scientific reports*, 7(1):1–9, 2017.

[21] J. Prance, C. Smith, J. Griffiths, S. Chorley, D Anderson, G. Jones, I Farrer, and D. Ritchie. Electronic refrigeration of a two-dimensional electron gas. *Phys. Rev. Lett.*, 102(14):146602, 2009.

[22] D. Maradan, L. Casparis, T. Liu, D. E. F. Biesinger, C. P. Scheller, D. M. Zumbühl, J. D. Zimmerman, and A. C. Gossard. GaAs quantum dot thermometry using direct transport and charge sensing. *J. Low Temp. Phys.*, 175(5-6):784–798, 2014.

[23] G. Nicolí, P. Märki, B. A. Bräm, M. P. Röösli, S. Hennel, A. Hofmann, C. Reichl, W. Wegscheider, T. Ihn, and K. Ensslin. Quantum dot thermometry at ultra-low temperature in a dilution refrigerator with a 4he immersion cell. *Review of Scientific Instruments*, 90(11):113901, 2019.

[24] L. DiCarlo, H. J. Lynch, A. C. Johnson, L. I. Childress, K. Crockett, C. M. Marcus, M. P. Hanson, and A. C. Gossard. Differential charge sensing and charge delocalization in a tunable double quantum dot. *Physical review letters*, 92(22):226801, 2004.

[25] A. Mavalankar, S. J. Chorley, J. Griffiths, G. A. C. Jones, I. Farrer, D. A. Ritchie, and C. G. Smith. A non-invasive electron thermometer based on charge sensing of a quantum dot. *Applied Physics Letters*, 103(13):133116, 2013.

[26] P. Torresani, M. J. Martínez-Pérez, S. Gasparinetti, J. Renard, G. Biasiol, L. Sorba, F. Giazotto, and S. De Franceschi. Nongalvanic primary thermometry of a two-dimensional electron gas. *Phys. Rev. B*, 88(24):245304, 2013.

[27] S. Gasparinetti, K. L. Viisanen, O.-P. Saira, T. Faivre, M. Arzeo, M. Meschke, and J. P. Pekola. Fast electron thermometry for ultrasensitive calorimetric detection. *Phys. Rev. Appl.*, 3(1):014007, 2015.

[28] I. Ahmed, A. Chatterjee, S. Barraud, J. J. L. Morton, J. A. Haigh, and
      M. F. Gonzalez-Zalba. Primary thermometry of a single reservoir
      using cyclic electron tunneling to a quantum dot. *Commun. Phys.*,
      1(1):1–7, 2018.

[29] D. Cousins, S. N. Fisher, A. Guénault, R. P. Haley, I. Miller,
      G. R. Pickett, G. Plenderleith, P Skyba, P. Thibault, and M. Ward. An
      advanced dilution refrigerator designed for the new lancaster
      microkelvin facility. *J. of Low Temp. Phys.*, 114(5-6):547, 1999.

[30] F. Pobell. *Matter and methods at low temperatures*, volume 2. Springer,
      2007.

[31] J. Chawner, A. Jones, M. Noble, G. Pickett, V. Tsepelin, and D. Zmeev.
      LEGO® block structures as a sub-kelvin thermal insulator. *Scientific
      Reports*, 9(1):1–4, 2019.

[32] L. P. Kouwenhoven, C. M. Marcus, P. L. McEuen, S. Tarucha,
      R. M. Westervelt, and N. S. Wingreen. Electron transport in quantum
      dots, *Mesoscopic electron transport*, pages 105–214. Springer, 1997.

[33] L. P. Kouwenhoven, D. Austing, and S. Tarucha. Few-electron
      quantum dots. *Reports on Progress in Physics*, 64(6):701, 2001.

[34] T. Ihn. *Semiconductor Nanostructures: Quantum States and Electronic
      Transport*. OUP Oxford, 2010. ISBN: 9780199534425.

[35] E. Schrödinger. An undulatory theory of the mechanics of atoms and
      molecules. *Physical Review*, 28(6):1049, 1926.

[36] D. T. Gillespie and P. A. Kazaks. *A quantum mechanics primer*,
      volume 41 of number 2. 1973, pages 302–303.

[37] H. Grabert and M. H. Devoret. *Single charge tunneling: Coulomb
      blockade phenomena in nanostructures*, volume 294. Springer Science &
      Business Media, 2013.

[38] L. Mandelstam and I. G. Tamm. The uncertainty relation between energy and time in non-relativistic quantum mechanics, *Selected Papers*, pages 115–123. Springer, 1991.

[39] P. A. M. Dirac. The quantum theory of the emission and absorption of radiation. *Proceedings of the Royal Society of London. Series A, Containing Papers of a Mathematical and Physical Character*, 114(767):243–265, 1927.

[40] E. Fermi. *Nuclear physics: a course given by Enrico Fermi at the University of Chicago*. University of Chicago Press, 1950.

[41] C. Whan and T. Orlando. Transport properties of a quantum dot with superconducting leads. *Physical Review B*, 54(8):R5255, 1996.

[42] J.-M. Zhang and Y. Liu. Fermi's golden rule: its derivation and breakdown by an ideal model. *European Journal of Physics*, 37(6):065406, 2016.

[43] G. Johansson, L. Tornberg, V. Shumeiko, and G. Wendin. Readout methods and devices for Josephson-junction-based solid-state qubits. *J. Phys. Condens. Matter*, 18(21):S901, 2006.

[44] S. N. Shevchenko, S. Ashhab, and F. Nori. Inverse landau-zener-stückelberg problem for qubit-resonator systems. *Phys. Rev. B*, 85(9):094502, 2012.

[45] S. Shevchenko, A. Omelyanchouk, and E Il'ichev. Multiphoton transitions in Josephson-junction qubits. *J. Low Temp. Phys.*, 38(4):283–300, 2012.

[46] R. Mizuta, R. Otxoa, A. Betz, and M. F. Gonzalez-Zalba. Quantum and tunneling capacitance in charge and spin qubits. *Physical Review B*, 95(4):045414, 2017.

[47] M. Esterli, R. M. Otxoa, and M. F. Gonzalez-Zalba. Small-signal equivalent circuit for double quantum dots at low-frequencies. *Applied Physics Letters*, 114(25):253505, 2019.

[48]   R. N. Bracewell and R. N. Bracewell. *The Fourier transform and its applications*, volume 31999. McGraw-Hill New York, 1986.

[49]   N. Hartman, C. Olsen, S. Lüscher, M. Samani, S. Fallahi, G. C. Gardner, M. Manfra, and J. Folk. Direct entropy measurement in a mesoscopic quantum system. *Nat. Phys.*, 14(11):1083–1086, 2018.

[50]   P. Echternach, M. Thoman, C. Gould, and H. Bozler. Electron-phonon scattering rates in disordered metallic films below 1 k. *Physical Review B*, 46(16):10339, 1992.

[51]   W. H. Press, S. A. Teukolsky, W. T. Vetterling, and B. P. Flannery. *Numerical recipes 3rd edition: The art of scientific computing*. Cambridge university press, 2007.

[52]   O. V. Lounasmaa. *Experimental principles and methods below 1K*. academic Press, 1974.

[53]   P. Das, R. B. de Ouboter, and K. W. Taconis. A realization of a london-clarke-mendoza type refrigerator, *Low Temperature Physics LT9*, pages 1253–1255. Springer, 1965.

[54]   Y. Nakamura, Y. A. Pashkin, and J. S. Tsai. Coherent control of macroscopic quantum states in a single-cooper-pair box. *nature*, 398(6730):786–788, 1999.

[55]   T. Duty, G. Johansson, K. Bladh, D. Gunnarsson, C. Wilson, and P. Delsing. Observation of quantum capacitance in the cooper-pair transistor. *Physical review letters*, 95(20):206807, 2005.

[56]   D. M. Pozar. *Microwave engineering*. John Wiley & Sons, 2009.

[57]   C. Bowick. *RF circuit design*. Elsevier, 2011.

[58]   S. J. Chorley, J. Wabnig, Z. V. Penfold-Fitch, K. D. Petersson, J. Frake, C. G. Smith, and M. Buitelaar. Measuring the complex admittance of a carbon nanotube double quantum dot. *Phys. Rev. Lett.*, 108(3):036802, 2012.

[59] A. C. Betz, R. Wacquez, M. Vinet, X. Jehl, A. L. Saraiva, M. Sanquer, A. J. Ferguson, and M. F. Gonzalez-Zalba. Dispersively detected Pauli spin-blockade in a silicon nanowire field-effect transistor. *Nano Lett.*, 15(7):4622–4627, 2015.

[60] M. F. Gonzalez-Zalba, S. N. Shevchenko, S. Barraud, J. R. Johansson, A. J. Ferguson, F. Nori, and A. C. Betz. Gate-sensing coherent charge oscillations in a silicon field-effect transistor. *Nano Lett.*, 16(3):1614–1619, 2016.

[61] I. Ahmed, J. A. Haigh, S. Schaal, S. Barraud, Y. Zhu, C.-m. Lee, M. Amado, J. W. A. Robinson, A. Rossi, J. J. L. Morton, et al. Radio-frequency capacitive gate-based sensing. *Physical Review Applied*, 10(1):014018, 2018.

[62] G. Ghione and C. Naldi. Parameters of coplanar waveguides with lower ground plane. *Electronics Letters*, 19(18):734–735, 1983.

[63] B. C. Wadell. *Transmission line design handbook*. Artech House, 1991.

[64] A. L. Woodcraft and A. Gray. A low temperature thermal conductivity database. *AIP Conf. Proc.*, 1185(1):681, 2009.

[65] P. Debye. Zur theorie der spezifischen wärmen. *Annalen der Physik*, 344(14):789–839, 1912.

[66] C. Enss and S. Hunklinger. *Low-Temperature Physics*. SpringerLink: Springer e-Books. Springer Berlin Heidelberg, 2005.

[67] D. Zych. Thermal conductivity of a machinable glass-ceramic below 1 k. *Cryogenics*, 29(7):758–759, 1989.

[68] M. Locatelli, D. Arnaud, and M. Routin. Thermal conductivity of some insulating materials below 1k. *Cryogenics*, 16(6):374, 1976.

[69] T. Wagner, S. Götz, and G. Eska. Thermal conductivity of wood at low temperatures. *Cryogenics*, 34(8):655–657, 1994.

[70] J. J. Morton, D. R. McCamey, M. A. Eriksson, and S. A. Lyon. Embracing the quantum limit in silicon computing. *Nature*, 479(7373):345–353, 2011.

[71] F. A. Zwanenburg, A. S. Dzurak, A. Morello, M. Y. Simmons, L. C. Hollenberg, G. Klimeck, S. Rogge, S. N. Coppersmith, and M. A. Eriksson. Silicon quantum electronics. *Reviews of modern physics*, 85(3):961, 2013.

[72] A. C. Betz, S. Barraud, Q. Wilmart, B. Placais, X. Jehl, M. Sanquer, and M. F. Gonzalez-Zalba. High-frequency characterization of thermionic charge transport in silicon-on-insulator nanowire transistors. *Appl. Phys. Lett.*, 104(4):043106, 2014.

[73] M. Veldhorst, C. Yang, J. Hwang, W Huang, J. Dehollain, J. Muhonen, S Simmons, A Laucht, F. Hudson, K. M. Itoh, et al. A two-qubit logic gate in silicon. *Nature*, 526(7573):410–414, 2015.

[74] A. Rossi, R. Zhao, A. S. Dzurak, and M. F. Gonzalez-Zalba. Dispersive readout of a silicon quantum dot with an accumulation-mode gate sensor. *Applied Physics Letters*, 110(21):212101, 2017.

[75] T. Watson, S. Philips, E. Kawakami, D. Ward, P. Scarlino, M. Veldhorst, D. Savage, M. Lagally, M. Friesen, S. Coppersmith, et al. A programmable two-qubit quantum processor in silicon. *Nature*, 555(7698):633–637, 2018.

[76] W. Huang, C. H. Yang, K. W. Chan, T. Tanttu, B. Hensen, R. C. C. Leon, M. A. Fogarty, J. C. C. Hwang, F. E. Hudson, K. M. Itoh, et al. Fidelity benchmarks for two-qubit gates in silicon. *Nature*, 569(7757):532–536, 2019.

[77] Y. He, S. Gorman, D. Keith, L. Kranz, J. Keizer, and M. Simmons. A two-qubit gate between phosphorus donor electrons in silicon. *Nature*, 571(7765):371–375, 2019.

[78] A. Chatterjee, S. N. Shevchenko, S. Barraud, R. M. Otxoa, F. Nori, J. J. Morton, and M. F. Gonzalez-Zalba. A silicon-based single-electron

interferometer coupled to a fermionic sea. *Physical Review B*, 97(4):045405, 2018.

[79] R. Corporation. RO4000 SeriesHigh Frequency Circuit Materials Data Sheet. Rogers Corporation, 2018. URL: www.rogerscorp.com.

[80] S. S. Mohan, M. del Mar Hershenson, S. P. Boyd, and T. H. Lee. Simple accurate expressions for planar spiral inductances. *IEEE Journal of solid-state circuits*, 34(10):1419–1424, 1999.

[81] B. Villis, A. Orlov, X Jehl, G. Snider, P Fay, and M Sanquer. Defect detection in nano-scale transistors based on radio-frequency reflectometry. *Applied Physics Letters*, 99(15):152106, 2011.

[82] P. Welch. The use of fast fourier transform for the estimation of power spectra: a method based on time averaging over short, modified periodograms. *IEEE Transactions on audio and electroacoustics*, 15(2):70–73, 1967.

[83] 3D render of LEGO blocks by Prof. G. R. Pickett. 2019.

[84] The LEGO Group. LEGO company profile. Corporate Brand Communications, 2020.

[85] A. H. Schoen. *Infinite periodic minimal surfaces without self-intersections*. National Aeronautics and Space Administration, 1970.

[86] R. Osserman. *A survey of minimal surfaces*. Courier Corporation, 2013.

[87] D. W. Abueidda, M. Elhebeary, C.-S. A. Shiang, S. Pang, R. K. A. Al-Rub, and I. M. Jasiuk. Mechanical properties of 3d printed polymeric gyroid cellular structures: experimental and finite element study. *Materials & Design*, 165:107597, 2019.

[88] L. J. Salerno, P. Kittel, and A. L. Spivak. Thermal conductance of pressed metallic contacts augmented with indium foil or apiezon grease at liquid helium temperatures. *Cryogenics*, 34(8):649–654, 1994.

[89] Y. M. Bunkov, A. Guénault, D. Hayward, D. Jackson, C. Kennedy, T. Nichols, I. Miller, G. Pickett, and M. Ward. A compact dilution refrigerator with vertical heat exchangers for operation to 2 mk. *Journal of Low Temperature Physics*, 83(5-6):257–272, 1991.

[90] M. Schwark, F. Pobell, M. Kubota, and R. M. Mueller. Tunneling with very long relaxation times in glasses, organic materials, and nb-ti-h (d). *Journal of low temperature physics*, 58(1-2):171–181, 1985.

[91] K.-P. Weiss, N. Bagrets, C. Lange, W. Goldacker, and J. Wohlgemuth. Thermal and mechanical properties of selected 3d printed thermoplastics in the cryogenic temperature regime. *IOP Conference Series: Materials Science and Engineering*, volume 102 of number 1, page 012022. IOP Publishing, 2015.

[92] J. Hornibrook, J. Colless, I. C. Lamb, S. Pauka, H Lu, A. Gossard, J. Watson, G. Gardner, S Fallahi, M. Manfra, et al. Cryogenic control architecture for large-scale quantum computing. *Physical Review Applied*, 3(2):024010, 2015.

[93] Y. Afsar, T. Moy, N. Brady, S. Wagner, J. C. Sturm, N. Verma, A. Agrawal, A. Natarajan, and C. An Interferer-Tolerant. 2018 index ieee journal of solid-state circuits vol. 53. *IEEE Journal of Solid-State Circuits*, 53(12):3701, 2018.

[94] A. Luukanen, L. Grönberg, M. Grönholm, P. Lappalainen, M. Leivo, A. Rautiainen, A. Tamminen, J. Ala-Laurinaho, C. R. Dietlein, and E. N. Grossman. Real-time passive terahertz imaging system for standoff concealed weapons imaging. *Passive Millimeter-Wave Imaging Technology XIII*, volume 7670, page 767004. International Society for Optics and Photonics, 2010.

[95] T. McGuire, M. Hirsch, M. Parsons, S. Leake, and J. Straub. Design for an in-space 3d printer. *Sensors and systems for space applications IX*, volume 9838, page 98380V. International Society for Optics and Photonics, 2016.

[96] C. Shemelya, A. De La Rosa, A. R. Torrado, K. Yu, J. Domanowski, P. J. Bonacuse, R. E. Martin, M. Juhasz, F. Hurwitz, R. B. Wicker, et al. Anisotropy of thermal conductivity in 3d printed polymer matrix composites for space based cube satellites. *Additive Manufacturing*, 16:186–196, 2017.

[97] Y. Nakagawa, K.-i. Mori, and T. Maeno. 3d printing of carbon fibre-reinforced plastic parts. *The International Journal of Advanced Manufacturing Technology*, 91(5-8):2811–2817, 2017.

[98] L. G. Blok, M. L. Longana, H Yu, and B. K. Woods. An investigation into 3d printing of fibre reinforced thermoplastic composites. *Additive Manufacturing*, 22:176–186, 2018.